pennsylvania
DEPARTMENT OF TRANSPORTATION

D-1 Flex Beam Field Instrumentation & Load Testing of Innovative Bridge Design

FINAL REPORT

March 31, 2023

By: Bryan Gonzalez, Ian Hodgson, Richard Sause, Clay Naito

ATLSS Center
Lehigh University

COMMONWEALTH OF PENNSYLVANIA
DEPARTMENT OF TRANSPORTATION

CONTRACT # EO4767
WORK ORDER # 05

Technical Report Documentation Page

1. Report No.	2. Government Accession No.	3. Recipient's Catalog No.
FHWA -PA-2023-005-EO4767 WO 05		

4. Title and Subtitle	5. Report Date
D-1 Flex Beam Field Instrumentation & Load Testing of Innovative Bridge Design	March 31, 2023
	6. Performing Organization Code

7. Author(s)	8. Performing Organization Report No.
Bryan Gonzalez, Ian Hodgson, Richard Sause, Clay Naito	

9. Performing Organization Name and Address	10. Work Unit No. (TRAIS)
ATLSS Center, Lehigh University 117 ATLSS Drive Bethlehem, PA 18015	**11. Contract or Grant No.** EO4767 WO 05

12. Sponsoring Agency Name and Address	13. Type of Report and Period Covered
The Pennsylvania Department of Transportation Bureau of Planning and Research Commonwealth Keystone Building 400 North Street, 6th Floor Harrisburg, PA 17120-0064	Final Report
	14. Sponsoring Agency Code

15. Supplementary Notes

16. Abstract

This report presents a study of an innovative superstructure system, termed Flex Beam, for short-span highway bridge applications. The system is comprised of inverted steel tee sections embedded in a concrete deck. An innovative mechanism for interface shear transfer between steel and concrete is provided by transverse deck reinforcement bars which pass through drilled holes near the tops of the steel tee webs. The first Flex Beam bridge was constructed in 2021, and consists of ten (inverted steel tee section) units with a span of 32 feet and width (from out-to-out) of 26 feet. This study assessed experimentally and numerically the in-situ performance of this Flex Beam demonstration bridge. After instrumenting the bridge, the response of the Flex Beam bridge to controlled-load testing and typical traffic loading was measured. In the report, the response of the Flex Beam bridge is assessed relative to the response anticipated from typical design and analysis calculations, and from the previous research on the Flex Beam system. Finite element analysis (FEA) results from several different FEA models are compared with the measured response of the bridge.

17. Key Words	18. Distribution Statement
Short-span steel highway bridge, composite steel bridge, controlled-load bridge testing, finite element analysis of highway bridges	No restrictions. This document is available from the National Technical Information Service, Springfield, VA 22161

19. Security Classif. (of this report)	20. Security Classif. (of this page)	21. No. of Pages	22. Price
Unclassified	Unclassified	100	**$114,885.36**

Form DOT F 1700.7 **(8-72)** **Reproduction of completed page authorized**

D-1 Flex Beam Field Instrumentation & Load Testing of Innovative Bridge Design

Final Report to the Pennsylvania Department of Transportation

March 31, 2023

By: Bryan Gonzalez, Ian Hodgson, Richard Sause, Clay Naito

ATLSS Center
Lehigh University

Contract: EO4767
Work Order: 05

Disclaimer

The contents of this report reflect the views of the authors who are responsible for the facts and the accuracy of the data presented herein. The contents do not necessarily reflect the official views or policies of the US Department of Transportation, Federal Highway Administration, or the Commonwealth of Pennsylvania at the time of publication. This report does not constitute a standard, specification or regulation.

Acknowledgements

The authors are grateful for support from the Pennsylvania Department of Transportation to conduct this study and prepare this report. The Flex Beam system concept initiated within Pennsylvania Department of Transportation, District 1. The authors are grateful for the contributions of Robin Hendricks, Lehigh University to the development of the Flex Beam system and to this study. The contributions of the technical staff of the ATLSS Center at Lehigh University are also acknowledged. The authors appreciate the comments on this study and report provided by colleagues at Modjeski and Masters, Inc., Harrisburg PA.

Table of Contents

List of Tables

Page

List of Figures

Page

List of Acronyms and Symbols

The symbols listed here are used in figures, tables, and the text of this report.

ATLSS	Advanced Technology for Large Structural Systems
PennDOT	Pennsylvania Department of Transportation
RHS	Right-Hand Side of Test Truck
LHS	Left-Hand Side of Test Truck
NTT	Nominal Test Truck
ATT	Actual Test Truck
B#	Inverted Steel Tee Section Designated Number
DK	Concrete Deck Label Used in Instrumentation
SG#	Strain Gauge (and Sensor Number) Used in Instrumentation
DISP	Displacement Sensor Used in Instrumentation
CL	Centerline of Bridge Span
QRT	Quarter Point of Bridge Span
E	East End of the Bridge (General and Used in Instrumentation)
W	West End of the Bridge (General and Used in Instrumentation)
EB	Eastbound direction of travel or eastbound lane
WB	Westbound direction of travel or westbound lane
Model 1	Numerical Model 1 (Shell)
Model 2	Numerical Model 2 (Shell)
Model 3	Numerical Model 3 (Shell)
Model 4	Numerical Model 4 (Solid – Uncalibrated Model)
Model 5	Numerical Model 5 (Solid – Calibrated Model)
$\mathbf{E_s}$	Theoretical Elastic Modulus for Steel Structural Members (29,000 ksi)
$\mathbf{E_c}$	Theoretical Elastic Modulus for Concrete (3,625 ksi)
$\boldsymbol{v_s}$	Poisson's Ratio for Steel (0.3)
$\boldsymbol{v_c}$	Poisson's Ratio for Concrete (0.2)
Hz	Hertz
in.	Inches
ft	Feet
lb.	Pounds
kip	Kilo Pounds (half-ton)
ksi	Kip Per-Square-Inch

Executive Summary

This report presents a study of an innovative highway bridge superstructure system termed Flex Beam, which was developed previously by Lehigh University in collaboration with the Pennsylvania Department of Transportation (PennDOT) and Modjeski and Masters, Inc. for short-span highway bridge applications. The system is comprised of inverted steel tee sections embedded in a concrete deck. An innovative mechanism for interface shear transfer between steel and concrete is provided by transverse deck reinforcement bars which pass through drilled holes near the tops of the steel tee webs. The first Flex Beam bridge was constructed in Erie County, within PennDOT District 1, in 2021. This Flex Beam demonstration bridge carries Pageville Road over the West Branch of the Cussewago Creek. The bridge, consisting of ten (inverted steel tee section) units, has a span of 32 feet and width (from out-to-out) of 26 feet.

This study assessed experimentally and numerically the in-situ performance of the Flex Beam demonstration bridge. After instrumenting the bridge (with strain gauges and displacement sensors), the response of the Flex Beam bridge to controlled-load testing and typical traffic loading was measured. The controlled-load testing used a heavy truck of known dimensions and weight. The response of the Flex Beam bridge was assessed relative to the response anticipated from typical design and analysis calculations, and from the previous research on the Flex Beam system. The ability of finite element analysis to capture the actual measured behavior of the bridge, under various levels of model refinement, was also assessed.

Controlled-load testing showed that the Flex Beam system exhibits fully composite behavior, consistent with a plane-section transformed section analysis, in regions away from the bearings. Fully composite behavior was observed in regions near the bearings (i.e., there was no significant relative longitudinal displacement (or slip between the steel tee section and the composite deck), however a linear strain distribution over the height of the composite section was not observed (i.e., the plane-section assumption was not valid), as a result of interaction with the large concrete end diaphragms. The end diaphragms introduced some flexural restraint of the composite steel tee sections near the bearings, which produced a negative bending effect near the bearings and reduced the largest steel tee flange bottom bending stresses near mid-span. The Flex Beam bridge has semi-integral abutments, and comparisons of controlled-load testing results with finite element analysis results suggest that pressure from the roadway subbase and backfill behind the concrete end diaphragms causes greater flexural restraint in the bridge than expected from a finite element analysis without this pressure. Relative displacements between the steel tee sections and concrete deck were relatively small (less than 0.001 in.) indicating fully composite behavior. Dynamic amplification of the bridge response was found to be small (possibly a result of the smooth roadway conditions on and near the bridge). The response of the bridge from the controlled–load testing was consistent with the response expected from typical design and analysis calculations and with the results from previous research on the Flex Beam system. In general, the measured stresses were low.

Monitoring of typical vehicular traffic over a period of six weeks showed that the structural response of the Flex Beam bridge was consistent with that observed from controlled-load testing. Strains and stresses were well below those measured during controlled-load testing with the largest observed values at approximately 65 percent of that attained from the test truck. The strains across the depth of the most heavily-loaded composite steel tee sections were shown to be consistent with the plane-section assumption typically used for analysis and design. Some of the data from events during the monitoring phase showed oscillations in mid-span flange bottom strain time-histories from vibration of the bridge, which was not observed during controlled-load testing, however, the stresses from these events were relatively small.

The finite element analysis results indicate that the parapets and end diaphragms have a significant effect on the response of the Flex Beam system. Including these two features in the finite element analysis model reduced flange bottom stresses (at the highest stress locations) of the steel tee sections. As expected, the model details influenced the finite element analysis results. Results from solid (or brick) element models, which enabled the parapets and end diaphragms to be modeled accurately, showed relatively good agreement with controlled-load testing results. Shell element models, which made it difficult to accurately

model the parapets and end diaphragms, provided larger (conservative) flange bottom stress results. The negative bending effect near the bearings (from restraint by the concrete end diaphragms) was captured by the solid element models. The solid element models also enabled the pressure from the roadway subbase and backfill behind the end diaphragms (from the semi-integral abutment condition) to be modeled.

A conventional line-girder analysis, assuming a fully composite condition and plane-section behavior and using a transformed-section model, provided results similar to those from finite element analysis of a single Flex Beam unit (i.e., single steel tee section with composite deck). However, the vehicular load distribution factors recommended for design of the Flex Beam system, were shown to be quite conservative compared to results from controlled-load testing and FEA. Stresses from a line-girder analysis with vehicular load distribution factors applied to the test truck load effects were significantly higher than those from 3D finite element analysis of the bridge and significantly higher than the measured test data. The analytical studies suggest that the vehicular load distribution factor for flexure used to design the Flex Beam demonstration bridge may be as much as 65% larger than the actual value for the Flex Beam demonstration bridge. Similarly, the vehicular load distribution factor for shear used to design the Flex Beam demonstration bridge may be as much as 2.8 times larger than the actual value for the Flex Beam demonstration bridge. A comprehensive study of vehicular load distribution factors for the Flex Beam system is needed.

CHAPTER 1: INTRODUCTION

1.1 Overview

This chapter provides an outline of the Flex Beam bridge project, including details of the Flex Beam demonstration bridge and the scope of the work performed to assess the design methodology for the bridge. The chapter ends with a description of the arrangement of this report.

1.2 Bridge Location

Constructed in 2021, the Flex Beam bridge carries Pageville Road across the West Branch of the Cussewago Creek within Elk Creek Township in Erie County in PennDOT District 1, near Edinboro, Pennsylvania. The creek flows in an approximately southerly direction, and Pageville Road runs in the east-west direction. The bridge location is shown in Figure 1.

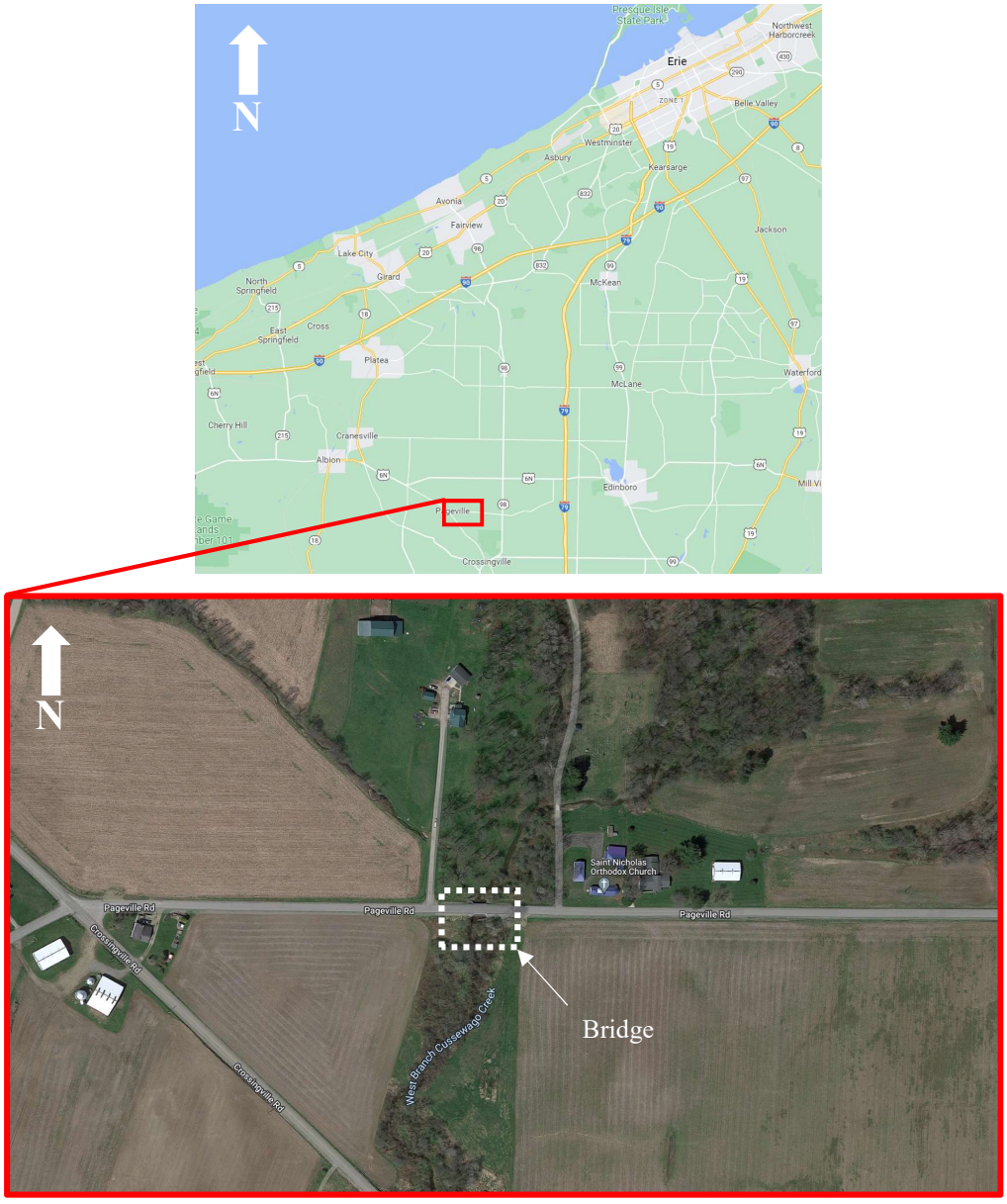

Figure 1. Location of Flex Beam demonstration bridge (http://maps.google.com, 2022).

1.3 Bridge Description

Currently in-service, the Flex Beam demonstration bridge is a single-span bridge based on previous research on the Flex Beam bridge system at Lehigh University (Naito, Hendricks, & Sause, 2018a) (Naito, Hendricks, & Sause, 2018b). The bridge has ten composite concrete deck and inverted steel tee sections as the primary flexural members. The bridge span, from bearing-to-bearing, is 32-ft and the total structure length, from end-to-end, is 34-ft. A plan view drawing of the bridge is shown in Figure 2.

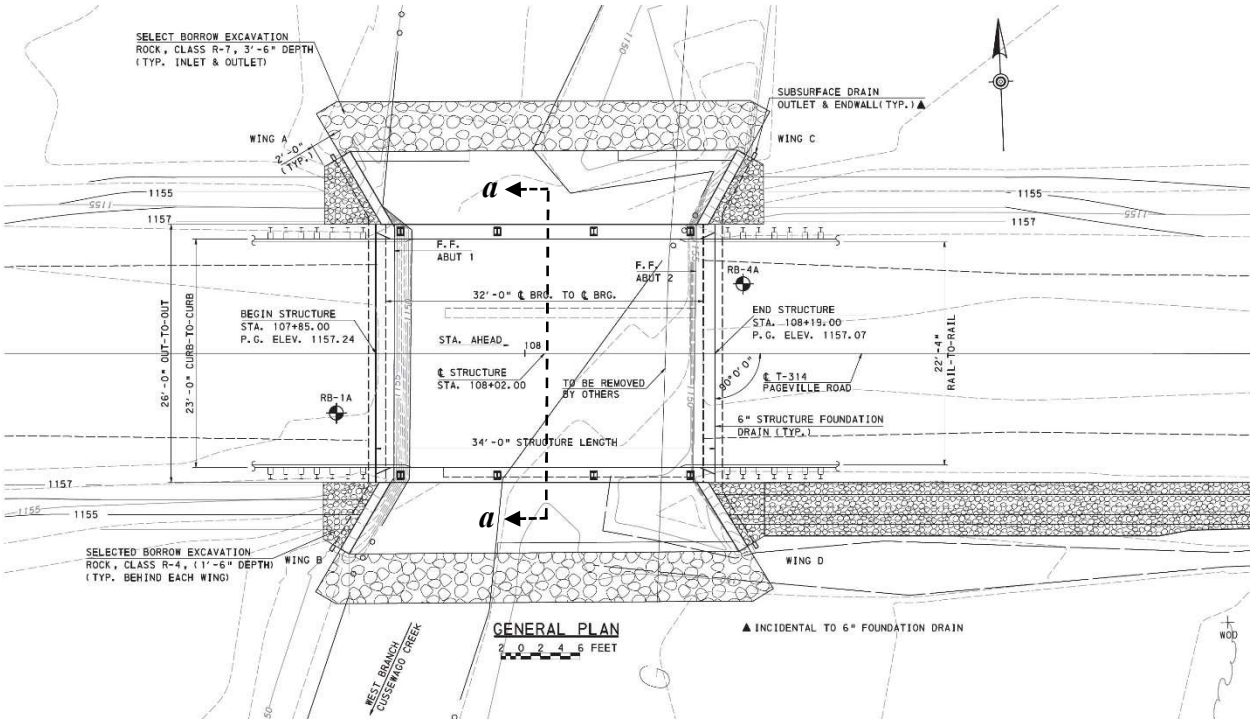

Figure 2. Plan view of Flex Beam bridge (PennDOT, 2020).

The ten composite concrete deck and inverted steel tee sections of the bridge were constructed from five prefabricated units, with each unit incorporating two inverted steel tee sections (see Figure 3 and Figure 4).

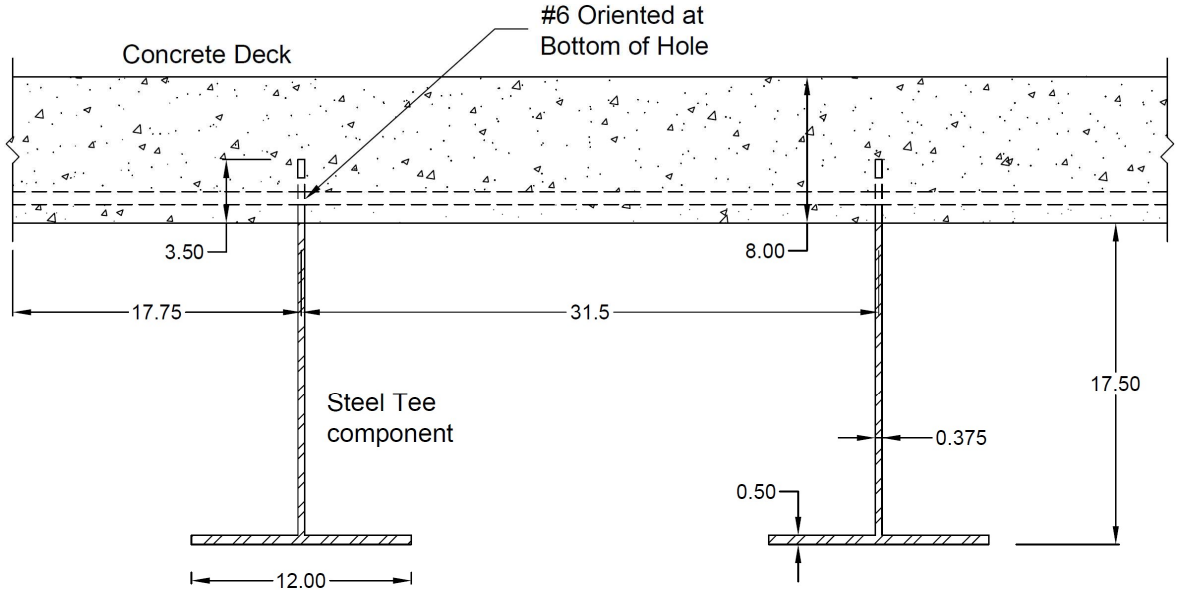

Figure 3. Cross section of prefabricated unit with two inverted steel tee sections (all dimension in inches) (PennDOT, 2020).

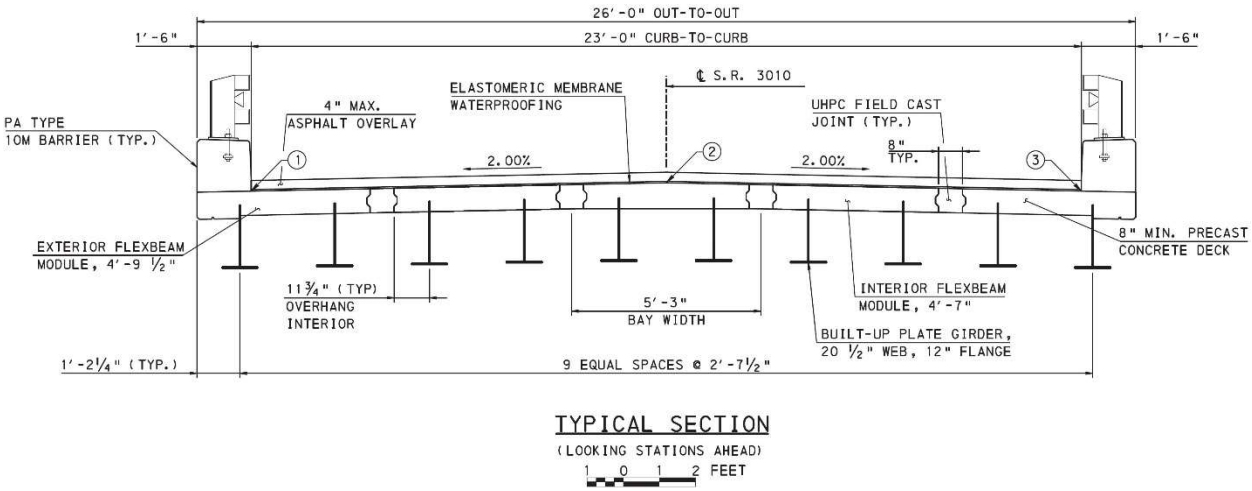

Figure 4. Section view of bridge (Section a-a shown in the plan view) (PennDOT, 2020).

The overall width of the bridge is 26-ft and the roadway width is 23-ft. The bridge has two traffic lanes flanked by concrete parapets with a width of 18-in. and height of 20-in. (see Figure 5).

Figure 5. Demonstration Flex Beam bridge. Left: West direction view of bridge, and Right: South direction view of bridge.

The web of each inverted steel tee section is embedded in the concrete deck (see Figure 3). A unique interface shear connection between each steel tee section and the concrete deck is provided by transverse steel reinforcement, acting as dowels, passing through holes in the steel tee webs. The bridge also has concrete end diaphragms that are 21-in. in width which are cast between inverted steel tee sections. Composite behavior between the steel tee section and concrete diaphragm is provided using the same transverse steel dowel interface shear connection (see Figure 6).

Figure 6. Photo of prefabricated unit showing the end diaphragm and parapet.

The Flex Beam demonstration bridge has large concrete end diaphragms, shown in Figure 6, and was constructed without back-walls at both abutments. This semi-integral abutment design simplifies the reconstruction and reuse of existing abutments in bridge replacement projects. Without independent back-walls, however, the roadway subbase and backfill are in direct contact with the end diaphragms and restrain the end diaphragms and attached steel tee sections. The effects of the semi-integral abutments are discussed further in Chapter 4.

The effects of the parapets, end diaphragms, and restraint from the semi-integral abutments are often neglected in typical design calculations. The effects on vehicular load distribution among the steel tee sections and the validity of assumptions/simplifications used to design the Flex Beam system were assessed by comparing results from controlled-load testing and monitoring of the typical vehicular-load response with results from simple calculations and finite element analysis of the bridge.

1.4 Project Scope

To evaluate response of the Flex Beam demonstration bridge under vehicular loads, and to assess the design assumptions/simplifications, the following scope of work has been performed:

1. Finite element analysis (FEA) of the Flex Beam bridge to determine areas of interest for the location of strain gauges and displacement sensors for controlled-load testing and monitoring of the typical vehicular-load response of the demonstration bridge. The FEA provided the expected maximum bending stress (and strain) and shears in the composite steel tee sections. The FEA work included development of various calculation models of the demonstration bridge, going from a simplified line-girder approach, useful for design of a Flex Beam bridge, to rigorous FEA models that incorporate the parapets, end diaphragms, and restraint from the semi-integral abutments that influence the response of the bridge.
2. The Flex Beam bridge was instrumented with strain gauges and displacement sensors. The instrumentation plan was based on the results of the FEA. 29 strain gauges and 7 displacement transducers were installed to measure strains, and relative displacements, respectively, at locations of interest on the steel tee sections and on the bottom of the concrete deck. Displacement transducers were positioned to measure the relative longitudinal displacement between the web of the inverted steel tee sections and concrete deck to assess the interface shear connection and the composite behavior of the Flex Beam system.
3. Controlled-load testing was performed on the Flex Beam bridge. The controlled-load testing used a truck of known weight and geometry that was moved to various positions on the bridge deck (statically and dynamically). The specific transverse and longitudinal positions of the test truck

were based on FEA results. The controlled-load testing provided calibration data for refinement of the FEA models, data on the overall flexural and shear response of the Flex Beam demonstration bridge, and data on the distribution of moment and shear among the individual composite steel tee sections. Controlled-load testing was performed immediately after installation of the instrumentation.

4. Following the controlled-load testing, the Flex Beam bridge was monitored for six weeks to assess the response of the bridge under typical vehicular load. Due to the lack of accessible electric power at the bridge, a solar power system was installed to provide power to a data logger system. From the instrumentation used in the controlled load testing, a subset of 12 strain gauges were selected for the typical vehicular-load response monitoring.
5. The results from the controlled-load load testing and typical vehicular-load response monitoring are documented in this report. The report provides validation of the current Flex Beam design assumptions/simplifications regarding composite behavior, and moment and shear distribution among the composite steel tee sections.

1.5 Organization of Report

Chapter 2 provides a description of the testing of the Flex Beam demonstration bridge, including controlled-load testing and monitoring of the typical vehicular-load response.

Chapter 3 summarizes the results from controlled-load testing and monitoring of the typical vehicular-load response of the bridge.

Chapter 4 describes the finite element analyses and other calculations performed in the project, including pre-test analyses and post-test analyses, which were conducted before and after the controlled-load testing, respectively.

Chapter 5 presents a summary of results and conclusions from the project.

CHAPTER 2: TESTING PROGRAM

2.1. Background

To measure the response of the Flex Beam demonstration bridge, an array of instrumentation consisting of strain and displacement sensors were installed. Data were collected from these sensors during controlled-load testing of the bridge. Additionally, data were collected from selected strain gauges over several weeks of monitoring of the typical vehicular-load response of the bridge.

The purpose of the controlled-load testing is to measure the response of the bridge and the instrumented structural components to a known vehicular load. Strains in the concrete deck and inverted steel tee sections, and relative longitudinal displacements between the concrete deck and steel tee sections were measured. The controlled-load testing provided calibration data for refinement of finite element analysis (FEA) models, data on the overall flexural and shear response of the Flex Beam bridge, and some data on the load distribution between the individual composite steel tee sections. A single test truck was used for the controlled-load testing. The test truck axle weights and geometry were used as input to FEA models. The strains measured during the controlled-load testing were compared with results from the FEA models and used to calibrate the FEA models. This chapter describes the controlled-load testing and monitoring of the typical vehicular-load response.

2.2. Test Truck

The controlled-load testing used a loaded standard PennDOT triaxle dump truck (see Figure 7). This test truck includes a fourth axle (tag axle) between the front and tandem axles, but to maximize the axle weights, the tag axle was not used during controlled load testing (i.e., the tag axle was in the raised position and did not support any load during the testing). The test truck was weighed on calibrated scales by a Pennsylvania State Police Weight Enforcement team. The test truck was driven to and from the bridge, and during the controlled-load testing, by PennDOT personnel.

Two test truck axle weights and geometries were considered in the project. In the initial phase of the project (*pre-test analyses*), the properties of a test truck from a previous bridge testing project (with axle weights and geometry that were anticipated for the test truck in the controlled-load testing) were used to model the test truck – here termed the *Nominal Test Truck* or NTT. For the second phase of the project (*post-test analyses*) the measured axle (and wheel) weights and geometry of the load test truck used in the controlled-load testing of the bridge were utilized – here termed the *Actual Test Truck* or ATT. The NTT is shown in the left image of Figure 7 while the ATT is shown in the right image.

Figure 7. Tri-Axle PennDOT dump trucks used in bridge controlled-load testing. Left: Truck for pre-test analyses or Nominal Test Truck (NTT), and Right: Truck for controlled-load testing and post-testing analyses or Actual Test Truck (ATT) (Note: tag axle was lifted during controlled-load testing and not included in analyses.)

Using the results of the pre-test analyses, specific locations for the instrumentation were selected from FEA results using the NTT. Various load scenarios (transverse positions and longitudinal positions) and associated finite element analysis results were considered to determine the instrumentation locations.

The ATT was weighed by a Pennsylvania State Police Weight Enforcement team prior to the controlled-load testing using calibrated scales to obtain the gross vehicle weight (GVW) as well as the individual wheel weights. Additionally, key dimensions of the truck (axles) were measured on-site by Lehigh University researchers prior to the controlled-load testing. Figure 8 shows the truck weights and dimensions of the NTT and ATT. The NTT used for pre-test analyses has a GVW of 72 kips, while the ATT used for controlled-load testing and post-test analyses had a GVW of 77.55 kips.

Nominal Test Truck (NTT) Axle Load Data

Front Axle Load (lb)	Tandem Axle					
	Axle 2 (lb)		Axle 3 (lb)			
20,000	26,000		26,000			
LHS (lb)	RHS (lb)	LHS (lb)	RHS (lb)	LHS (lb)	RHS (lb)	
10,000	10,000	13,000	13,000	13,000	13,000	

Actual Test Truck (ATT) Axle Load Data

Front Axle Load (lb)	Tandem Axle					
	Axle 2 (lb)		Axle 3 (lb)			
21,800	27,500		28,250			
LHS (lb)	RHS (lb)	LHS (lb)	RHS (lb)	LHS (lb)	RHS (lb)	
9,850	11,950	12,400	15,100	12,700	15,550	

Geometry of Nominal Test Truck (NTT)

A	B	C	D	E	F	G
(in)	(in)	(in)	(in)	(in)	(in)	(in)
210	264	84	74	9	20	10

Geometry of Actual Test Truck (ATT)

A	B	C	D	E	F	G
(in)	(in)	(in)	(in)	(in)	(in)	(in)
224	275.5	85	73	8	22	13.5

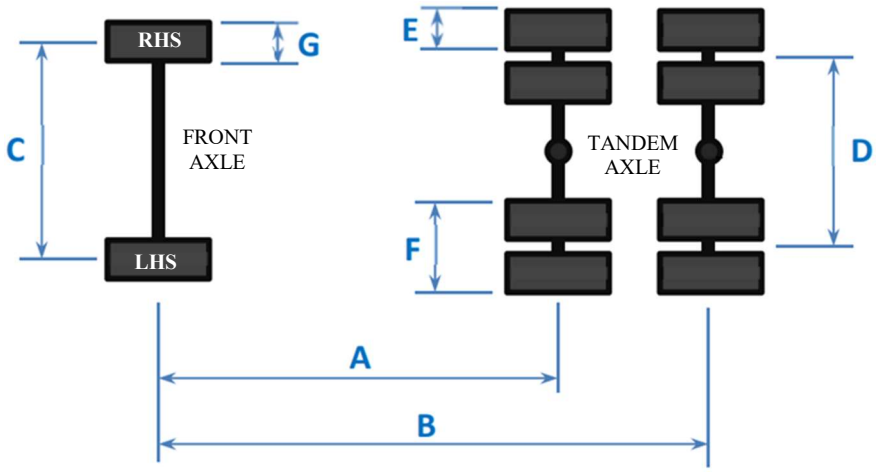

Figure 8. Test truck dimensions and weights.

The dimensions of the areas of wheel contact with the roadway in the longitudinal direction of the truck were not measured and a typical value of 10 in. is assumed. The wheel loads of the NTT were assumed to be symmetrical about the longitudinal axis (i.e., both sides of the truck are equally loaded), while the ATT has measured wheel loads that were unsymmetrical (i.e., with different wheel weights between the left-hand-side (LHS) and the right-hand-side (RHS) of the truck). The rear tandem axles of the ATT had different measured total weights, while the rear tandem axles of the NTT were assumed to have the same weights. The differences between the ATT and the NTT were included in the corresponding analyses.

2.3. Loading Configurations

The pre-test analysis FEA considered three transverse positions of the test truck (given in Table 1), namely: (**1**) mid-width of the bridge, (**2**) mid-lane, and (**3**) with the centroid of the wheels at 2 ft. from the parapet (i.e., roadway edge). For each transverse position, four longitudinal positions were considered, namely: (**1**) the truck centered on mid-span; (**2A**) a truck position with the front axle of the tandem axle centered on the bearing, the rear axle of the tandem on the bridge, and the front axle of the truck off the bridge; (**2B**) a truck position with the rear axle of the tandem axle centered on the bearing, the front axle of the tandem axle and

the front axle of the truck on the bridge; and (**3**) a truck position with the tandem axle centered at mid-span (and the front axle of the truck off the bridge). The test truck was placed at these same positions during the controlled-load testing.

Table 1. Load positions for FEA and controlled-load testing.

Transverse Position	Longitudinal Position
(**1**) Mid-Width	(**1**) Truck Centered in Span
(**2**) Mid-Lane	(**2A**) Front Axle of Tandem Centered on the Bearing (**2B**) Back Axle of Tandem Centered on the Bearing
(**3**) 2 ft. from Road Edge	(**3**) Tandem Axle Centered at Mid-Span

Figure 9 shows an example plan view of the load positions used for FEA and controlled load testing, where the NTT is in Transverse Position 1 and Longitudinal Position 3. The figure shows the plan dimensions of the NTT (i.e., wheel locations) and the distances to the ends of the bridge deck and the north parapet. Using the test truck dimensions in Figure 8 and the load positions in Table 1, similar plan views can be created for other load positions of the NTT or ATT. The test truck positions are further described in Chapter 4.

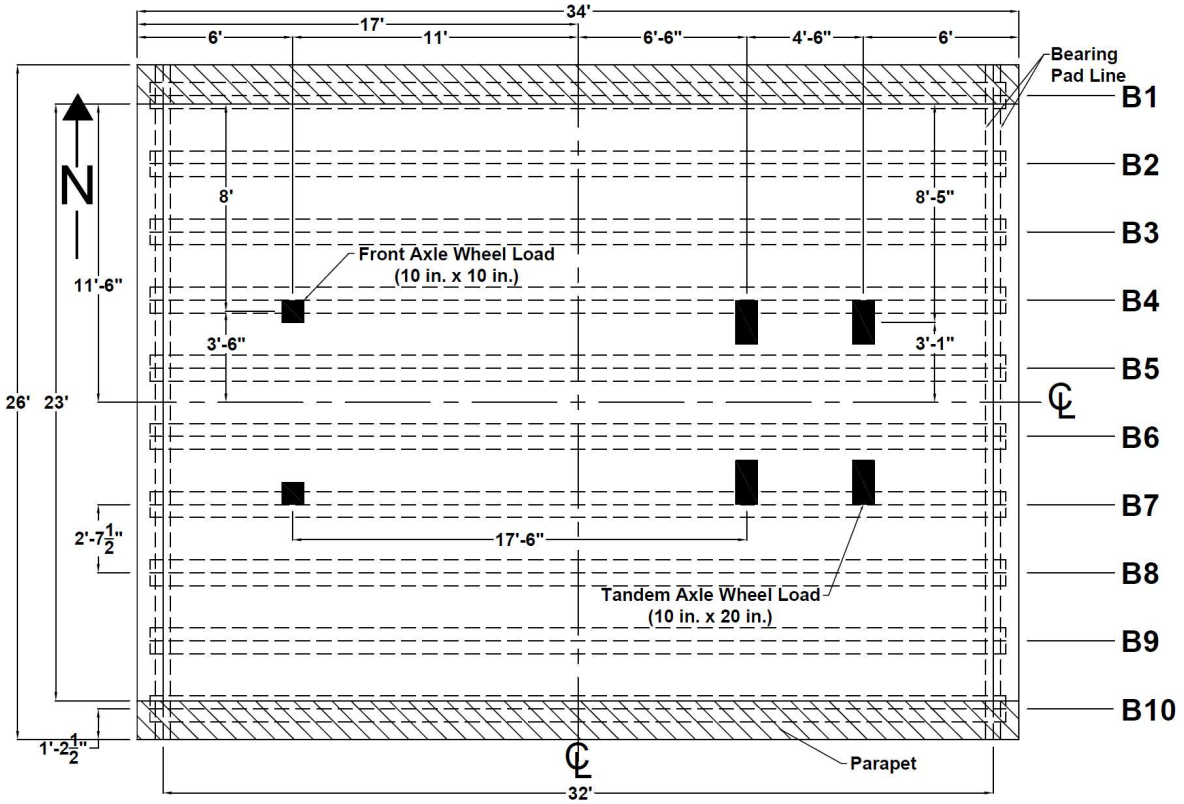

Figure 9. Plan view of NTT in Transverse Position 1 and Longitudinal Position 3.

2.4. Locations Selected for Sensors

Designations for the inverted steel tee sections are presented in Figure 10 along with sensor locations. More detail about the instrumented locations is given later. Considering the various test truck positions given above (transverse and longitudinal positions), the finite element results from pre-test analysis were used to plan the locations for load testing instrumentation.

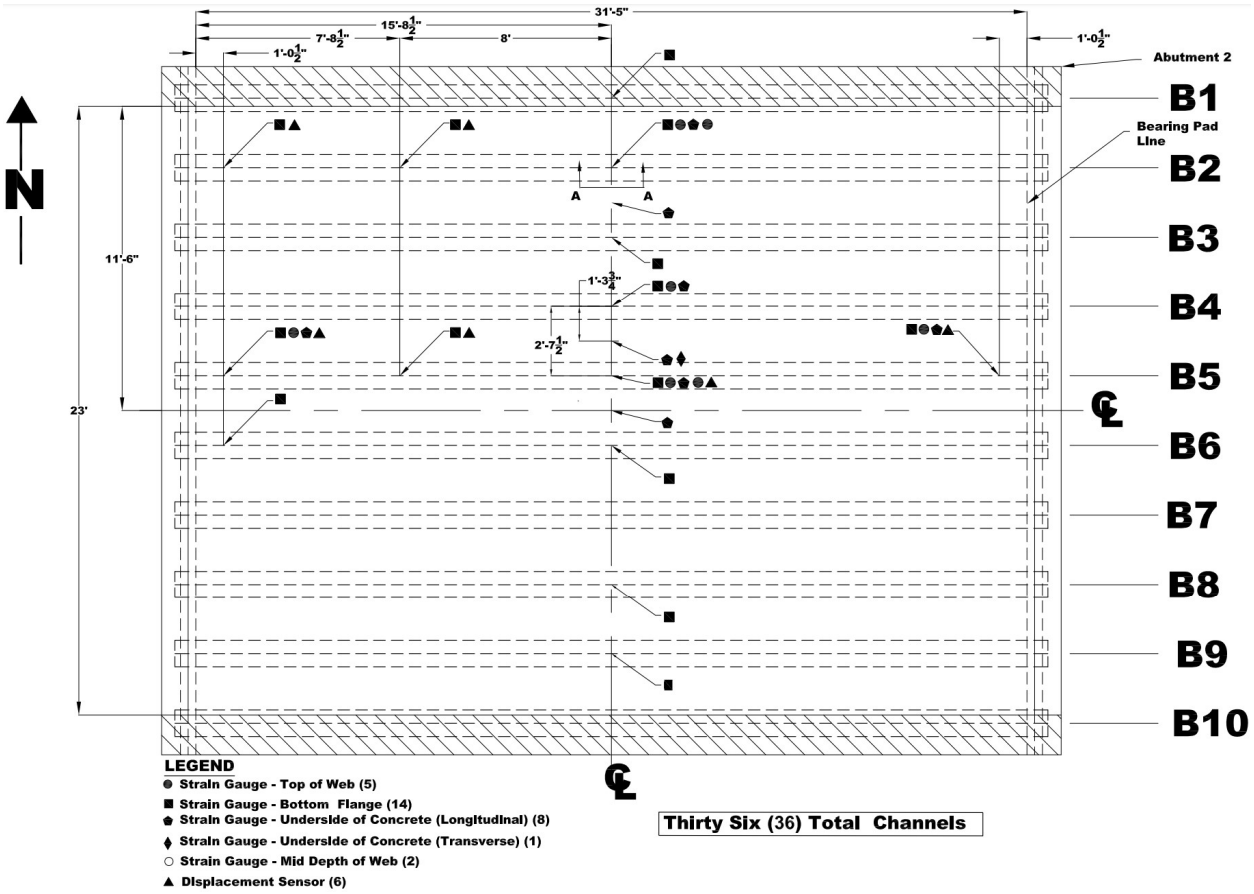

Figure 10. Labels for steel tee components and locations selected for instrumentation.

A complete description of the FEA (for both pre-test and post-test analyses) is provided in Chapter 4. For the purpose of describing the instrumentation planning process, the FEA model (denoted "Model 4") used in the instrumentation planning process was made of solid elements and was later found (see Chapter 4) to provide a reasonably accurate representation of the bridge response to the test truck loading.

The FEA results of interest include shear connection forces, mid-span deflections, and stresses in the longitudinal direction on the bottom of the flanges of the inverted steel tee sections and on the top and bottom of the concrete deck, as well as transverse stresses in the concrete deck. Figure 11 shows FEA results for stresses (in ksi) at the flange bottoms, with the test truck centered in the westbound lane and the tandem axle centered at mid-span (i.e., from Model 4 with the test truck in Transverse Position 2, Longitudinal Position 3). The stress contours show the largest longitudinal tensile stresses in blue and compressive longitudinal stresses (near the bearings) in grey. For this transverse position of the test truck, to measure the maximum stress on the bottom of the flange, the third inverted steel tee beam from the north (B3) was instrumented at mid-span.

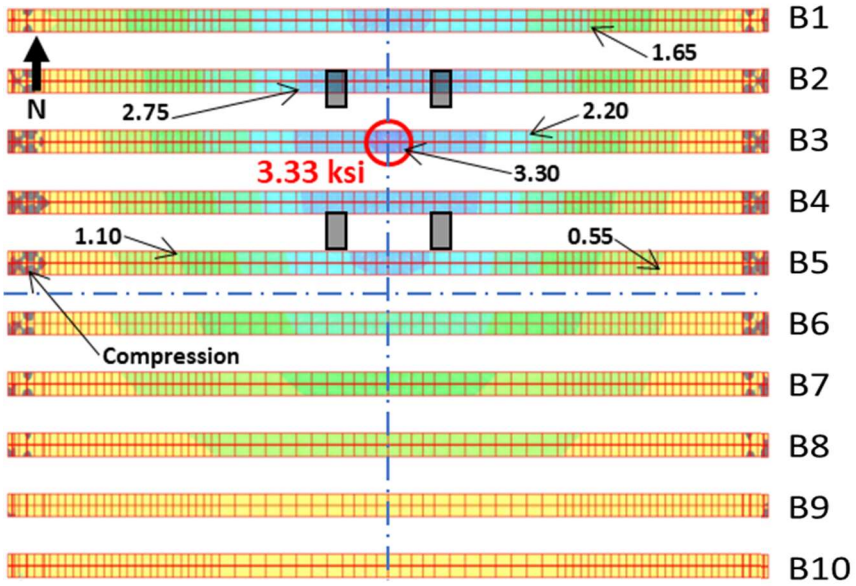

Figure 11. Longitudinal stress distribution on flange bottom (Model 4: Transverse Position 2, Longitudinal Position 3). Test truck wheel loads shown in black. Maximum value shown in red with position circled. Compressive stresses in grey.

Figure 12 shows a side view of the inverted steel tee section with the largest longitudinal flange stress (third steel tee section from the north, B3). The image shows a stress gradient (compression in grey) over the depth of the steel tee section from the FEA results with the test truck in Transverse Position 2, Longitudinal Position 3. In the instrumentation plan, strain gauges on the flange and web were placed at several elevations to measure this gradient. In addition to measuring the variation of stress through the steel tee section depth, these strain measurements were used to assess the corresponding curvature and bending moment to validate the plane-section assumption (i.e., beam theory) and transformed-section model used in design calculations.

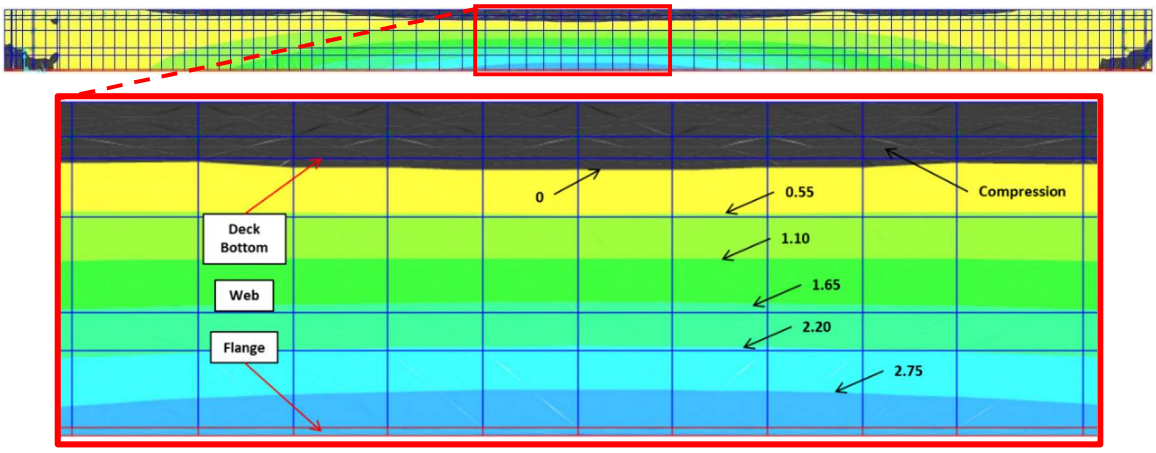

Figure 12. Longitudinal stress over depth of inverted steel tee section (Model 4: Transverse Position 2, Longitudinal Position 3). Top: full length tee section, and Bottom: enlarged view at mid-span of tee section.

Simultaneous measurement of adjacent web and deck strains was considered useful for assessing the composite action of the Flex Beam system, which is assumed for design calculations. To assess the composite action, surface-bonded strain gauges were applied to both the bottom surface of the concrete deck and the adjacent web of the steel tee section; with full composite action these strains should be similar. Relative displacements between the concrete deck and steel tee web were measured to further assess the composite action.

For certain load cases, the FEA results show that the torsional rigidity of the concrete end diaphragms leads to negative bending of the composite steel tee sections near the bearings. The FEA longitudinal stress results in Figure 13 for the flange bottom of the steel tee sections (from Model 4 with the test truck in Transverse Position 1, Longitudinal Position 3) show negative bending at each end of the steel tee sections near the centerline of the bridge.

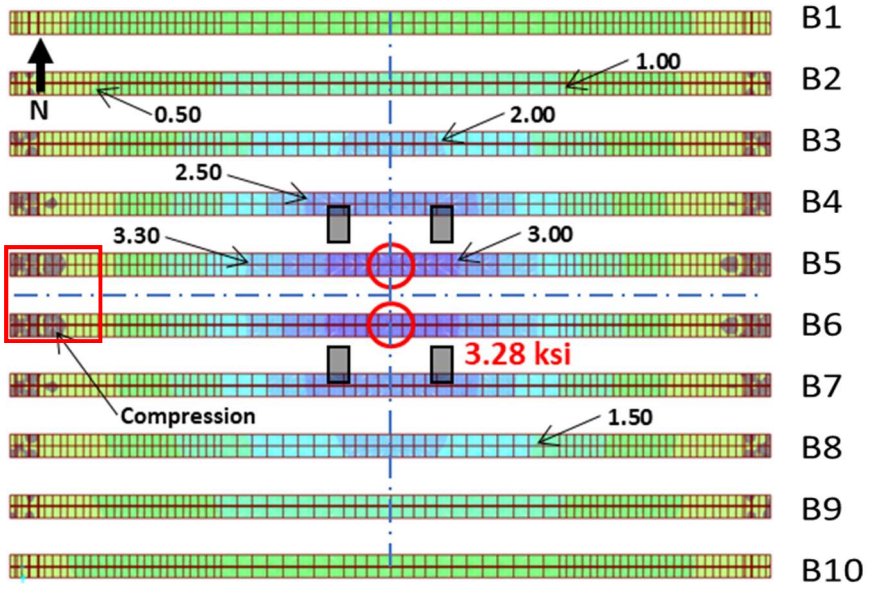

Figure 13. Longitudinal stress distribution on flange bottom of steel tee sections (Model 4: Transverse Position 1, Longitudinal Position 3). Test truck wheel loads in black. Maximum values shown in red with position circled. Compressive stress in grey.

Figure 14 shows a close-up view of the ends of the two steel tee sections (B5 and B6) near the centerline of the bridge (small area boxed in red). The image shows some localized flange plate bending zones (small green tension regions surrounded by grey compressive stress regions) at and near the bearing pads (shown by blue rectangles) that appear to be artificial results from details of the spring supports used to model the bearing pads. Outside of the bearing pad region a large bulb-shaped (grey) zone of compressive stress (in the longitudinal direction) of the flange is observed. These compressive stresses from primary negative bending were also present during the controlled-load testing as measured by strain gauges installed at these locations.

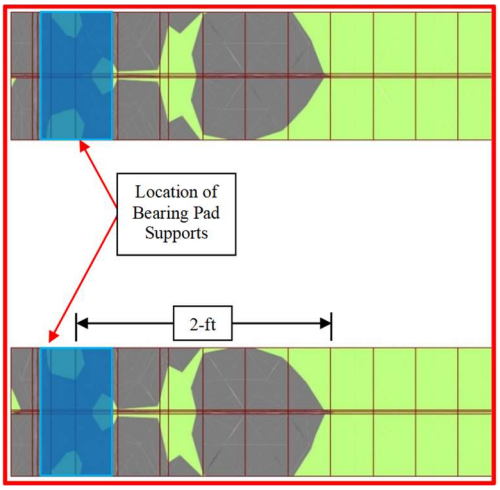

Figure 14. Longitudinal stress on flange bottom of steel tee sections showing negative moment (Solid Model: Transverse Position 1, Longitudinal Position 3). Compressive stress in grey.

In summary, based on FEA results, strain gauges were installed at selected locations on the inverted steel tee sections: some locations were on the bottom of the flange, and other locations were on the web at different elevations. Strain gauges were also installed at selected locations on the bottom of the concrete deck (in both the longitudinal and transverse directions). Displacement sensors were attached near the interface between the steel tee section web and bottom of the concrete deck to measure relative displacement in the longitudinal direction.

2.5. Details of As-Installed Sensor Locations

From a systematic study of the FEA results (for the load positions described above) the final instrumentation plan was developed (see Figure 10), which included a total of 36 sensors. Unfortunately, due to unanticipated moisture conditions on the bottom of the concrete deck, one concrete strain gauge (longitudinal strain gauge: S21-Deck) could not be installed. Thus, the number of sensors used during controlled-load testing of the Flex Beam bridge was 35.

The final instrumentation plan is summarized in Table 2. A total of 21 strain gauges were installed on the steel tee sections, 8 strain gauges were installed on the bottom of the concrete deck, and 6 displacement transducers were installed at the interface between the steel tee section webs and the bottom of the concrete deck. Each sensor is associated with a designated steel tee section ("B#") or the concrete deck ("DK_#_#") if the sensor is on the deck between adjacent steel tees and is given as the prefix for sensor labeling. Table 2 shows the identifier for each sensor, which has a suffix depending on the sensor type ("SG#" for "strain gauge" or "DISP" for "displacement transducer"). The table lists the surface(s) each sensor is attached to. The location of the gauge relative to the global geometry of the bridge is also provided in the sensor labeling ("CL" for "centerline", "E" for "east bearing", "W" for "west bearing", and "QTR" for "quarter span"). The steel tee designations and sensor layout are also shown in Figure 10, where symbols indicate the sensor type and location.

From observations and measurements of the as-constructed bridge, it was noted that the bearing stiffener plates are accurately aligned with the centerline of the bearing pads, thus the span of the bridge was taken as the centerline stiffener-to-stiffener distance. The longitudinal locations of the sensors were measured from the centerline of either the east or west bearing stiffener plate, depending on which half of the bridge the sensor is located in (east or west half of the bridge span). For consistency, all sensors at the centerline of the span were located by measuring from the west bearing stiffener plate. Table 2 indicates the bearing stiffener plate that was used to measure the sensor location (either "E" for east stiffener plate or "W" for west stiffener plate).

Figure 15 shows typical sensor locations on a transverse view of a composite steel tee section (i.e., a longitudinal section). Note that this figure does not show a typical layout of sensors at a single longitudinal location; it shows only the typical vertical locations on the steel tee section and concrete deck. The relative displacement in the longitudinal direction between the concrete deck and steel tee web was measured by displacement transducers attached to the web and the bottom of the deck, as shown in the figure. The figure also shows adjacent bonded strain gauges, placed with one on the steel tee web and the other on the concrete deck bottom, which were used to evaluate composite action between the deck and web.

Figure 16 shows the typical sensor locations on a transverse section through two composite steel tee sections. Note that this figure does not show a typical layout of sensors at a single longitudinal location; it shows only the typical vertical and transverse locations on the steel tee section and concrete deck. Note that the concrete deck longitudinal strain measurements were made at a few locations and concrete deck transverse strains were made at one location between two steel tee sections (with longitudinal strain measured at the same location).

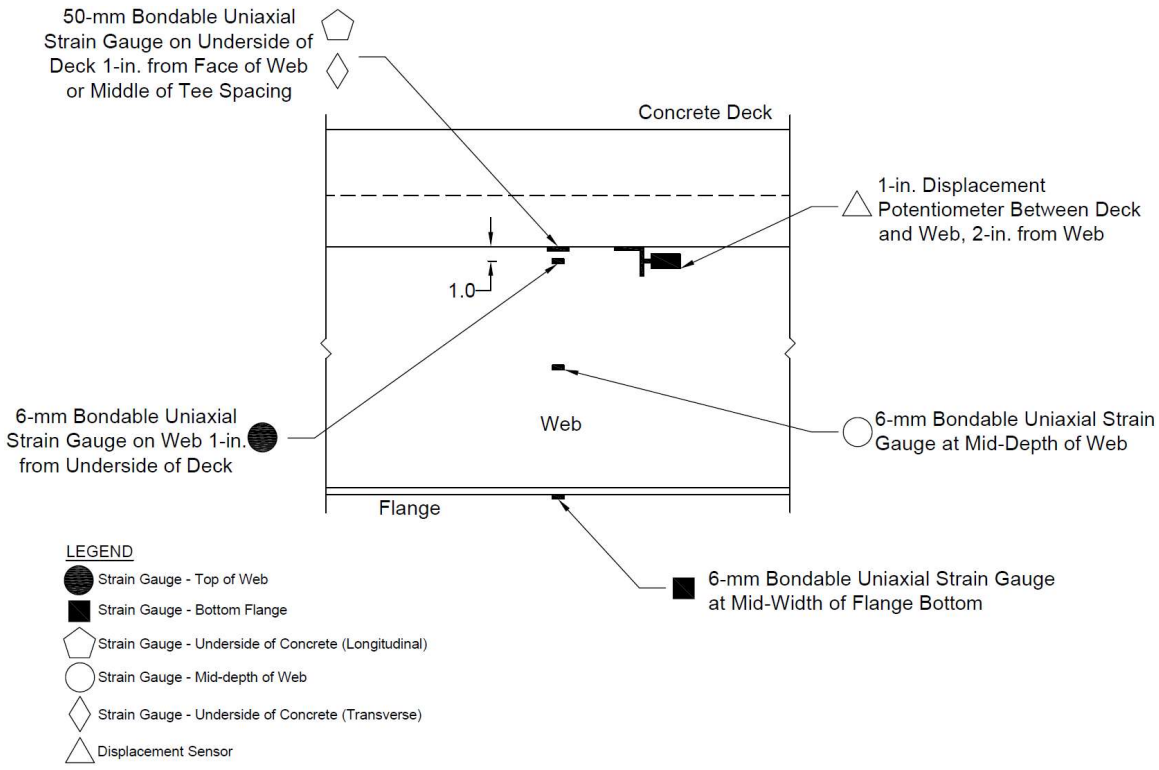

Figure 15. Typical sensor locations (longitudinal section, transverse view).

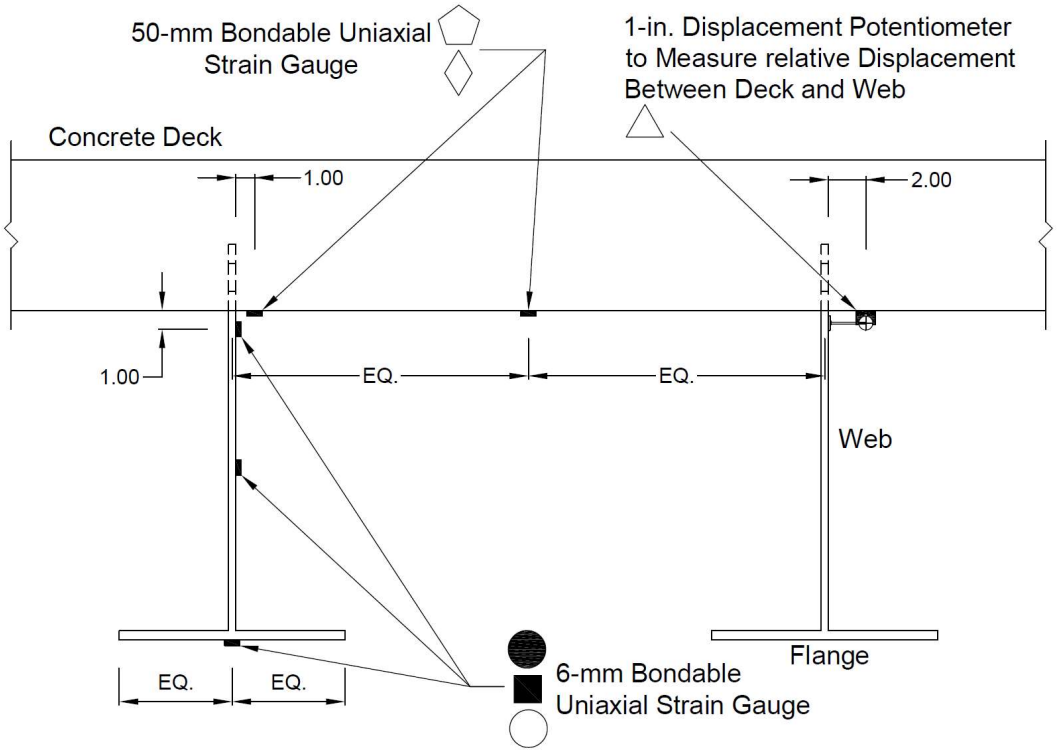

Figure 16. Typical sensor locations (transverse section, longitudinal view).

Table 2. Final Instrumentation Plan.

Sensor Identifier	Associated Steel Tee	Attached Surface	Sensor Type	Distance from CL of Stiffener Plate (in.)	Location Detail	Intended Measurement
B2_W_SG1	B2	Tee Flange	Strain Gauge	16 (W)	Mid Flange Width	Flange Stress
B2_QRT_SG1	B2	Tee Flange	Strain Gauge	96 (W)	Mid Flange Width	Flange Stress
B1_CL_SG1	B1	Tee Flange	Strain Gauge	192 (W)	Mid Flange Width	Flange Stress
B2_CL_SG1	B2	Tee Flange	Strain Gauge	192 (W)	Mid Flange Width	Flange Stress
B2_CL_SG2	B2	Deck Bottom	Strain Gauge	192 (W)	Near Tee Web	Composite
B2_CL_SG3	B2	Tee Web	Strain Gauge	192 (W)	Near Deck Bottom	Composite
B2_CL_SG4	B2	Tee Web	Strain Gauge	192 (W)	Mid Web Depth	Stress Gradient
DK_2_3_SG2	Mid B2-B3	Deck Bottom	Strain Gauge	16 (W)	Mid Tee Spacing	Deck Stress
B3_CL_SG1	B3	Tee Flange	Strain Gauge	192 (W)	Mid Flange Width	Flange Stress
B4_CL_SG1	B4	Tee Flange	Strain Gauge	192 (W)	Mid Flange Width	Flange Stress
B4_CL_SG2	B4	Deck Bottom	Strain Gauge	192 (W)	Near Tee Web	Composite
B4_CL_SG3	B4	Tee Web	Strain Gauge	192 (W)	Near Deck Bottom	Composite
B5_QRT_SG1	B5	Tee Flange	Strain Gauge	96 (W)	Mid Flange Width	Flange Stress
B2_W_SG1	B5	Tee Flange	Strain Gauge	16 (W)	Mid Flange Width	Flange Stress
B5_W_SG2	B5	Deck Bottom	Strain Gauge	16 (W)	Near Tee Web	Composite
B5_W_SG3	B5	Tee Web	Strain Gauge	16 (W)	Near Deck Bottom	Composite
DK_4_5_SG2	Mid B4-B5	Deck Bottom	Strain Gauge	192 (W)	Mid Tee Spacing	Deck Stress
DK_4_5_SG5	Mid B4-B5	Deck Bottom	Strain Gauge	192 (W)	Mid Tee Spacing	Deck Stress
B5_CL_SG1	B5	Tee Flange	Strain Gauge	192 (W)	Mid Flange Width	Flange Stress
B5_CL_SG3	B5	Tee Web	Strain Gauge	192 (W)	Near Deck Bottom	Composite
B5_CL_SG4	B5	Tee Web	Strain Gauge	192 (W)	Mid Web Depth	Stress Gradient
B6_W_SG1	B6	Tee Flange	Strain Gauge	16 (W)	Mid Flange Width	Flange Stress
DK_5_6_SG2	Mid B5-B6	Deck Bottom	Strain Gauge	192 (W)	Mid Tee Spacing	Deck Stress
B5_E_SG1	B5	Tee Flange	Strain Gauge	16 (E)	Mid Flange Width	Flange Stress
B5_E_SG2	B5	Deck Bottom	Strain Gauge	16 (E)	Near Tee Web	Composite
B5_E_SG3	B5	Tee Web	Strain Gauge	16 (E)	Near Deck Bottom	Composite
B6_CL_SG1	B6	Tee Flange	Strain Gauge	192 (W)	Mid Flange Width	Flange Stress
B8_CL_SG1	B8	Tee Flange	Strain Gauge	192 (W)	Mid Flange Width	Flange Stress
B9_CL_SG1	B9	Tee Flange	Strain Gauge	192 (W)	Mid Flange Width	Flange Stress
B2_W_DISP	B2	Deck & Web	Transducer	16 (W)	Web-Deck Interface	Shear Slip
B2_QRT_DISP	B2	Deck & Web	Transducer	96 (W)	Web-Deck Interface	Shear Slip
B5_W_DISP	B5	Deck & Web	Transducer	16 (W)	Web-Deck Interface	Shear Slip
B5_QRT_DISP	B5	Deck & Web	Transducer	96 (W)	Web-Deck Interface	Shear Slip
B5_CL_DISP	B5	Deck & Web	Transducer	192 (W)	Web-Deck Interface	Shear Slip
B5_E_DISP	B5	Deck & Web	Transducer	16 (E)	Web-Deck Interface	Shear Slip

"SG": Strain Gauge

"E": Measured from East Abutment

"DISP": Displacement Sensor

"W": Measured from West Abutment

Instrumentation was installed on the bridge (i.e., installation of the sensors, wiring/cables, solar power system, and data acquisition system) over a three-day period (September 12-14, 2022) by a four-person team from the ATLSS Research Center at Lehigh University (see Figure 17). The installation of sensors, wiring/cables, solar power system, and data acquisition equipment was performed directly from the ground (or using a small step ladder or low scaffold).

Figure 17. Installation of sensors and wiring/cables on Flex Beam demonstration bridge.

As noted above, displacement sensors were positioned to measure relative displacement between the concrete deck and inverted steel tee section (see Figure 18). Two sensors (on B2 and B5) were placed near the west bearing. Two additional sensors were placed on B2 and B5 at the west quarter point of the span. Additional displacement sensors were placed on B5, with one at the centerline (mid-span) and the other near the east bearing. These displacement sensors provide measurements of relative displacement (for example, from possible shear slip) along the length of one steel tee section that is near mid width (i.e., the centerline) of the bridge. The bodies of the displacement sensors were attached to the web of the steel tee sections and targets for the plungers of the displacement sensors were attached to the bottom of the concrete deck. A positive value from these displacement sensors means that the deck moves to the west (at the location of the instrument) relative to the web and a negative value means that the deck moves to the east relative to the web.

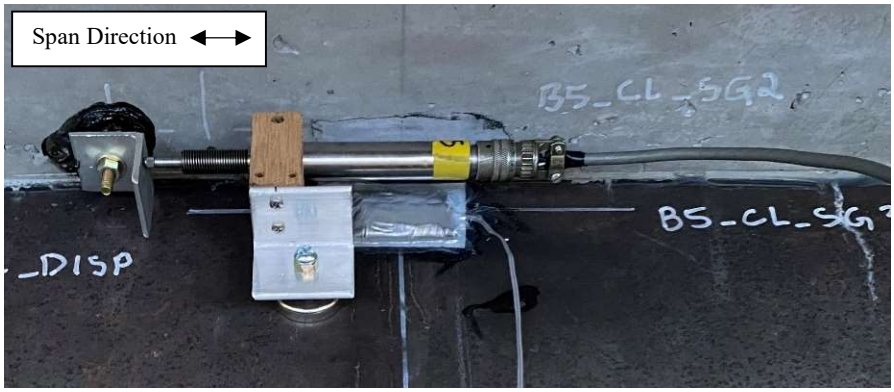

Figure 18. Displacement transducer measuring relative displacement).

Weather proofing was applied to all strain gauges; thus, the images of the strain gauges in the report show the silver protective tape and water sealant silicone that cover the strain gauge (a black double headed arrow is added to the images to show the direction of measurement for the covered strain gauge). Figure 19 shows a location with a strain gauge installed on bottom of the flange (mid flange width) to measure longitudinal strain (from flexure). This strain gauge is placed at the mid-span of B4. The maximum values of flexural stress were expected on the flange bottom at mid-span. To measure these largest stresses and to characterize

the flexural stress distribution across the bridge, a total of eight steel tee sections had strain gauges at mid-span (i.e., B1, B2, B3, B4, B5, B6, B8, and B9). The flange bottom of the tee sections of B2 and B5 also had strain gauges at the west quarter point to observe the longitudinal bending moment variation.

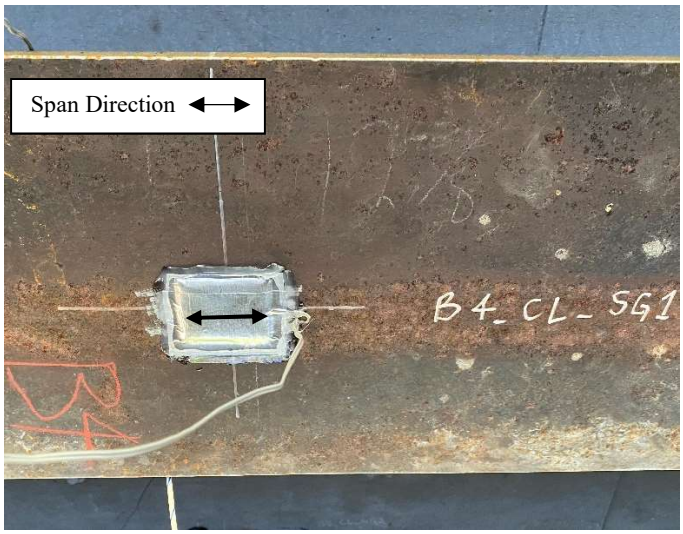

Figure 19. Strain gauge on bottom of flange of tee component (B4_CL_SG1).

A number of strain gauges were positioned near the bearings to measure the negative bending (i.e., bending reversal) observed in the FEA results. Strain gauges were placed on the flange bottom of B2 and B5 near the west bearing, and on the flange bottom of B5 near the east bearing (see Figure 20). Figure 20 also shows displacement transducers near the bearings.

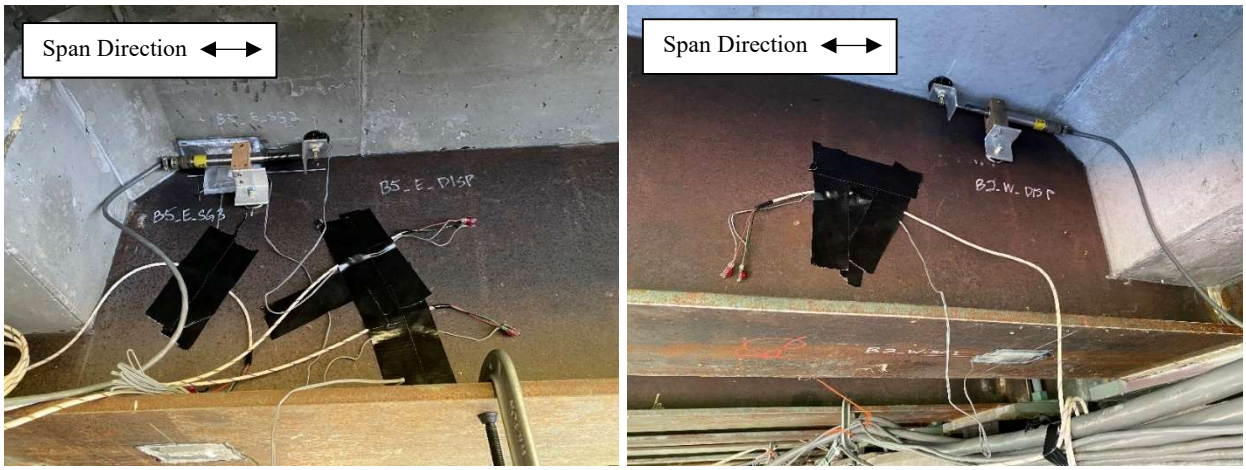

Figure 20. Left: Strain gauges on bottom of flange, top of web, and concrete deck bottom and displacement transducer near east bearing (B5_E). Right: Strain gauge on bottom of flange and displacement transducer near west bearing (B2_W).

Figure 21 shows the strain gauges installed at mid-span of the bridge to measure the stress gradient over the depth of steel tee section B2. As shown in the figure, strain gauges were installed on the steel tee near the bottom of the deck, mid-depth of the exposed steel tee web, and on the bottom of the flange. This strain gauge arrangement is repeated on B5. As previously mentioned, these measurements allow assessment of the plane-section assumption and transformed-section model used in the design of the Flex Beam system. Figure 22 shows a strain gauge pair (one on bottom of the concrete deck and another on the adjacent steel tee web). Data from these strain gauges, in combination, are intended to assess the composite action of the Flex Beam system; with full composite action, the measured data from these two strain gauges should be

similar. This strain gauge configuration was installed at mid-span of B2 and B4 at mid-span, and near the west and east bearings of B5.

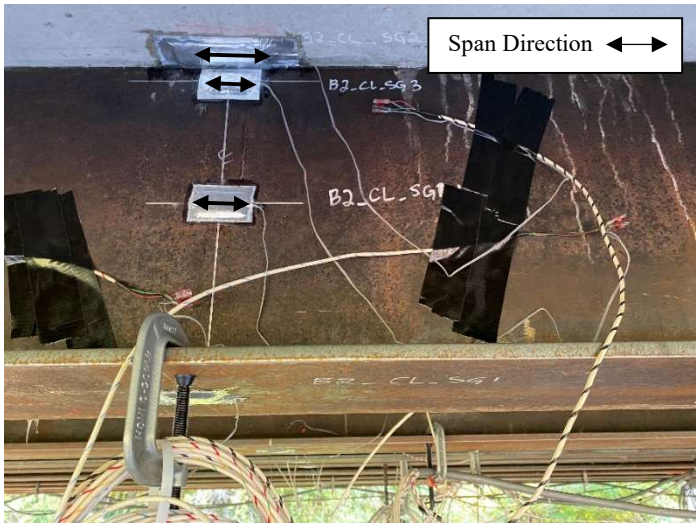

Figure 21. Strain gauges installed over depth of steel tee section (B2_CL_SG2, SG3, & SG4).

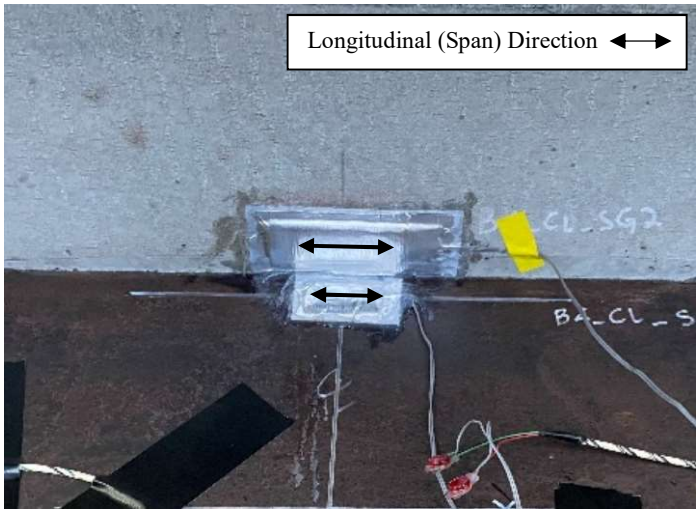

Figure 22. Strain gauges at bottom of deck and adjacent steel tee web (B4_CL_SG2 & SG3).

At several locations between steel tee sections, concrete strain gauges were applied to the bottom of the deck. At these locations, the strain gauges were centered between the tee sections. These gauges are located at mid-span between B2 and B3, between B4 and B5, and between B5 and B6. Between B4 and B5, two gauges were installed with one measuring longitudinal strain and the other measuring transverse strain (see Figure 23). At the other two locations, gauges were used in the longitudinal direction only.

Figure 23. Bottom of deck gauges centered between steel tee sections (transverse and longitudinal) (DK_4_5_SG2 and SG5).

Figure 24 shows views under the bridge after all of the sensors and wiring/cables were installed. Figure 25 shows the bridge (viewed facing south).

Figure 24. Underside of instrumented bridge. Left: Facing east. Right: Facing west.

Figure 25. Underside of instrumented bridge (facing south).

2.6. Descriptions of Sensors

The strain gauges used on steel tee sections were uniaxial bondable resistance-type strain gauges with a gauge length of 6 mm (0.24 in.) and resistance of 120 ohms. These gauges, model FLAB-6-11-3LJC-F, were manufactured by Tokyo Measuring Instruments Laboratory, (see Figure 26). The strain gauges were used in a quarter-bridge configuration with an excitation voltage of 5 volts. A bondable strain gauge type was selected due to the capability to measure relatively small strain values since the stresses from the FEA results were relatively small (with the largest stresses in the range of 3 to 4 ksi). The steel surface was prepared by degreasing and grinding to remove any paint and surface corrosion. The area was then textured to a certain roughness, as needed to adhere the strain gauge, using emery paper. After a final cleaning, each gauge was applied using a specialized strain gauge adhesive (CN cyanoacrylate adhesive).

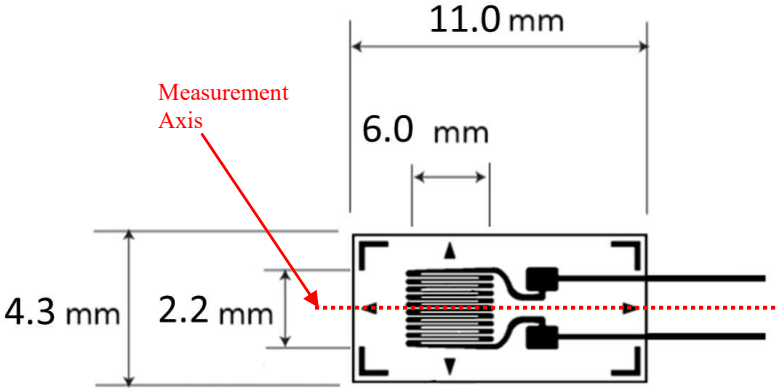

Figure 26. Steel bondable strain gauge.

The strain gauges on the bottom of the concrete deck were uniaxial bondable resistance-type strain gauges manufactured by Tokyo Measuring Instruments Laboratory, model PL-60-11-3LJC-F with a 60 mm (2.4 in.) gauge length (see Figure 27). These gauges have a resistance of 120 Ohms and were used in a quarter-bridge configuration with an excitation of 5 volts. The concrete surface was first prepared by grinding to create a textured surface for an epoxy (J-B Weld Bonder, Urethane, Model No. 50139) base. The epoxy base was then textured with emery paper to the appropriate roughness. After a final cleaning, each gauge were applied using the same adhesive used for the gauges on the steel tee sections.

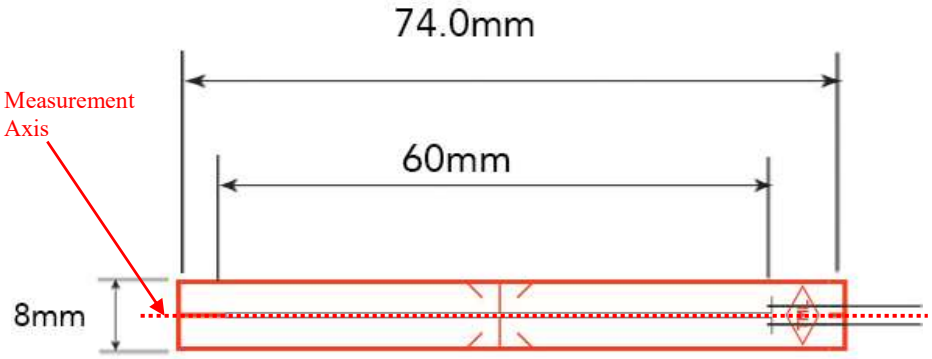

Figure 27. Concrete bondable strain gauge.

The displacement sensors were spring-loaded Linear Variable Differential Transformers (LVDTs) manufactured by Macro Sensors, Inc., model GHSD-750-250 (see Figure 28). These sensors have a total stoke of 0.5 in (±0.250 in.).

Figure 28. Displacement sensor.

2.7. Data Acquisition Equipment

Data were collected using a Campbell Scientific CR9000 Data Logger, which is a high-speed, multi-channel, 16-bit digital data acquisition system. To ensure a stable, noise-free signal, analog and digital filtering was employed as data were recorded.

The data logger was housed in a steel job box adjacent to the north-west corner of the bridge, near the west abutment. Figure 29 shows the site with locations outlined for the data logger and power systems. The data logger job box is shown in Figure 30 and Figure 31.

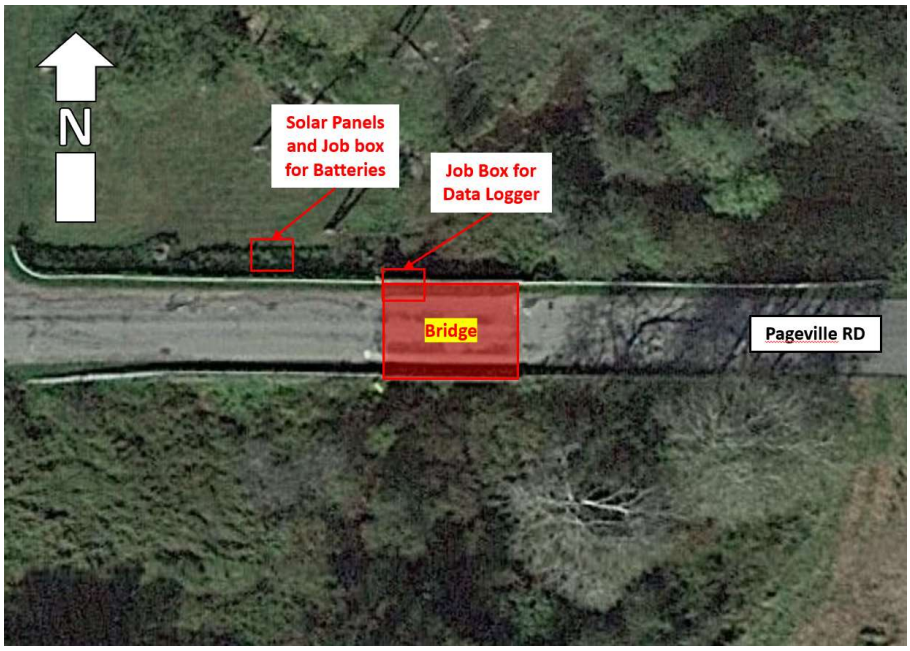

Figure 29. Bridge site plan showing locations of instrumentation equipment.

Wires originating from the sensors were bundled into trunk cables which ran from the bridge to the data logger, with each trunk cable designated for a particular set of data logger channels. The truck cables were assigned to particular set of data logger filter cards (each filter card has six channels, and the data logger was configured with six filter cards for a total of 36 channels).

Figure 30. Job box housing data logger equipment.

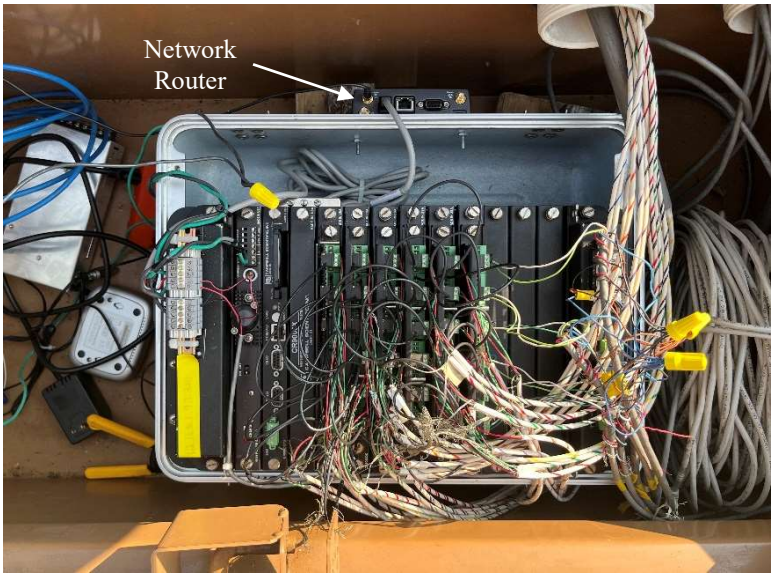

Figure 31. Campbell Scientific CR9000 data logger and sensor gauge wiring inside the job box.

Data were collected at a rate of 100 samples per second during controlled-load testing and during several weeks of monitoring of the typical vehicular-load response. Data were viewed on-site by connecting the data logger directly to a laptop computer. This configuration was used to manually start and stop data collection during controlled-load testing. At the conclusion of each controlled-load test, data were downloaded to the laptop computer from the onboard memory of the data logger.

The data logger is autonomous and does not need continuous direct communication to collect data. A wireless modem was connected to the data logger to enable remote downloading of monitoring data. Unfortunately, due to very poor wireless network signal in the area where the bridge is located, a remote connection to the data logger was not possible. Therefore, data from several weeks of monitoring were downloaded to a laptop computer after the monitoring phase ended. As mentioned earlier, the sensors used for several weeks of monitoring was reduced to 12 strain gauges (2 filter cards) to reduce the demand on the solar power system.

2.8. Electric Power System

During the controlled-load testing, which was performed during one day, electric power for the data acquisition equipment was provided on-site by a portable gas-powered generator. For several weeks of monitoring of typical vehicular-load response, a solar power system was used, which consisted of solar panels and a battery storage system. As shown in Figure 32, two solar panel units, one with three panels connected in series and the other with two panels, form part of the system. The solar panels were mounted on hollow circular steel tubes embedded in the ground with concrete. A job box shown in Figure 32 housed a power system controller and 18 sealed deep-cycle 12V batteries connected in parallel. The interior of this job box is shown in Figure 33. Figure 34 shows the complete data acquisition and solar power system.

Figure 32. Solar panels and job box for solar power system.

Figure 33. Solar power system batteries and controller inside job box (12 additional batteries are underneath white shelf).

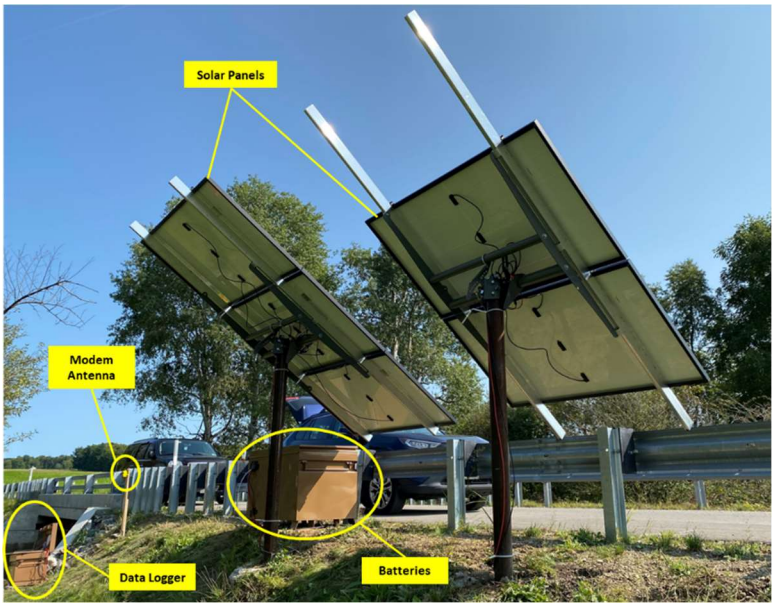

Figure 34. Complete data acquisition and solar power system.

2.9. Controlled-Load Testing Procedure

A series of controlled-load tests were conducted using a fully loaded tri-axle dump truck, denoted the *Actual Test Truck* (ATT) and described earlier. Prior to testing the ATT was weighed by a Pennsylvania State Police Weight Enforcement team using calibrated scales. The axle spacings and tracks were measured on-site. The ATT data is given in Figure 8, and the ATT is shown in Figure 7. The GVW of the ATT was 77,550 lb. The ATT was the only vehicle on the bridge during controlled-load testing. Traffic was stopped at either end of the bridge the tests and traffic queues were cleared between tests.

The controlled-load tests were performed on September 15, 2022. Moving vehicle tests were conducted with the test truck passing over the bridge at either crawl speed (i.e., *Crawl* tests providing a pseudo-static response) or the posted speed limit (i.e., *Dynamic* tests providing a dynamic response). During each moving vehicle test, the test truck was driven completely across the bridge while maintaining a specified transverse position and speed, and data were collected from the sensors on the bridge. Static load tests (i.e., *Park* tests) were conducted by parking the test truck at specified positions on the bridge, while data were collected from the sensors on the bridge. During each test, data were collected at a rate of 100 samples per second.

The controlled-load tests are summarized in Table 3, which lists a total of 29 *Park*, *Crawl* and *Dynamic* tests. The individual tests are numbered sequentially in the order that they were performed. 21 tests were performed with the truck moving in the westbound direction and 8 tests were performed with the truck moving in the eastbound direction. Westbound crawl and dynamic tests were performed with the test truck in one of three transverse positions (bridge mid-width, mid-lane, and 2 ft. from the north parapet). Eastbound tests used only the single mid-lane transverse position. Each crawl test was performed twice to assess the repeatability of the results. Dynamic tests were performed twice in each lane, while a single park test was performed for each specified position.

Each crawl test began with the test truck completely off the bridge. Then the truck moved across the bridge span, and the test concluded when the rear tandem axle was completely off the bridge. For each dynamic test, the test truck reached the posted speed before the front axle reached the bridge and maintained that speed until the rear tandem axle was off the bridge. For each park test, the test truck was positioned, as accurately as possible, at each specified position. The truck was parked at the specified position for approximately 15-20 seconds. Data was recorded while the test truck drove onto the bridge, parked, and drove off the bridge.

Table 3. Summary of controlled-load tests.

Test No.	Test Truck Direction of Travel	Test Type	Transverse Position	Longitudinal Position
1	Westbound	Crawl	(**1**) Mid-Width	Entire Span
2	Westbound	Crawl	(**1**) Mid-Width	Entire Span
3	Westbound	Crawl	(**2**) Mid-Lane	Entire Span
4	Westbound	Crawl	(**2**) Mid-Lane	Entire Span
5	Westbound	Crawl	(**3**) 2 ft from Parapet	Entire Span
6	Westbound	Crawl	(**3**) 2 ft from Parapet	Entire Span
7	Westbound	Dynamic	(**1**) Mid-Width	Entire Span
8	Westbound	Dynamic	(**1**) Mid-Width	Entire Span
9	Westbound	Dynamic	(**2**) Mid-Lane	Entire Span
10	Westbound	Dynamic	(**2**) Mid-Lane	Entire Span
11	Westbound	Dynamic	(**3**) 2 ft from Parapet	Entire Span
12	Westbound	Dynamic	(**3**) 2 ft from Parapet	Entire Span
13	Westbound	Park	(**1**) Mid-Width	(**2A**) Front Axle of Tandem Aligned on Bearing
14	Westbound	Park	(**2**) Mid-Lane	(**2A**) Front Axle of Tandem Aligned on (Bearing
15	Westbound	Park	(**3**) 2 ft from Parapet	(**2A**) Front Axle of Tandem Aligned on Bearing
16	Westbound	Park	(**1**) Mid-Width	(**1**) Truck Centered in Span
17	Westbound	Park	(**2**) Mid-Lane	(**1**) Truck Centered in Span
18	Westbound	Park	(**3**) 2 ft from Parapet	(**1**) Truck Centered in Span
19	Westbound	Park	(**1**) Mid-Width	(**3**) Tandem Axle Centered in Span
20	Westbound	Park	(**2**) Mid-Lane	(**3**) Tandem Axle Centered in Span
21	Westbound	Park	(**3**) 2 ft from Parapet	(**3**) Tandem Axle Centered in Span
22	Eastbound	Crawl	(**2**) Mid-Lane	Entire Span
23	Eastbound	Crawl	(**2**) Mid-Lane	Entire Span
24	Eastbound	Dynamic	(**2**) Mid-Lane	Entire Span
25	Eastbound	Dynamic	(**2**) Mid-Lane	Entire Span
26	Eastbound	Park	(**2**) Mid-Lane	(**2B**) Rear Axle of Tandem Aligned on Bearing
27	Eastbound	Park	(**2**) Mid-Lane	(**1**) Truck Centered in Span
28	Eastbound	Park	(**2**) Mid-Lane	(**3**) Tandem Axle Centered in Span
29	Eastbound in Westbound Lane	Park	(**2**) Mid-Lane	(**2B**) Rear Axle of Tandem Aligned on Bearing

2.10. Process for Monitoring of Typical Vehicular-Load Response

Monitoring of the typical vehicular-load response of the bridge was also performed. Due to electric power limitations, only two filter cards with up to 12 strain gauges were available for the monitoring. As mentioned earlier, 12 strain gauges were selected for typical vehicular-load response monitoring; these strain gauges are at locations shown in Figure 35. These gauges were selected after review of data from the controlled-load testing. The relative displacement measurements were very small when the bridge was loaded with the heavy ATT, thus, the displacement sensors were not included in the monitoring of the typical vehicular-load response.

The 12 gauges selected for monitoring were expected to provide data to characterize the mid-span flexural response of the composite steel tee sections, the load distribution among the composite steel tee sections, and the stress gradient in the composite steel tee sections to validate a plane-section assumption. Strain gauges on the flange bottom at mid-span of steel tee sections B1, B2, B3, B4, B5, B6, B8, and B9 were

selected to characterize mid-span flexural response and load distribution. Also, at mid-span of B5, the strain gauge at the mid-depth of the (exposed) web was included to validate the plane-section assumption.

In addition, the strain gauge on the flange bottom of B5 near the west abutment was included to see if negative (reverse) bending was observed under typical vehicular loading. Lastly, two strain gauges on the bottom of the concrete deck, between B4 and B5, were included (one measuring longitudinal strain and the other measuring transverse strain).

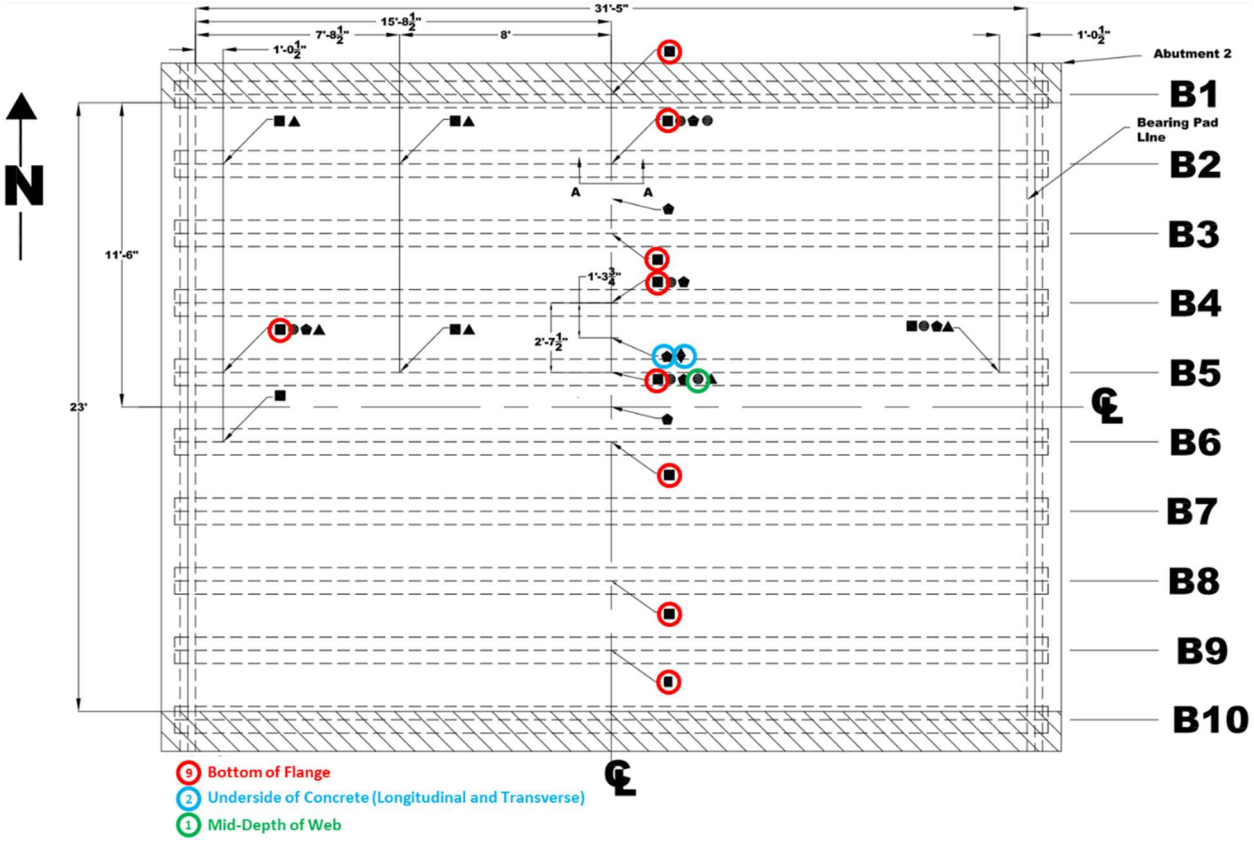

Figure 35. Sensors (strain gauges) selected for monitoring phase of the project.

Monitoring of the typical vehicular-load response of the bridge was included for comparison with the controlled-load testing response. For several weeks of monitoring, the data logger was programmed to record time-history data from the 12 strain gauges. The specifics of the data collection algorithm are as follows.

During the dynamic controlled-load tests, a sampling rate of 100 Hz was used to accurately capture the maximum responses. However, continuous recording at 100 Hz of time-history data over several weeks of monitoring would result in an unmanageable quantity of data. Therefore, data were recorded only for a limited duration of time when the measured response at selected strain gauges exceeded predefined trigger values. The strain gauges used for the trigger conditions are located on the flange bottoms at mid-span of steel tee sections B3 and B8. Strain time-history data were recorded when the strain at either one of these two gauges exceeded the strain value corresponding to 0.25 ksi (i.e., (0.25 ksi)/E = 8.62 microstrain). With these trigger conditions, a heavy vehicle in either the eastbound or westbound lane could trigger the data logger. When a trigger condition was met, the data logger was programmed to record high speed data (at 100 Hz) from all sensors for 1 second before the strain exceeds the trigger level and 1 second after the strain drops below the trigger level. The trigger level of 0.25 ksi was selected to limit the amount of data collected. The goal of the triggering procedure was to capture the response caused by the heaviest vehicles crossing the bridge.

2.11. Summary

Instrumentation and controlled-load testing plans were presented in this chapter. Based on initial FEA work (pre-test analyses) the bridge instrumentation and controlled-load testing plans were developed. The instrumentation was intended to provide data useful to assess the load distribution among the composite steel tee sections, and to assess the stress response of the composite steel tee sections. Results from the controlled-load testing and monitoring are discussed in the next chapter.

CHAPTER 3: FIELD TESTING RESULTS

3.1. Background

The data from controlled-load load testing and monitoring of the typical vehicular-load response of the Flex Beam demonstration bridge are presented in this chapter.

3.2. Controlled-Load Testing

As described in Chapter 2, instrumentation was installed on the Flex Beam bridge and a test plan was developed, based on finite element analysis (FEA) results. Controlled-load testing was performed on the morning of September 15, 2022. Immediately prior to the controlled-load testing, the road was marked with high-visibility tape to indicate the specified positions of the test truck (see Figure 36). The test truck driver positioned the truck as close as possible to the specified transverse and longitudinal positions, with guidance provided by the Lehigh University research team.

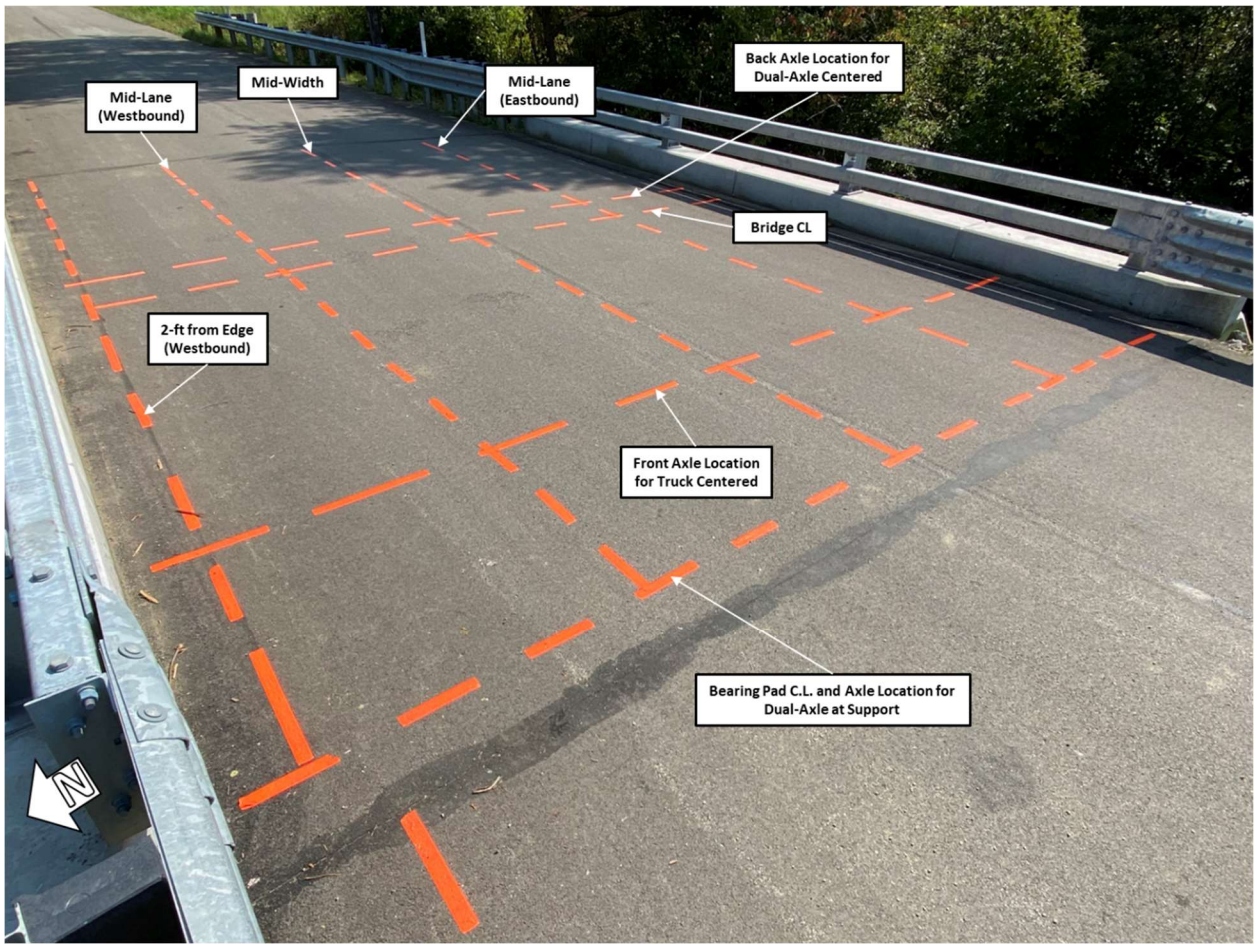

Figure 36. Road layout markings for controlled-load testing.

Crawl tests were performed first, to establish the pseudo-static response of the bridge as the test truck moves across the bridge span at a slow speed with a constant transverse position. During a crawl test, the speed of the test truck was 3 to 5 mph (see Figure 37) with the test starting with the truck approximately 1 ft before the bridge and the test finishing when the truck was completely off the bridge. Three tests were performed in the westbound direction and one in the eastbound direction. Each crawl test was performed two times to assess the repeatability of the data. The results of the repeated tests were found to be similar.

Figure 37. Crawl test procedures during controlled load testing. Left: Transverse Position 1, Westbound. Right: Transverse Position 2, Westbound.

Dynamic tests were performed next, to assess the level of response amplification from the test truck moving across the bridge at the posted speed limit with a constant transverse position. During a dynamic test, the speed of the test truck was approximately 25 mph with the test starting with the truck at a significant distance from the bridge in order to reach the specified speed before reaching the bridge. Three tests were performed in the westbound direction and one in the eastbound direction. Each dynamic test was performed twice and the results from the repeated tests were found to be similar.

Lastly, the park tests were performed to determine the static response of the bridge with the test truck at a known position on the bridge. During a park test, the test truck was parked at a specified transverse and longitudinal position on the bridge for a period of at least 15 seconds while data from instrumentation on the bridge were recorded. After aligning the truck along the specified transverse position, the truck moved onto the bridge at crawl speed (3-5 mph) and stopped at the specified longitudinal position, remained there for approximately 15-20 seconds, and then moved forward at crawl speed off the bridge (see Figure 38 and Figure 39). The data acquisition system (data logger) established a new zero reference prior to each park test. Nine park tests were performed in the westbound direction and four in the eastbound direction. Each park test was performed only once.

Figure 38. Park test procedure. Left: Transverse Position 2, Longitudinal Position 1. Right: Transverse Position 2, Longitudinal Position 3.

Figure 38 shows a park test with the truck in the westbound direction in the mid-lane transverse position (Transverse Position 2). The left image shows the truck centered in the span (Longitudinal Position 1),

while the right image shows the truck with the tandem axle centered in the span and the front axle off the bridge (Longitudinal Position 3). The left image in Figure 39 shows the truck facing westbound in the mid-lane transverse position (Transverse Position 2), with the front axle of the tandem aligned with the centerline of the west bearing (with the rear axle of the tandem on the bridge and the front axle off the bridge, i.e., Longitudinal Position 2A), while the right image shows the truck in the mid-lane transverse position (Transverse Position 2, in the westbound lane with the truck facing eastbound) with the rear tandem axle centered above the west bearing and the entire truck on the bridge (with both the front tandem axle and the front axle on the bridge, i.e., Longitudinal Position 2B). The park position shown in the right image of Figure 39 (Test 29) is the position that yields the largest reactions at the bearings at one (west) end of the bridge, and corresponds to the largest theoretical vertical shear forces in the bridge. Since the test truck was oriented in the eastbound direction after conducting tests 26, 27, and 28 (which are in the eastbound direction of the roadway), and since the bridge is relatively symmetrical about both its longitudinal and transverse axes, it was decided to conduct Test 29 with the test truck facing eastbound in the westbound lane.

Figure 39. Park test procedure. Left: Transverse Position 2, Longitudinal Position 2A. Right: Transverse Position 2 (eastbound in westbound lane), Longitudinal Position 2B.

3.2.1. Controlled-Load Testing Results

A summary of the results from controlled-load testing is presented in this section. This summary focuses on tests with the same transverse position (Transverse Position 1).

3.2.1.1. Park Tests

Nine park tests were conducted. Figure 40 provides the strain time-history responses for the flange bottom at mid-span of each instrumented composite steel tee section during park Test 19, with the test truck at mid-width of the bridge and the tandem axle centered in the span (Transverse Position 1, Longitudinal Position 3). Figure 40 shows the progression of the test truck during the test after data collection was initiated at time equal to zero. After the front axle moved onto the bridge and moved forward there is a rise in the mid-span flange strain responses starting at approximately 23 seconds. Local maxima in the responses can be seen at approximately 31 seconds. The local maxima occur as the front axle of the truck passes over mid-span as the truck is moving to the specified longitudinal position. Larger local maxima are observed for gauges located near the test truck transverse position on the bridge (i.e., the strain gauges near the bridge mid-width are on the flanges of B4, B5, and B6). After the local maxima, the strains decrease, then increase until the tandem axle reached mid-span, when the data shows small oscillations as the truck came to a stop at the specified longitudinal position for the park test, producing vibration of the bridge. There is period of relatively constant strain as the test truck remained parked. The strains decrease as the truck moved off the bridge, and the test was concluded. For all park tests, the same procedure was followed. To establish

consistent park test results for strains and relative displacements, the data was averaged over a period of time when the test truck was parked (a duration of 10 seconds was used).

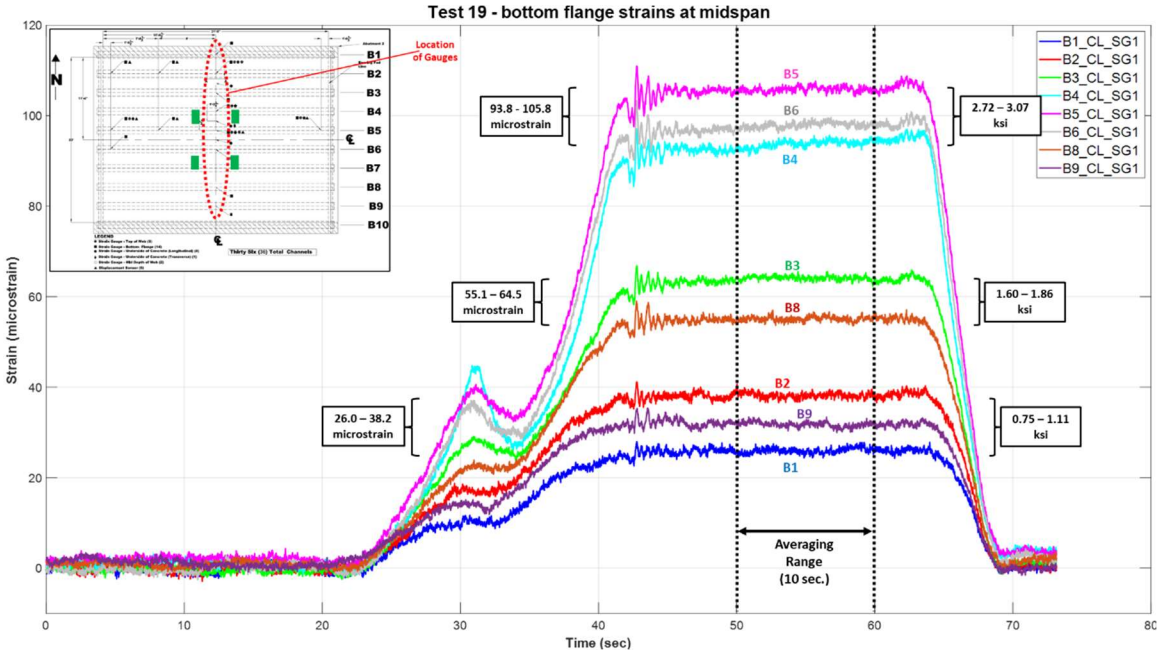

Figure 40. Park Test 19: Strain time-history responses on bottom of flanges at mid-span.

Figure 41 shows the responses of the mid-span strain gauges through the depth of composite steel tee section B5 for the same park test (Test 19). As expected, the flange bottom (shown by the blue curve) experienced the largest strain (and stress as shown by averaged stress values given with each curve). The strains are smaller for locations higher in the cross-section of the steel tee section, as shown by the data from the strain gauges at mid-depth of the (exposed) web (green curve) and near the concrete deck (red curve).

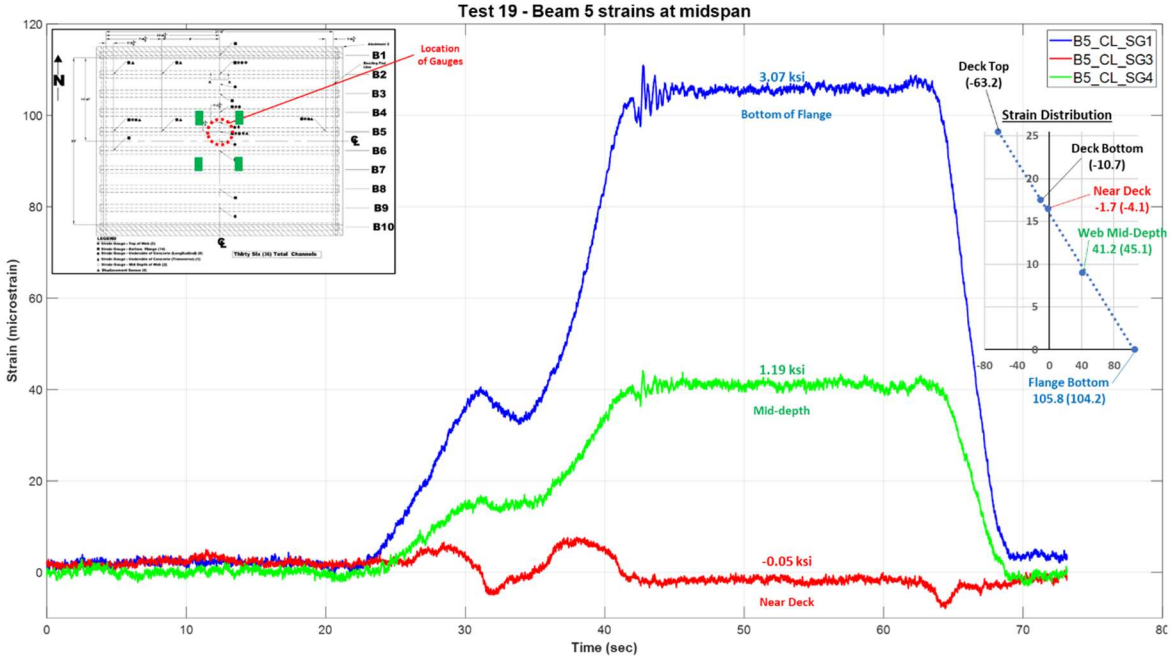

Figure 41. Park Test 19: Mid-span strain time-history responses over depth of composite steel tee section B5.

A plot of the strain distribution across the cross-section of composite steel tee section B5 is provided on the right side of Figure 41, where with location on the cross-section (from the bottom of the flange) is shown on the ordinate and the strain is shown on the abscissa. The dashed line is the best-fit straight line for the strain values from the three strain gauges on the steel tee section. These strain values are the average strain values (over a duration of 10 seconds) for the park test (Test 19). The strains at the bottom and top of the concrete deck (in parentheses) are from extrapolation of this best-fit line. The strain distribution plot compares the measured values from the strain gauges with the values from the best-fit line (in parentheses). The relatively small differences between the measured values and best-fit line (i.e., 3.9 microstrain corresponding to 0.11 ksi) validate the plane-section assumption.

As discussed in more detail in Chapter 4, two sources of restraint at the ends of the composite steel tee sections have been identified in the Flex Beam demonstration bridge: (1) negative (reverse) bending at the ends of the most heavily-loaded composite steel tee sections (near the bearings) from the torsional rigidity of the concrete end diaphragms, and (2) negative bending plus axial compression (i.e., "arching action") from restraint provided by the roadway subbase and backfill material at the semi-integral abutments. Although negative bending from the torsional rigidity of the end diaphragms is indistinguishable from negative bending caused by restraint from the roadway subbase and backfill material at the semi-integral abutments, compressive axial force on the cross-section at mid-span is a clear indicator of restraint from the roadway subbase and backfill material at the semi-integral abutments.

To determine if such axial force is present, the location of the centroid of the transformed-section model of the composite steel tee section (described in Chapter 4), 16.79 in. above the bottom of the steel tee flange, is compared to the location of the neutral axis (zero strain) interpolated using the best-fit line for the values from the three strain gauges on the steel tee section. For Test 19, the neutral axis at mid-span of B5 is 15.88 in. above the bottom of the flange, and compressive strain is observed at the centroid of the transformed-section model. The corresponding (compressive) stress at the centroid is -0.17 ksi, and the corresponding compressive axial force is -7.5 kips.

For the same park test (Test 19), negative (reverse) bending is observed at the ends (i.e., near the bearings) of composite steel tee section B5. Figure 42 and Figure 43 show the strains (with corresponding averaged stress values) through the depth of the composite steel tee section near the west and east bearings, respectively. From Figure 42, it is observed that the bottom of the flange (blue curve) near the west bearing is in compression, as a result of negative bending. The strains near the east bearing (Figure 43) are similar (blue curve for the bottom of the flange and green curve for mid-depth of the web).

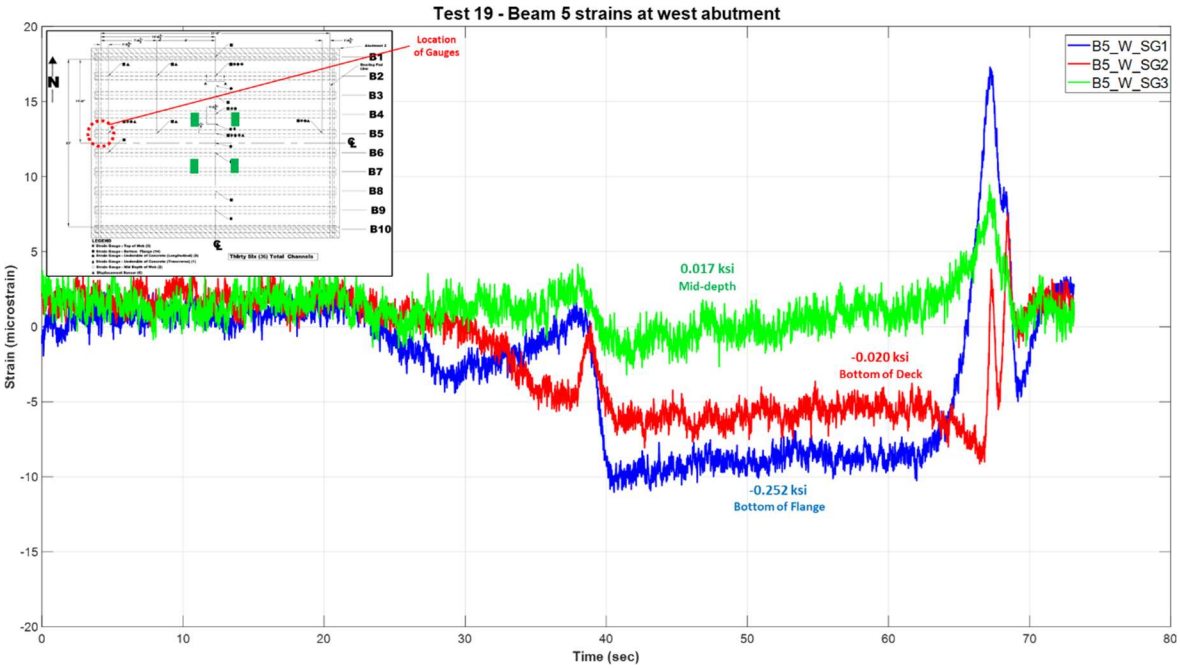

Figure 42. Park Test 19: Strain time-history responses over depth of composite steel tee section B5 near west bearing.

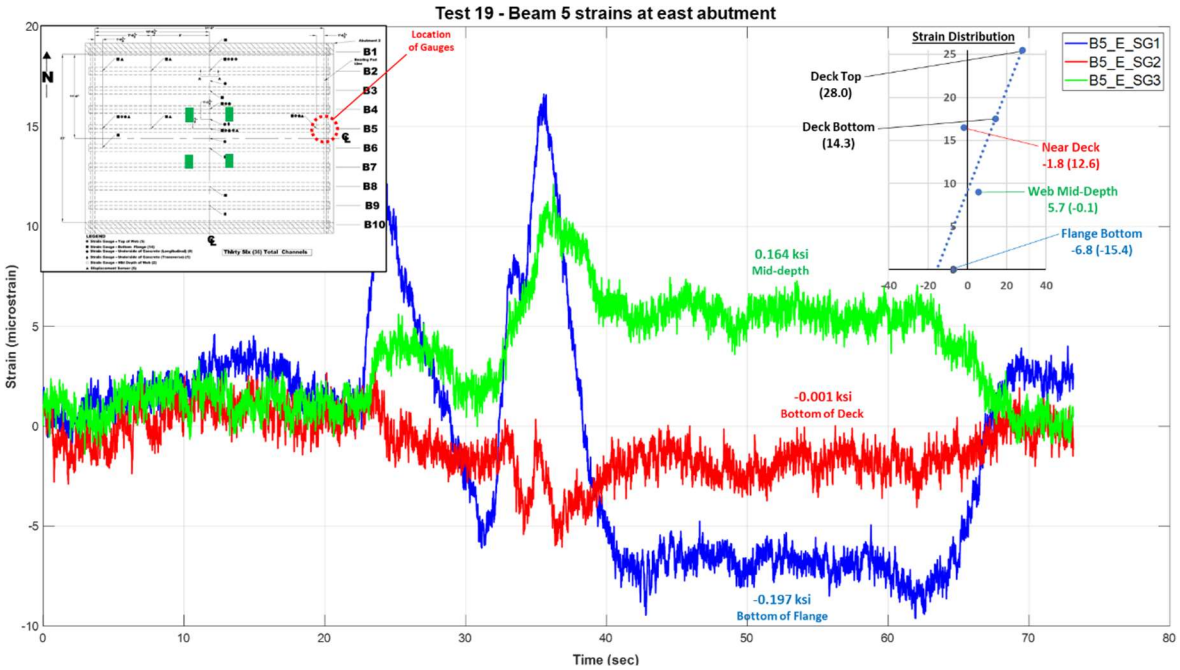

Figure 43. Park Test 19: Strain time-history responses over depth of composite steel tee section B5 near east bearing.

In both Figure 42 and Figure 43, the red curve is between the blue curve and green curve (flange bottom and mid-depth of web, respectively); the red curve is for the strain on the bottom of the concrete deck near the web of the steel tee section. From a plane-section assumption and assuming fully composite action, it is expected that the strain on the bottom of the deck would be positive (tension) and greater than the strain at mid-depth of the web. The results in Figure 42 and Figure 43, however, show that the plane-section assumption is not valid at these cross-sections near the bearings, likely as a result of interaction with the large concrete end diaphragms. A theoretical linear strain distribution across the cross-section of composite

steel tee section B5, which is consistent with the plane-section assumption, is shown as a dashed line in the plot on the right side of Figure 43. This dashed line is the best-fit straight line for the strain values from the three strain gauges on the steel tee section. These strain values are the average strain values (over a duration of 10 seconds) for the park test (Test 19). The strains at the bottom and top of the concrete deck (in parentheses) are from extrapolation of this best-fit line. The strain distribution plot compares the measured values from the strain gauges with the values from the best-fit line (in parentheses). The comparison shows very large differences, indicating that the measured strain values are not consistent with a linear strain distribution that is corresponds to the plane-section assumption. The influence of the large concrete end diaphragms on the strains and stresses in the composite steel tee sections near the bearings is discussed further in Chapter 4.

The relative displacement sensor data (showing the relative displacement between the web of the steel tee sections and concrete deck) are shown in Figure 44. The figure shows the relative displacement time-histories for the six displacement sensors (with averaged values given in mils where 1 mil = 0.001 in.) for the same park test (Test 19, Transverse Position 1, Longitudinal Position 3, westbound lane). The displacement sensor placed on composite steel tee section B5 near the west bearing, plotted in green has an averaged value of 0.20 mils, and the displacement sensor on B5 near the east bearing, plotted in grey has an averaged value of 0.23 mils. Data from laboratory tests have shown that these levels of relative displacement (i.e., 0.0002 to 0.0003 in.) correspond to linear-elastic interface shear force versus shear deformation behavior with essentially no slip (Cercone, Naito, Hendricks, & Sause, 2021). It is noteworthy that the displacement sensors at the mid-span and west quarter point of the span of B5 measure similar levels of relative displacement. In simple beam theory, when the test truck is in Longitudinal Position 3 with the tandem axle centered on mid-span, the quarter point is subjected to a level of interface shear force similar to that near the bearings, while the mid-span is not subjected to significant interface shear force. Thus, the small measured relative displacement at mid-span is from a modest level of asymmetry (about mid-span) in the bridge (e.g., fixed west bearings and expansion bearings at the east end). The displacement sensors on B2 show no measurable relative displacement, because interface shear force in B2 is very small.

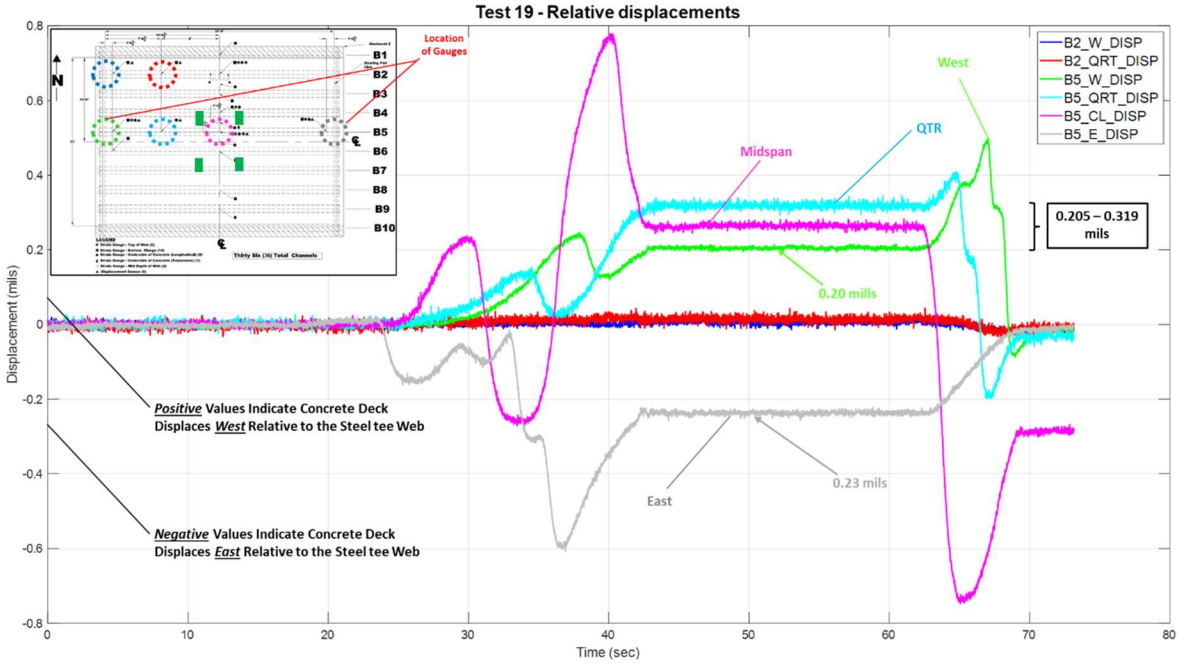

Figure 44. Park Test 19: Relative displacement time-history responses.

Figure 45 shows the strain time-histories measured during the same park test (Test 19) for four strain gauges on the bottom of the concrete deck. Three of these strain gauges measure longitudinal strain (DK_2_3_SG2, DK_4_5_SG2, and DK_5_6_SG2) and one strain gauge measures transverse strain (DK_4_5_SG5). All

longitudinal measurements show relatively small strain and corresponding averaged stress values (while the truck was parked). As the inset drawing in the top left corner of Figure 45 shows, the wheels on the north side of the truck are positioned between steel tee sections B4 and B5, which produces relatively high transverse flexural strain and stress on the concrete deck bottom when compared to the longitudinal strain and stress on the bottom of the deck from overall (primary) bending of the composite steel tee section. Although the static response from strain gauge DK_4_5_SG2 while the truck was parked is relatively small (-0.024 ksi), the local effects of the wheel loads cause larger values of strain and stress when the wheels passed over the strain gauge location. These larger values are not evident in the strains measured at strain gauges DK_2_3_SG2 and DK_5_6_SG2, because the wheels do not pass over these strain gauge locations.

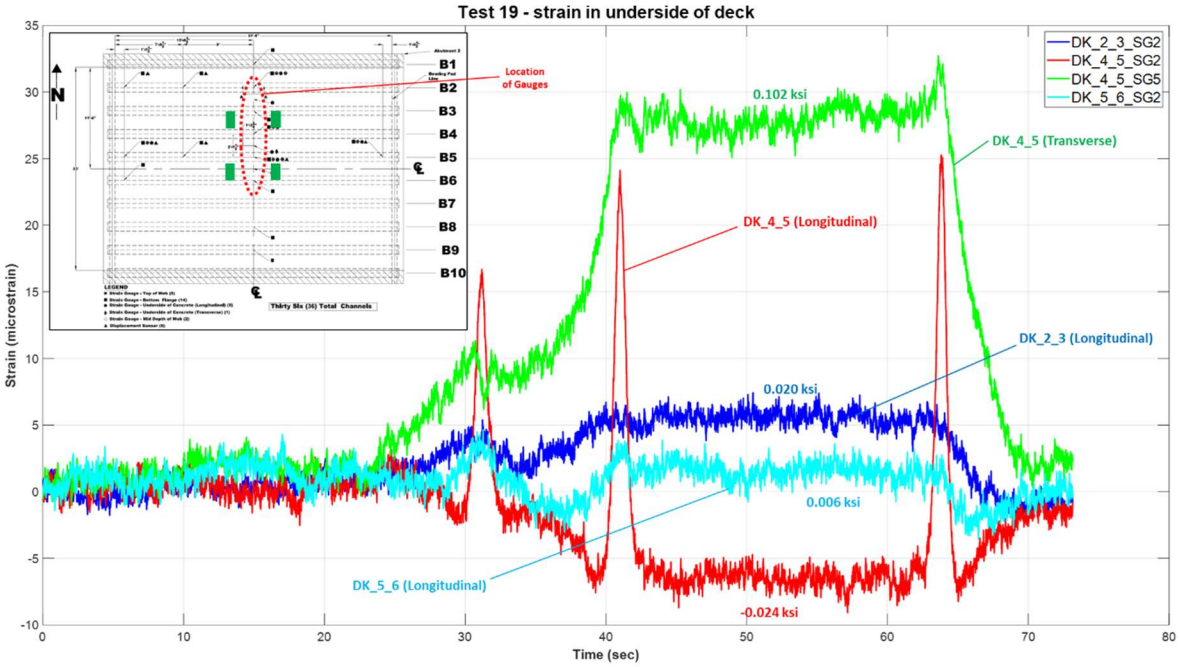

Figure 45. Park Test 19: Strain time-history responses on bottom of concrete deck.

3.2.1.2. Crawl Tests

Figure 46 shows strain time-histories for the flange bottom at mid-span of each instrumented composite steel tee section during Test 1 (crawl test in Transverse Position 1, mid-width of the bridge). As observed during the park tests, a local maxima in the strain data occurs as a truck axle passes above the sensor location. The peak response occurs as the rear tandem axle passes over mid-span. Figure 47 shows strain time-histories for the flange bottom of B2 and B5 at the west quarter point of the span, where the strain values are of smaller magnitude and a similar local maxima in the response is seen as the rear tandem axle passes over the strain gauge location. The figure shows B5 has larger strain than B2 because the test truck is mid-width of the bridge.

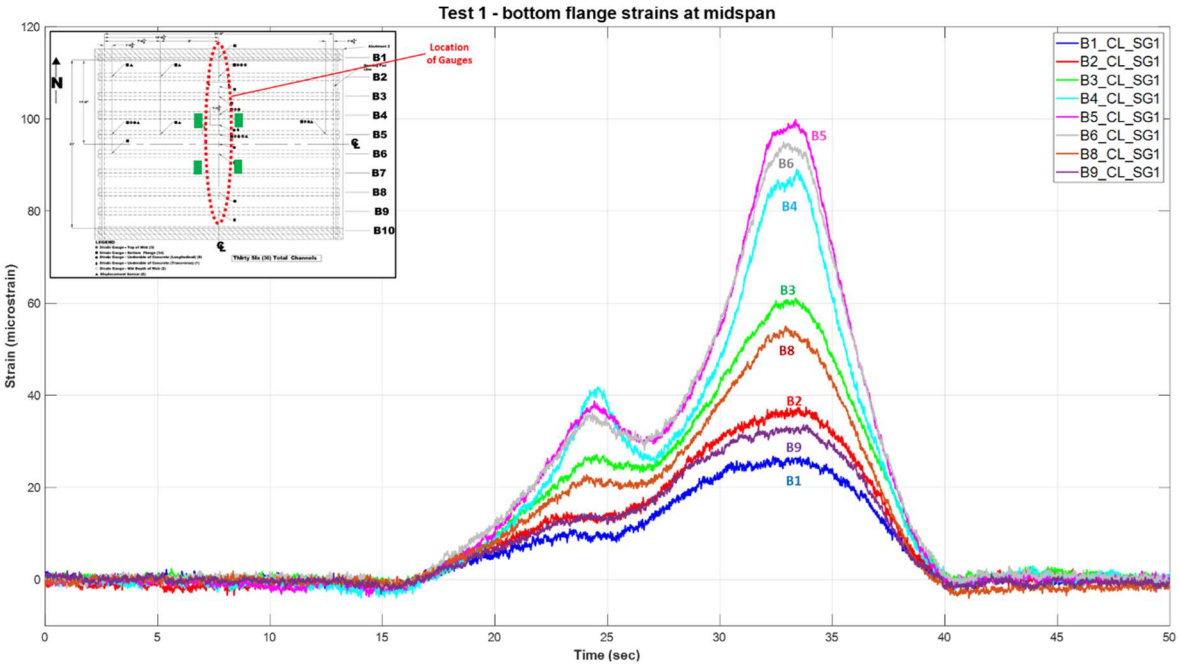

Figure 46. Crawl Test 1: Strain time-history responses on bottom of flanges at mid-span.

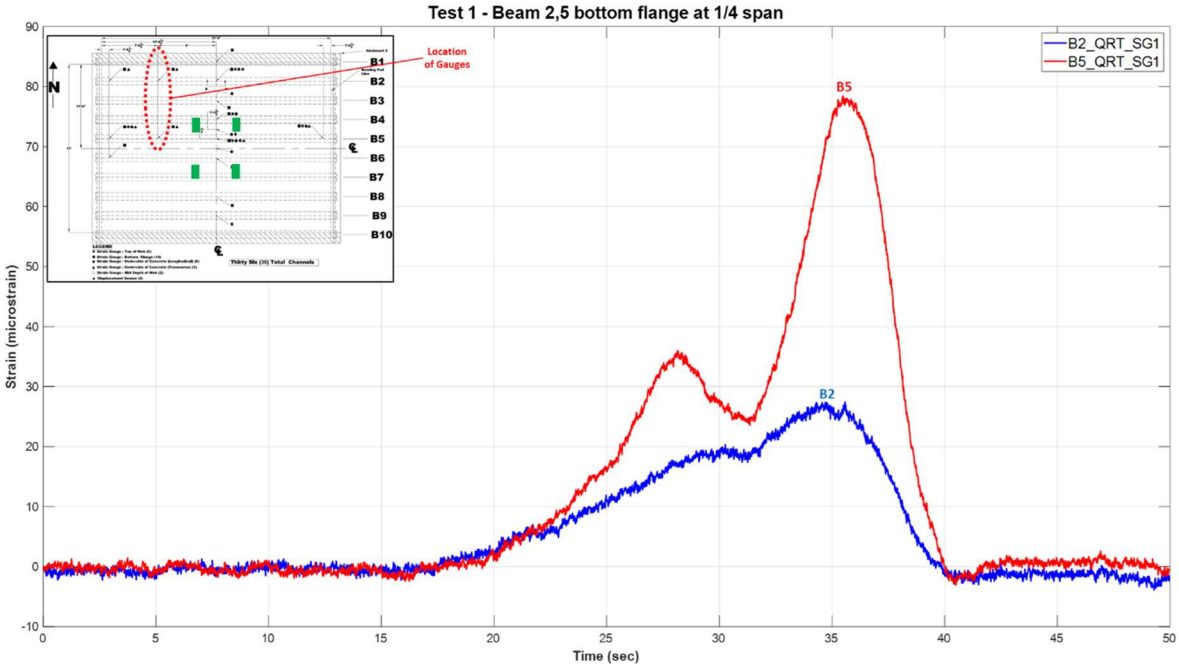

Figure 47. Crawl Test 1: Strain time-history responses on flanges at west quarter point of B2 and B5.

Figure 48 shows the responses of the mid-span strain gauges through the depth of composite steel tee section B5 during crawl Test 1. The figure shows that as the truck axles passed over the location of the gauges, the flange bottom and mid-depth of the web had positive strains and the web near the deck had negative strain. A plot of the strain distribution across the cross-section of composite steel tee section B5 (at a point in time with relatively large measured strain values, 34.0 seconds) is provided on the right side of Figure 48. The dashed line is the best-fit straight line for the strain values from the three strain gauges on the steel tee section. The strains on the bottom and top of the concrete deck (in parentheses) are determined from extrapolation of this best-fit line. The strain distribution plot compares the measured values from the strain

gauges with the values from the best-fit line (in parentheses). The relatively small differences between the measured values and best-fit line (i.e., 0.4 microstrain corresponding to 0.01 ksi) validate the plane-section assumption. For crawl Test 1, the neutral axis at mid-span of B5 is 15.53 in. above the bottom of the flange, and compressive strain is observed at the centroid of the transformed-section model. The corresponding (compressive) stress at the centroid is -0.23 ksi, and the corresponding net (compressive) axial force on the cross section is -10.1 kips.

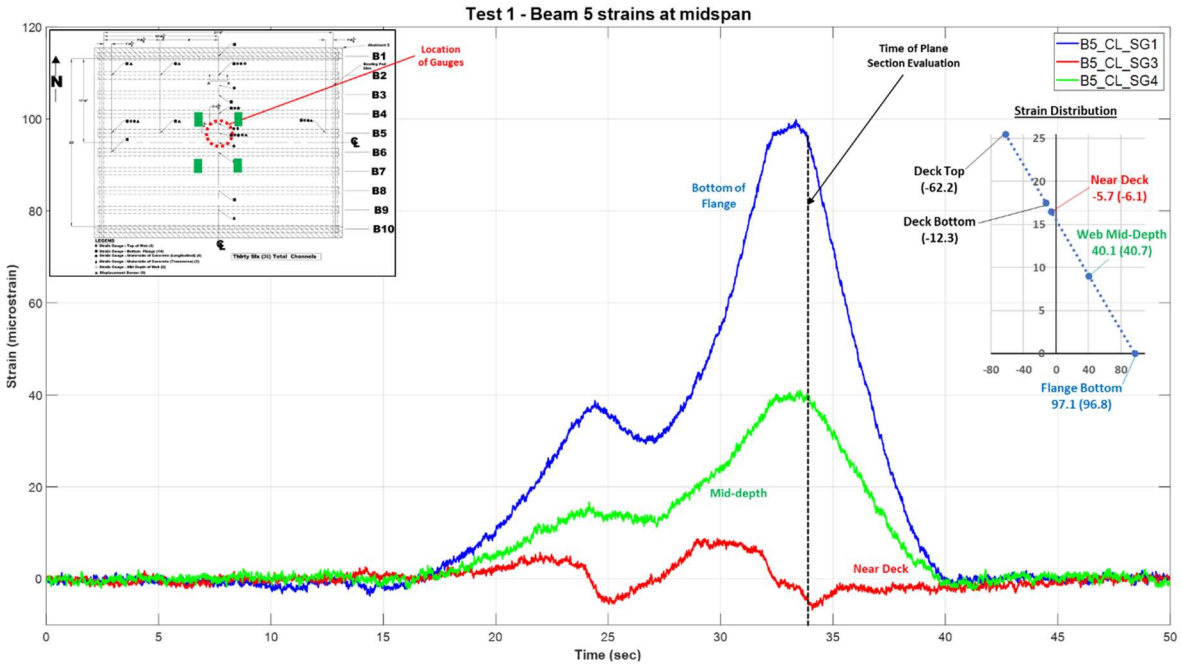

Figure 48. Crawl Test 1: Mid-span strain time-history responses over depth of composite steel tee section B5.

Figure 42 and Figure 43, which are plots of data from park Test 19 (Transverse Position 1, Longitudinal Position 3), show that negative (reverse) bending occurs at the ends (i.e., near the bearings) of composite steel tee section B5 when the tandem axle was near mid-span. Similar response is observed in Figure 49 and Figure 50 during crawl Test 1. Near the west bearing (Figure 49), the flange bottom (blue curve) has notable compression strain at approximately 32 to 33 seconds indicating notable negative bending as the tandem axle neared mid-span of the bridge. Later, as the tandem axle moved toward the west bearing, tension strains are observed on the flange bottom, followed by negative strains as the tandem axle passes over the strain gauge location. Note that the time of peak tension strains near the west bearing (at approximately 37 to 38 seconds) is after the time of peak tension strains on the flange bottom of B5 at the west quarter point of the span (at approximately 36 seconds, see Figure 47) since the test truck moved in the westbound direction. Near the east bearing (Figure 50), the flange bottom (blue curve) has notable compression strain at approximately 32 to 33 seconds indicating notable negative bending as the tandem axle neared mid-span of the bridge. Earlier, as the front axle passed over the east bearing (at approximately 15 seconds), compression strain occurs on the flange bottom as the front axle passes over the strain gauge location, followed by tension strain as the front axle moved into the span, followed by compression strain as the tandem axle passed over the east bearing, followed by tension strain as the tandem axle moved into the span.

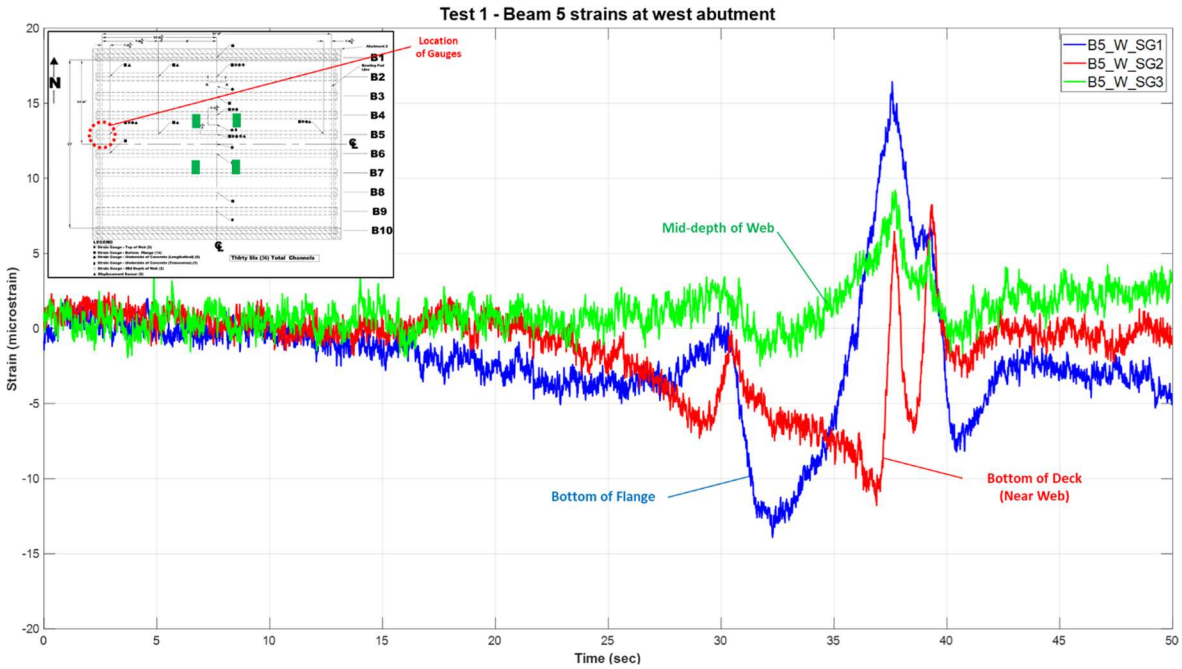

Figure 49. Crawl Test 1: Strain time-history responses over depth of composite steel tee section B5 near west bearing.

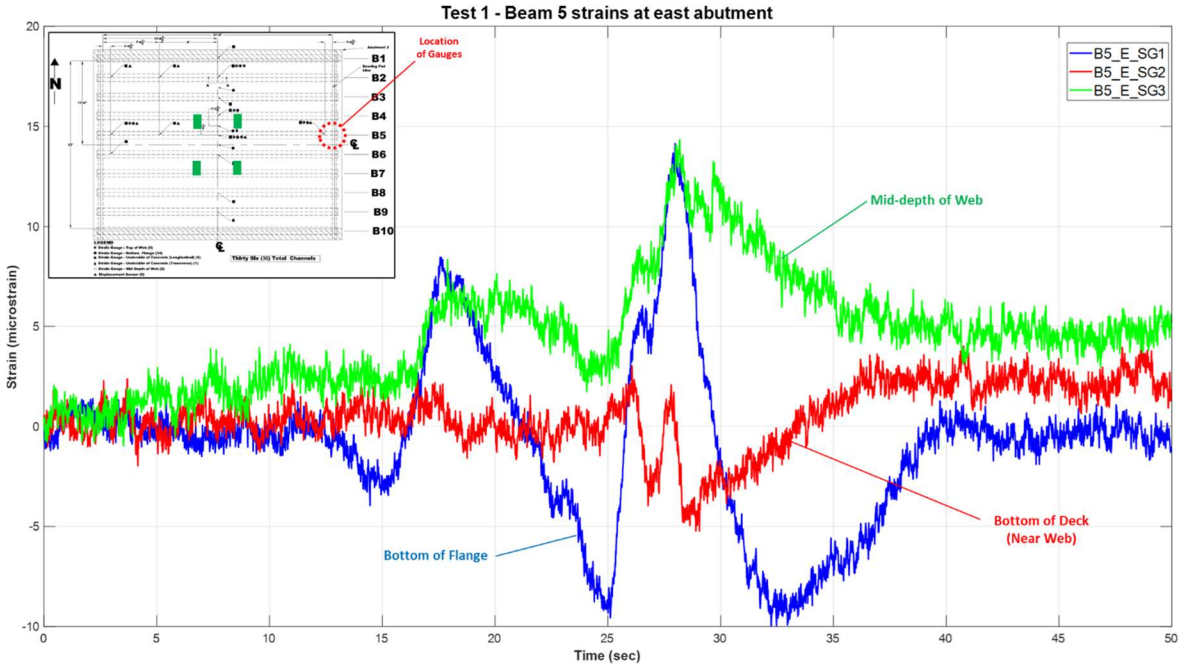

Figure 50. Crawl Test 1: Strain time-history responses over depth of composite steel tee section B5 near east bearing.

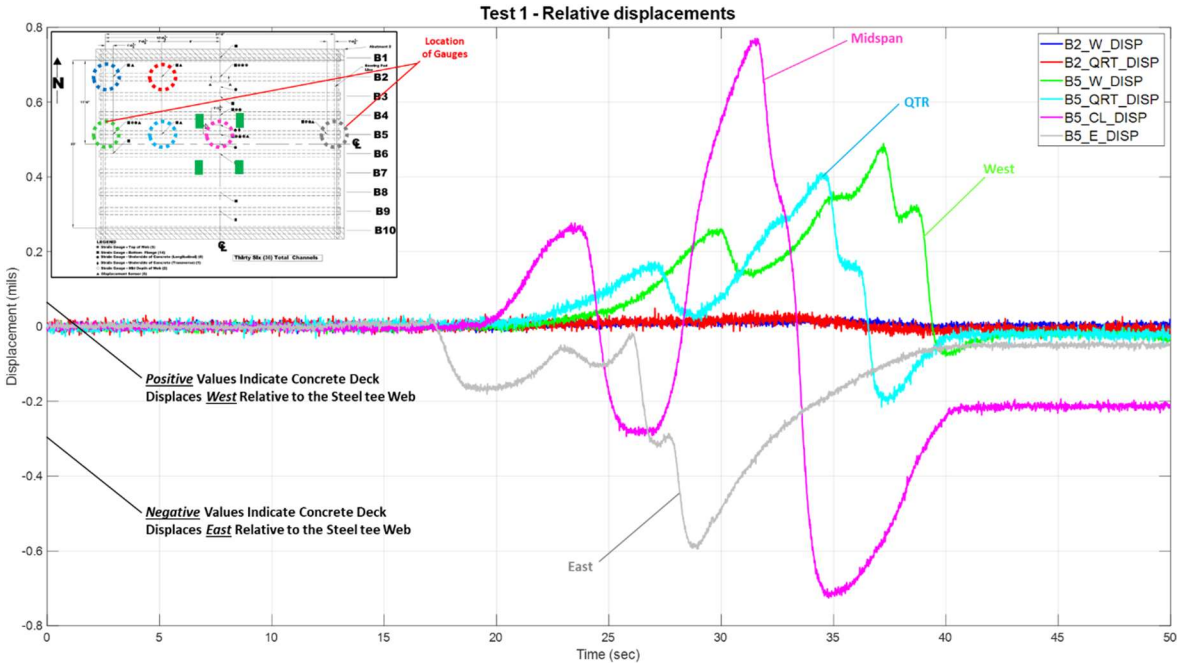

Figure 51. Crawl Test 1: Relative displacement time-history responses.

The displacement sensor data is shown in Figure 51. Although small in magnitude (less than 0.80 mils or less than 0.0008 in.) the largest relative displacement occurs at mid-span of composite steel tee section B5 (pink curve). This data shows that when the front axle approached mid-span (from the east), the deck is pushed westward relative to the web by the interface shear force (i.e., by the shear flow), and after the front axle passed mid-span (at approximately 24 to 25 seconds) the deck is pushed eastward relative to the web. A similar response occurs as the tandem axle approached mid-span and then passed mid-span (before and then after approximately 33 to 34 seconds). The magnitude of the relative displacement from the tandem axle is much larger than from the front axle because of the much larger tandem axle load. Similar, but more complex relative displacement responses are observed from the other displacement sensors on B5. The displacement data at the west quarter point of B5, for example, shows that as the front axle approached the quarter point, the deck is pushed westward relative to the web and as the front axle then passed the quarter point at approximately 27 to 28 seconds, the westward relative displacement of the deck decreased, but the deck relative displacement did not fully reverse (in sign) and the deck was not displaced to the east (relative to the web) because the much larger tandem axle load came on to the bridge at approximately 25 to 26 seconds, so the total interface shear continued to push the deck to the west (relative to the web). Data from laboratory tests shown in (Cercone, Naito, Hendricks, & Sause, 2021) show that these levels of relative displacement (i.e., less than 0.0008 in.) correspond to linear-elastic interface shear force versus shear deformation behavior with essentially no slip. The displacement sensors on B2 show no measurable relative displacement, because the level of interface shear force in B2 is very small.

Figure 52 shows the strain time-histories measured by strain gauges on the bottom of the concrete deck. Strain gauges located directly underneath the truck wheel path (between B4 and B5) measured a large local response (large local maxima) as the wheel passed over the strain gauge. This strain response is measured by a strain gauge located away from the truck wheel path (between B2 and B3) did not have a large local maxima, which is particularly noticeable when comparing the strain from DK_4_5_SG2 (red curve) to that from DK_2_3_SG2 (blue curve). The time history from strain gauge DK_4_5_SG5, which measured transverse strain, shows the effects of positive (transverse) bending between steel tee sections B4 and B5.

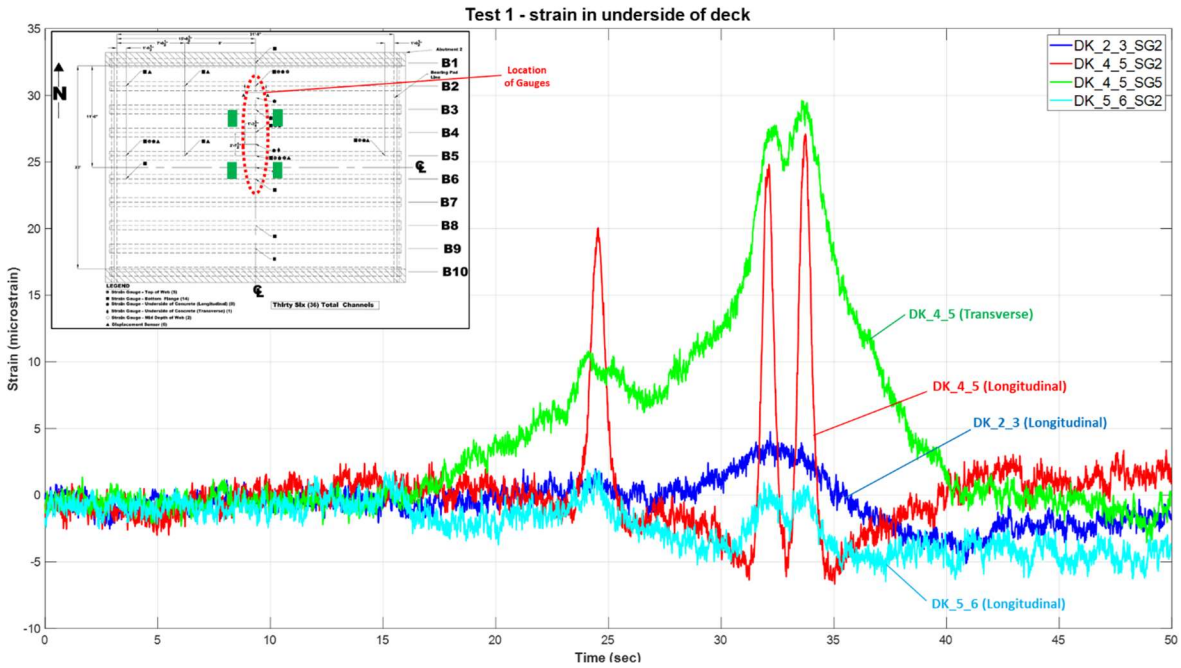

Figure 52. Crawl Test 7: Strain time-history responses on bottom of concrete deck.

3.2.1.3. Dynamic Tests

Figure 53 shows the strain time-histories for the flange bottom at mid-span of each instrumented composite steel tee section during Test 7 (dynamic test in Transverse Position 1, mid-width of the bridge). The strain responses are consistent with those observed for the corresponding crawl test (i.e., Test 1). The levels of dynamic amplification of dynamic test results versus crawl test results are discussed later.

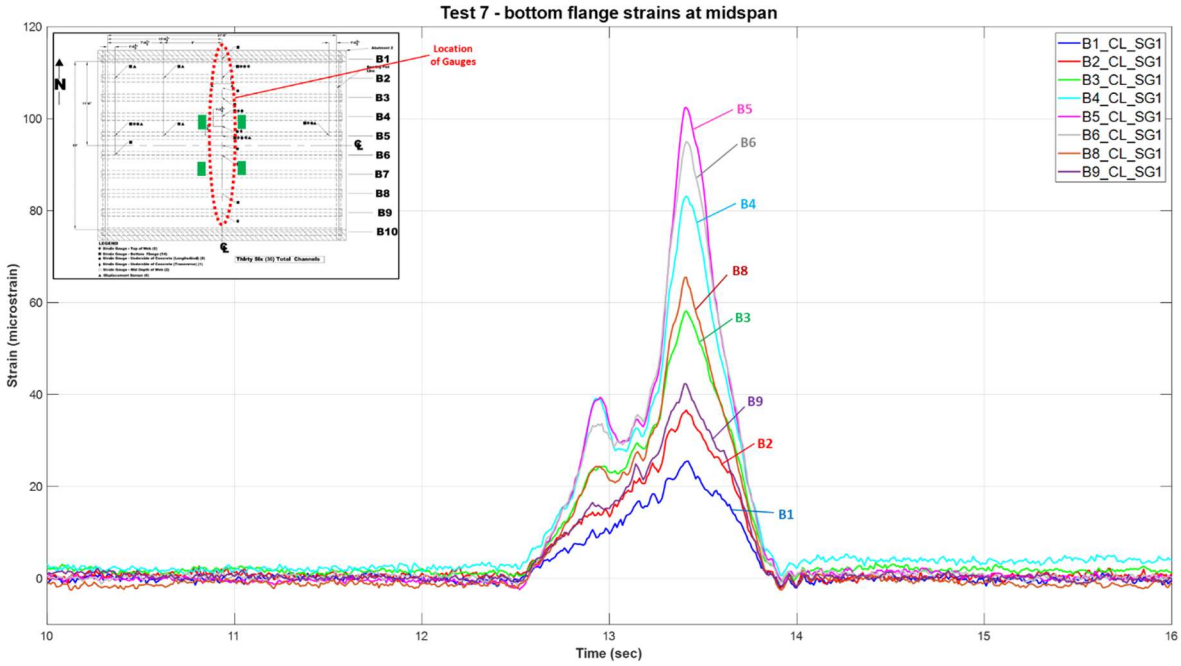

Figure 53. Dynamic Test 7: Strain time-history responses on bottom of flanges at mid-span.

Figure 54 shows the responses of the mid-span strain gauges through the depth of composite steel tee section B5 during dynamic Test 7. A plot of the strain distribution across the cross-section of composite steel tee

section B5 (at an approximate 13.5 second mark) is shown on the right side of Figure 54. The dashed line is the best-fit straight line for the strain values from the three strain gauges on the steel tee section. The relatively small differences between the measured values and best-fit line (i.e., 0.4 microstrain corresponding to 0.01 ksi) validate the plane-section assumption. For dynamic Test 7, the neutral axis at mid-span of B5 is 15.15 in. above the bottom of the flange, and compressive strain is observed at the centroid of the transformed-section model. The corresponding (compressive) stress at the centroid is -0.29 ksi, and the corresponding compressive axial force is -12.7 kips.

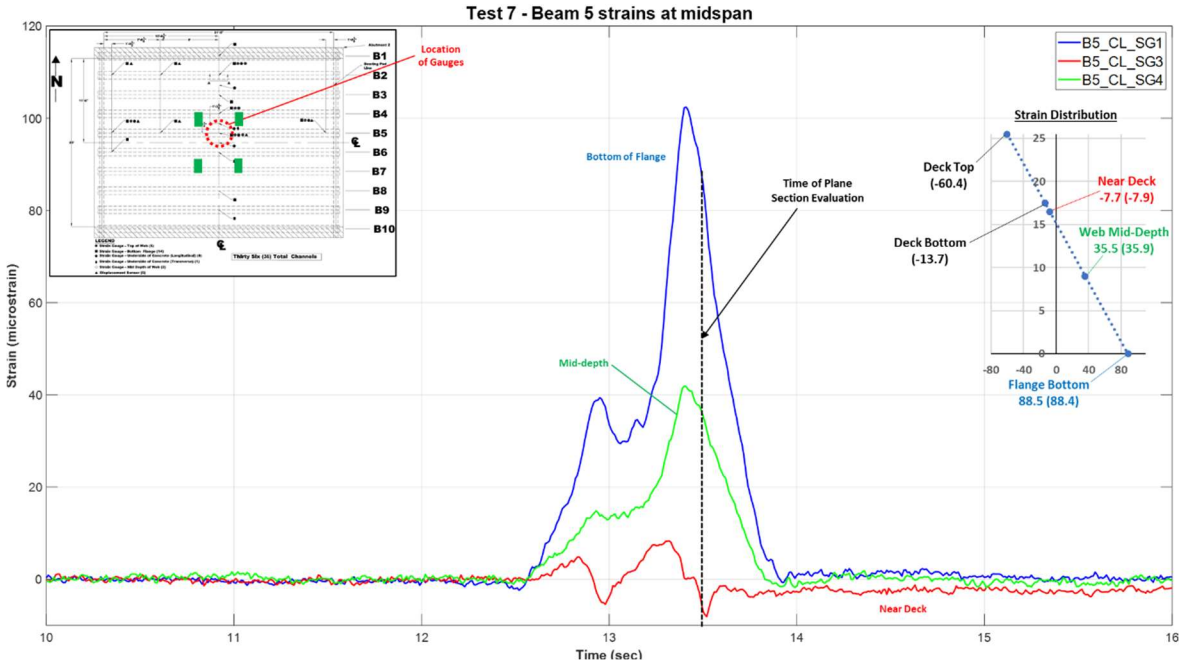

Figure 54. Dynamic Test 7: Mid-span strain time-history responses over depth of composite steel tee section B5.

Figure 52 shows the strain time-histories measured by strain gauges on the bottom of the concrete deck. Strain gauges located directly underneath the truck wheel path (between B4 and B5) measured a large local response (large local maxima) as the wheel passed over the strain gauge. This strain response is measured by a strain gauge located away from the truck wheel path (between B2 and B3) did not have a large local maxima, which is particularly noticeable when comparing the strain from DK_4_5_SG2 (red curve) to that from DK_2_3_SG2 (blue curve). The time history from strain gauge DK_4_5_SG5, which measured transverse strain, shows the effects of positive (transverse) bending between steel tee sections B4 and B5.

Figure 55 shows the strain time-histories measured by strain gauges on the bottom of the concrete deck. The strain response measured by DK_4_5_SG2 (red curve) shows large local maxima as the truck wheels passed over the strain gauge. The transverse strain measured by strain gauge DK_4_5_SG5 shows the effects of positive (transverse) bending between steel tee sections B4 and B5 as the wheel loads passed between these steel tee sections.

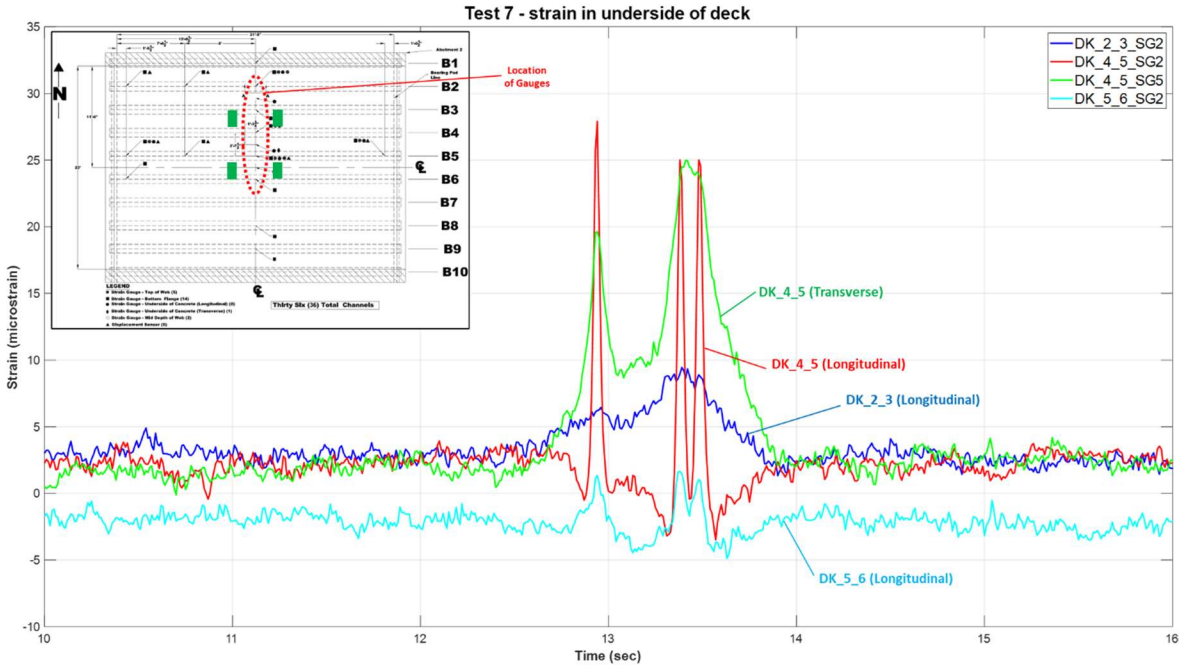

Figure 55. Dynamic Test 7: Strain time-history responses on bottom of concrete deck.

In general, the measured responses of the bridge during the dynamic tests are consistent with the measured responses during the park and crawl tests. The roadway on the Flex Beam demonstration bridge and on its approaches were observed to be relatively smooth, so dynamic amplifications of responses during the dynamic tests relative to those from the crawl tests were not expected to be large. Table 4 provides a dynamic amplification factor (DAF) of the response for each sensor from tests with the test truck mid-width of the bridge (Transverse Position 1). The DAF was calculated as the ratio of the result from the dynamic tests over the result from the crawl tests. Since two dynamic tests in each transverse position and two dynamic tests in each transverse position were conducted, the results from the two tests were averaged before the DAF was calculated. The DAF in Table 4 is the ratio of the averaged results dynamic tests 7 and 8 over the averaged results for crawl tests 1 and 2.

Typical DAF values are less than 1.0 and almost all DAF values are less than 1.2. Two DAF values from sensors near the bearings are unusually large (shown in bold font in the table), although the actual response values (from either the dynamic tests or the crawl tests) are small. Among the DAF values associated with significant strain (or stress), such as the flange bottom at mid-span of the instrumented composite steel tee sections near the mid-width of the bridge (i.e., B3, B4, B5, B6, and B8, shown in bold font in the table), the largest DAF is 1.09 for B8 and the remaining DAF are less than 0.96.

Table 4. DAF from dynamic tests and crawl tests.

Channel Name	Test 1		Test 2		Avg 1 & 2		Test 7		Test 8		Avg 7 & 8		DAF	
	Max Neg	Max Pos	Max Neg	Max Pos	Max Neg	Max Pos	Max Neg	Max Pos	Max Neg	Max Pos	Max Neg	Max Pos	Max Neg	Max Pos
B2_W_SG1	-0.085	0.220	-0.058	0.254	-0.071	0.237	-0.097	0.168	-0.071	0.189	-0.084	0.178	1.173	0.751
B2_QRT_SG1	-0.114	0.795	-0.118	0.857	-0.116	0.826	-0.106	0.628	-0.073	0.721	-0.089	0.675	0.770	0.817
B1_CL_SG1	-0.086	0.776	-0.123	0.769	-0.105	0.772	-0.065	0.74	-0.077	0.703	-0.071	0.722	0.679	0.934
B2_CL_SG1	-0.098	1.086	-0.097	1.113	-0.097	1.099	-0.067	1.062	-0.086	1.01	-0.076	1.036	0.785	0.942
B2_CL_SG2	-0.005	0.046	-0.011	0.036	-0.008	0.041	-0.004	0.045	-0.007	0.042	-0.006	0.043	0.680	1.044
B2_CL_SG3	-0.081	0.270	-0.084	0.247	-0.083	0.259	-0.093	0.174	-0.045	0.196	-0.069	0.185	0.835	0.715
B2_CL_SG4	-0.086	0.568	-0.047	0.613	-0.066	0.591	-0.026	0.628	-0.069	0.524	-0.048	0.576	0.719	0.975
DK_2_3_SG2	-0.019	0.017	-0.005	0.031	-0.012	0.024	-0.002	0.034	-0.016	0.016	-0.009	0.025	0.757	1.037
B3_CL_SG1	-0.071	1.771	-0.074	1.828	-0.073	1.800	-0.024	1.686	-0.064	1.558	-0.044	1.622	0.600	0.901
B4_CL_SG1	-0.116	2.582	-0.056	2.616	-0.086	2.599	-0.001	2.41	-0.073	2.227	-0.037	2.318	0.431	0.892
B4_CL_SG2	-0.011	0.073	-0.012	0.064	-0.012	0.069	-0.01	0.047	-0.016	0.046	-0.013	0.046	1.117	0.675
B4_CL_SG3	-0.109	0.356	-0.091	0.319	-0.100	0.337	-0.067	0.283	-0.075	0.269	-0.071	0.276	0.711	0.819
B5_QRT_SG1	-0.090	2.275	-0.191	2.239	-0.141	2.257	-0.133	2.014	-0.119	2.17	-0.126	2.092	0.897	0.927
B5_W_SG1	-0.403	0.477	-0.320	0.507	-0.362	0.492	-0.468	0.382	-0.336	0.372	-0.402	0.377	1.111	0.767
B5_W_SG2	-0.043	0.030	-0.034	0.034	-0.038	0.032	-0.049	0.042	-0.044	0.035	-0.047	0.038	1.221	1.191
B5_W_SG3	-0.073	0.267	-0.077	0.314	-0.075	0.291	-0.202	0.11	-0.115	0.116	-0.159	0.113	2.122	0.390
DK_4_5_SG2	-0.024	0.098	-0.017	0.11	-0.021	0.104	-0.013	0.101	-0.023	0.083	-0.018	0.092	0.850	0.887
DK_4_5_SG5	-0.013	0.107	-0.013	0.112	-0.013	0.110	-0.003	0.091	-0.006	0.082	-0.005	0.086	0.373	0.785
B5_CL_SG1	-0.108	2.895	-0.035	2.94	-0.071	2.918	-0.07	2.97	-0.043	2.585	-0.057	2.778	0.794	0.952
B5_CL_SG3	-0.195	0.254	-0.234	0.241	-0.214	0.248	-0.235	0.241	-0.204	0.242	-0.220	0.241	1.025	0.976
B5_CL_SG4	-0.069	1.192	-0.087	1.189	-0.078	1.191	-0.071	1.215	-0.05	1.037	-0.061	1.126	0.782	0.946
B6_W_SG1	-0.439	0.440	-0.357	0.496	-0.398	0.468	-0.431	0.39	-0.384	0.388	-0.408	0.389	1.024	0.831
DK_5_6_SG2	-0.024	0.007	-0.018	0.013	-0.021	0.010	-0.018	0.007	-0.007	0.015	-0.012	0.011	0.604	1.104
B5_E_SG1	-0.291	0.410	-0.310	0.416	-0.300	0.413	-0.257	0.466	-0.271	0.329	-0.264	0.398	0.879	0.963
B5_E_SG2	-0.019	0.015	-0.024	0.009	-0.021	0.012	-0.01	0.016	-0.015	0.011	-0.012	0.014	0.578	1.140
B5_E_SG3	-0.028	0.416	-0.139	0.263	-0.083	0.339	-0.112	0.282	-0.074	0.286	-0.093	0.284	1.118	0.837
B6_CL_SG1	-0.068	2.755	-0.143	2.691	-0.106	2.723	-0.046	2.756	-0.038	2.455	-0.042	2.606	0.398	0.957
B8_CL_SG1	-0.118	1.595	-0.066	1.593	-0.092	1.594	-0.074	1.9	-0.07	1.567	-0.072	1.734	0.784	1.087
B9_CL_SG1	-0.090	0.975	-0.104	0.991	-0.097	0.983	-0.05	1.229	-0.104	0.987	-0.077	1.108	0.795	1.127
B2_W_DISP	-0.019	0.026	-0.015	0.035	-0.017	0.030	-0.033	0.021	-0.024	0.019	-0.028	0.020	1.649	0.647
B2_QRT_DISP	-0.032	0.049	-0.033	0.06	-0.033	0.055	-0.037	0.035	-0.028	0.037	-0.033	0.036	0.998	0.658
B5_W_DISP	-0.080	0.490	-0.105	0.472	-0.092	0.481	-0.101	0.5	-0.084	0.463	-0.092	0.481	1.002	1.001
B5_QRT_DISP	-0.216	0.411	-0.228	0.387	-0.222	0.399	-0.257	0.347	-0.237	0.356	-0.247	0.352	1.115	0.881
B5_CL_DISP	-0.726	0.770	-0.749	0.753	-0.738	0.762	-0.703	0.784	-0.758	0.734	-0.730	0.759	0.990	0.996
B5_E_DISP	-0.022	0.595	-0.028	0.581	-0.025	0.588	-0.097	0.486	-0.018	0.502	-0.024	0.494	0.944	0.841

"E": East
"W": West
"CL": Centerline of Span
"QTR": Quarter Point of Span

"B#": Beam Designation
"SG": Strain Gauge
"DISP": Displacement Sensor
"DK": Deck

3.2.2. Controlled-Load Testing Summary

The structural responses of the Flex Beam demonstration bridge were examined using controlled-load testing. This section presented and discussed measured data from crawl, dynamic, and park tests with the test truck in the same transverse position (Transverse Position 1, mid-width of the bridge). In general, the values of strain (or stress) and relative displacement measured in these various tests are relatively small in magnitude. This aspect of the test results will be discussed in Chapter 4.

Effects of the large concrete end diaphragms on the response of the bridge were observed. The Flex Beam bridge system is assumed to be a simply supported structure (i.e., assumed to respond as a simply-supported beam) for design purposes, so significant negative (reverse) bending near the bearings is not expected. However, some negative bending moments near the bearings are observed when vehicular loads are near mid-span. These negative bending moments are attributed to restraint of the end rotation of the composite steel tee sections by the concrete end diaphragms. This aspect of the test results and comparisons with finite element analysis (FEA) results will be presented and discussed in Chapter 4.

Test results for strains across the depth of the most heavily-loaded composite steel tee sections (i.e., those near the transverse position of the test truck), validated the use of the plane-section assumption from beam theory and a transformed-section model for analysis and design of Flex Beam units. The plane-section assumption was validated by strain measurements from all three types (i.e., crawl, dynamic, and park) of controlled-load tests.

Test results for relative longitudinal displacement between the web of the steel tee sections and the concrete deck was presented and discussed. The possibility of relative slip between the steel tee web and concrete deck was assessed. Data from laboratory tests shown in (Cercone, Naito, Hendricks, & Sause, 2021) show that the largest levels of relative displacement observed in the controlled-load testing of the Flex Beam bridge (i.e., less than 0.0008 in.) correspond to low-level linear-elastic interface shear force versus shear deformation behavior with essentially no slip. The interface shear connection performed as expected and full composite action was observed.

Test results for tensile stresses on the bottom of the concrete deck during the controlled-load testing were generally small in magnitude. The largest measured tensile stress on the bottom of the concrete deck during a park test was approximately 200 psi in the longitudinal direction near steel tee section B2 (strain gauge B2_CL_SG2) during Test 20 (Transverse Position 2, Longitudinal Position 3). For the crawl tests and dynamic tests, the largest measured tensile stress on the bottom of the concrete deck was approximately 500 psi in the longitudinal direction from strain gauge B2_CL_SG2 when the test truck was in Transverse Position 3 (where the largest average result from Test 5 and Test 6 was 490 psi). For the other locations with strain gauges on the bottom of the concrete deck, the largest measured tensile stresses were less than 200 psi and far below the theoretical concrete cracking stress for the concrete deck, taken as 500 psi. The largest tensile stresses were usually associated with localized maxima in the strain time-histories as the test truck wheels passed the location of the strain gauge.

Within the test data presented here, potential inaccuracies may be anticipated. Potential sources of inaccuracy include discrepancies in the transverse position of the test truck as it moved longitudinally during the crawl and dynamic tests, and shifting of the contents (i.e., soil) within the PennDOT dump truck which served as the test truck. Discrepancies in transverse position would affect the load carried by each individual composite steel tee section and shifting of the truck contents would affect the distribution of the truck weight among the axles and the wheels of each axle (i.e., the wheel and axle loads would differ from those measured before the controlled-load testing began). These potential sources of inaccuracy were not investigated, however, agreement observed between analysis results and test results suggest that such inaccuracies are small.

Summaries of the controlled-load testing data (average stresses and relative displacements for the park tests and maximum and minimum stresses and relative displacements for the crawl and dynamic tests) are

provided in Appendix A. Also presented in Appendix A are the dynamic amplification factor (DAF) values calculated from the dynamic test and crawl test results.

3.3. Monitoring of Typical Vehicular-Load Response

Monitoring of the Flex Beam demonstration bridge was conducted between Tuesday, October 25 and Thursday, December 08, 2022. During this time (i.e., the monitoring phase), triggered time-history data was collected from the strain gauges selected for monitoring.

3.3.1. Triggered Stress Time-History Data

As previously mentioned, two trigger conditions were used to initiate recording of data from the sensors (strain gauges) selected for the monitoring phase of the project. For traffic in the westbound (WB) lane, the gauge on the flange bottom of steel tee section B3 was used to trigger recording, while for traffic in the eastbound (EB) lane, the gauge on the flange bottom of steel tee section B8 was used to trigger recording. The data recorded after a trigger from the gauge on B3 was stored in one data file and the data recorded after a trigger from the gauge on B8 was stored in another data file. The trigger value was set to 0.25 ksi, so when the strain measured by either strain gauge (on B3 or B8) exceeded the strain value corresponding to 0.25 ksi (i.e., (0.25 ksi)/E = 8.62 microstrain), data from all strain gauges was recorded. It is worth noting that although the B3 strain gauge trigger was intended for traffic in the WB lane, and the B8 strain gauge trigger was intended for traffic in the EB lane, a single vehicle may create a trigger condition (stress greater than or equal to 0.25 ksi) for both the gauge on B3 and the gauge on B8, or for only one of the gauges. Study of the data in the two data files (one for the B2 trigger events and one for the B8 trigger events) showed that many vehicles created trigger conditions for both strain gauges, resulting in recorded data in both data files.

Figure 56 shows the complete time-histories of data from the flange bottom strain gauges at mid-span of steel tee sections B1, B2, B3, B4, B5, B6, B8, and B9 after a trigger from the strain gauge on B3. Figure 57 shows the complete time-histories of data from the flange bottom strain gauges at mid-span of steel tee sections B1, B2, B3, B4, B5, B6, B8, and B9 after a trigger from the strain gauge on B8. Note that the time-histories in Figure 56 and Figure 57 are not continuous histories of data. Each trigger event is relatively short and varies in duration depending on the speed of the vehicle, with data recording beginning 1 second before the strain exceeds the trigger level and concluding 1 second after the strain drops below the trigger level. Most events produced slightly more than 3 seconds of recorded data. In Figure 56 and Figure 57, the recorded data from the trigger events are shown consecutively, one after the other, from the beginning of the monitoring phase until the end. Specific trigger events of interest (those which produce high strains and stresses) are detected from the complete time-histories visually by zooming in on times of large strains in the complete histories, plotting an isolated event, and noting the time and trigger number assigned to the trigger event. The plots of monitoring data given in subsequent figures in this section show the date and time at which the particular event occurred and show only the time-history of data for the individual event (i.e., with time equal to zero at the beginning of the data time-histories for the event).

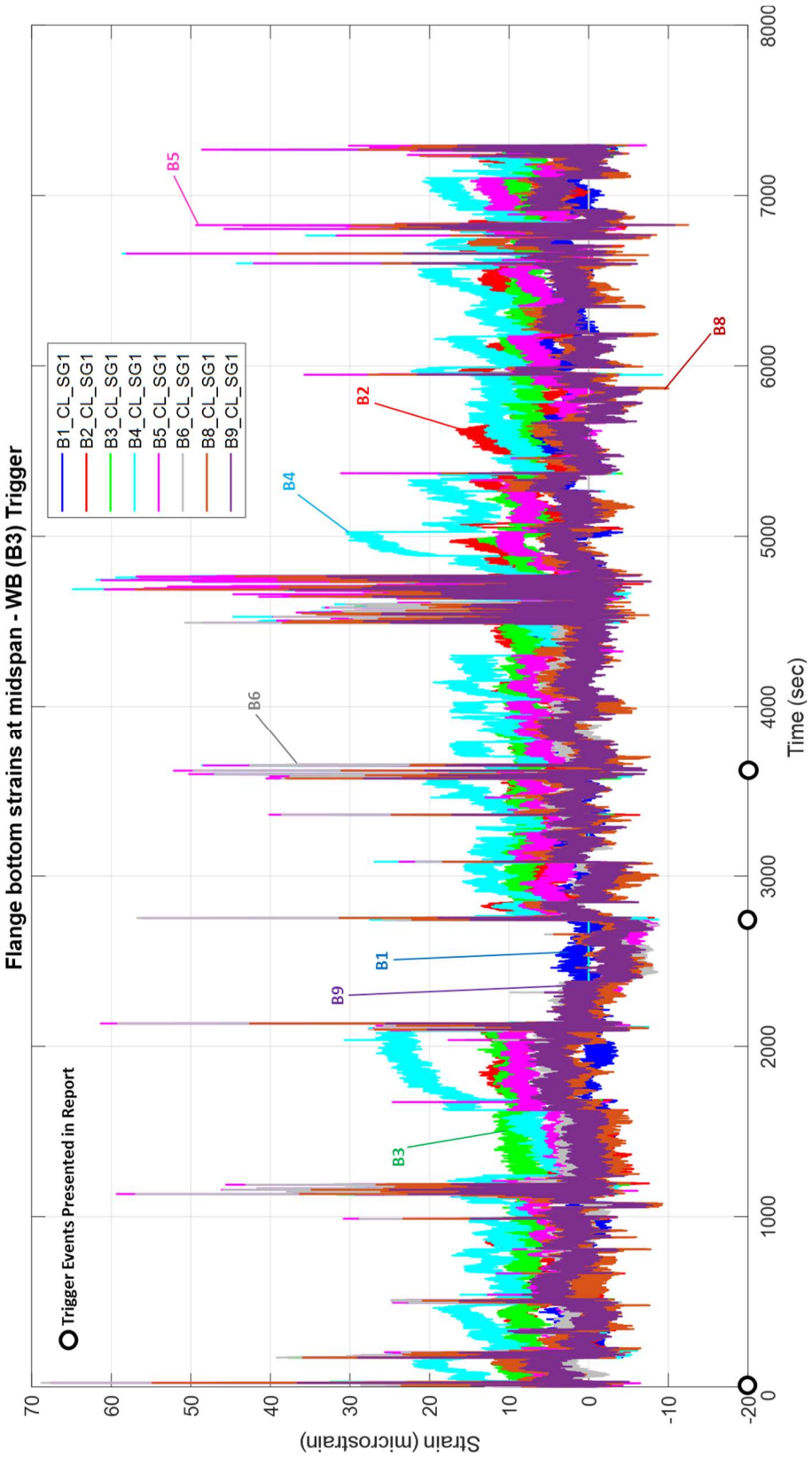

Figure 56. Complete time-histories of mid-span flange bottom strain data from B3 trigger events.

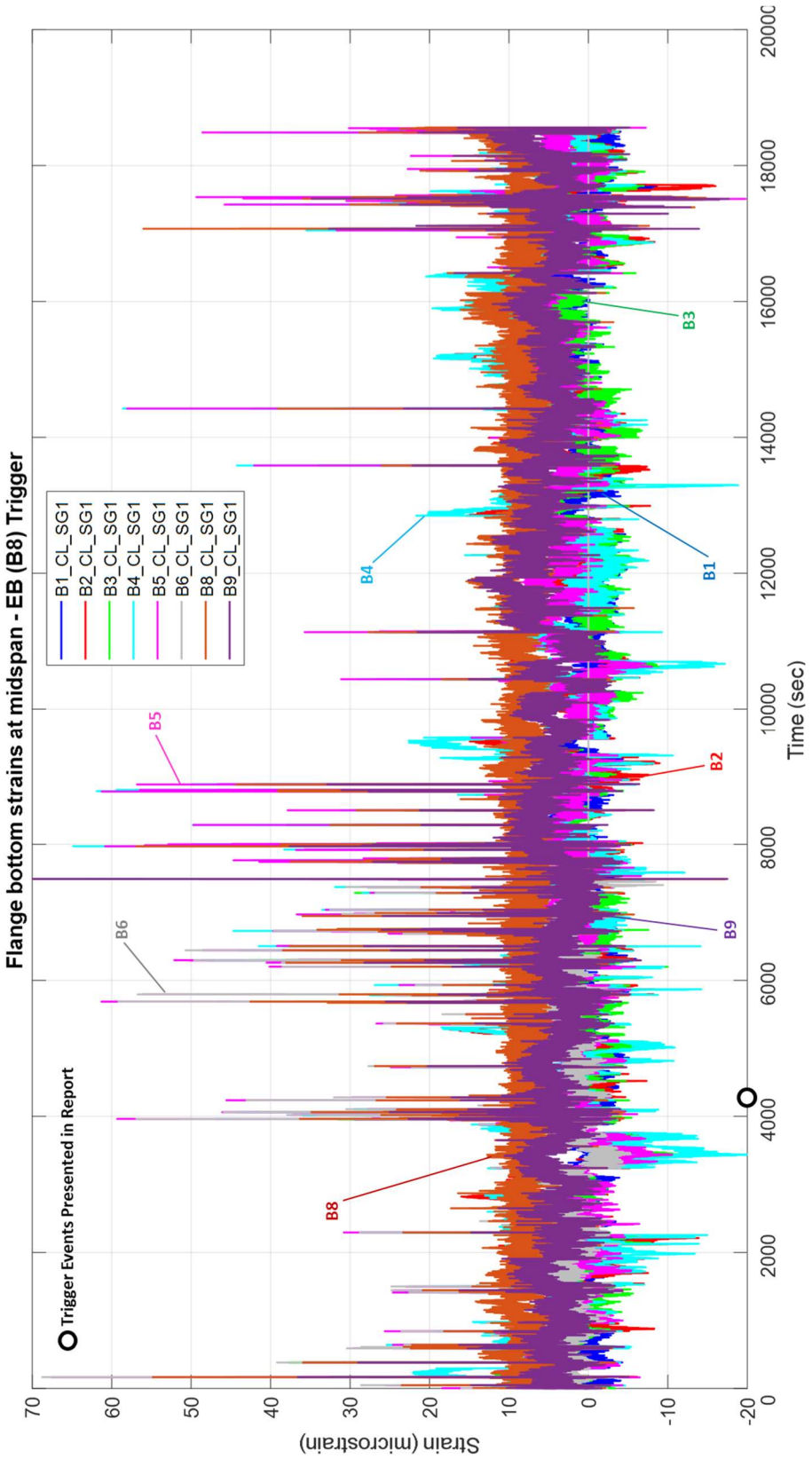

Figure 57. Complete time-histories of mid-span flange bottom strain data from B8 trigger events.

One B3 strain gauge trigger event with relatively high mid-span flange bottom strains, from early in the monitoring phase, is shown in Figure 58. This event occurred on Tuesday, October 25th at 4:57 p.m. and is shown at 22 seconds of the complete time-histories of the B3 trigger events in Figure 56. The figure shows relatively large strain values occurred at the mid-span flange bottoms of the steel tee sections.

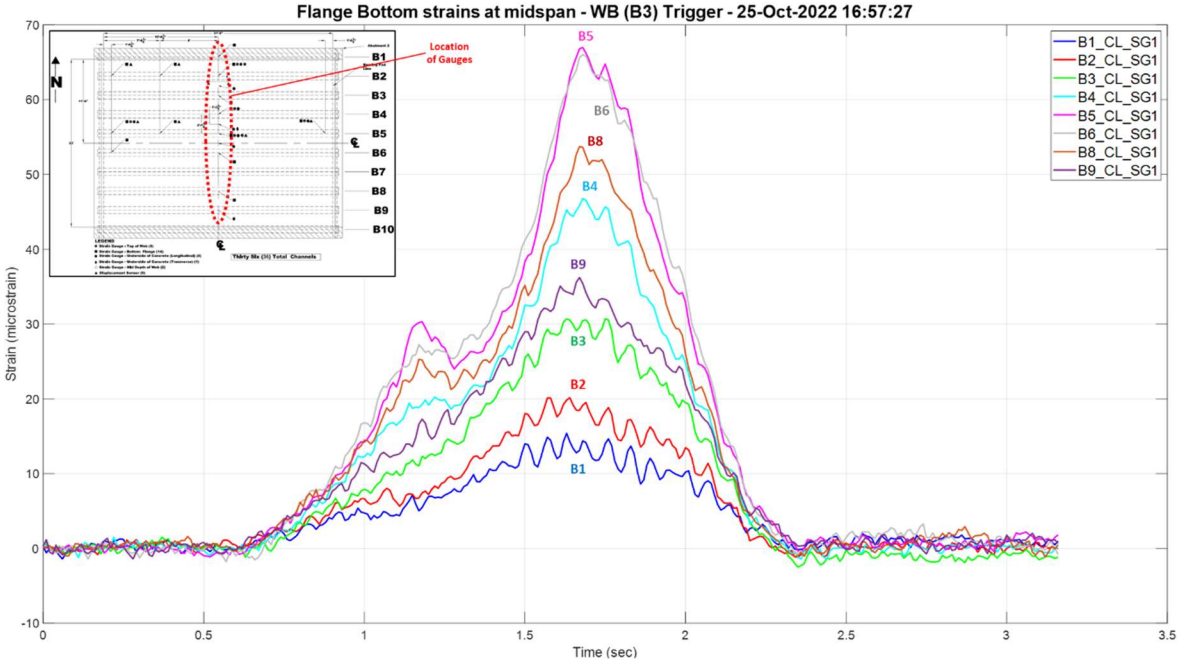

Figure 58. Mid-span flange bottom strains (B3 trigger event at 22 seconds of complete time-histories).

Corresponding maximum stress values of 1.94 ksi occurred on the flange bottom of steel tee section B5, and 1.91 ksi occurred on the flange bottom of steel tee section B6. For comparison, the maximum stress observed during controlled-load testing (under the 77.55-kip ATT), at the same location on B5 and B6 was approximately 3.1 ksi. The data in Figure 58 also shows that steel tee sections B8 and B9 had larger stresses than B3 and B2, respectively. This observation, suggests that the vehicle for this trigger event was closer to the south parapet than to the north parapet, and thus was likely traveling in the eastbound direction. It is also possible, however, that the vehicle was close to mid-width of the bridge and the south side of the vehicle was more heavily loaded than the north side of the vehicle.

For this same trigger event (October 25, 4:57 p.m.), time-histories of the measured strains over the depth of the composite steel tee section at mid-span of B5 are shown in Figure 59. A plot of the strain distribution over the cross-section at an arbitrary time (1.5 seconds) is provided on the right side of Figure 59. The dashed line is the best-fit straight line for the measured strain values from the three strain gauges over the depth of the composite section, which are B5_CL_SG1 on the flange bottom, B5_CL_SG4 at mid-depth of the (exposed) web, and DK_4_5_SG2 on the bottom of the concrete deck; note that strain gauge DK_4_5_SG2 is midway between steel tee sections B4 and B5, and not near the steel tee section web of B5. The strain distribution plot compares the measured values from the strain gauges with the values from the best-fit line (in parentheses). Similar to the results from the controlled-load testing, the relatively small differences between the measured values and best-fit line (i.e., 0.3 microstrain corresponding to 0.01 ksi) validate the plane-section assumption. As expected, the flange bottom has the largest strain (tension, from positive bending), and the strains decrease accordingly over the height of the composite section. At the arbitrary time (1.5 seconds) of this trigger event, the neutral axis at mid-span of B5 is 16.32 in. above the bottom of the flange, and compressive strain is observed at the centroid of the transformed-section model. The corresponding (compressive) stress at the centroid is –0.03 ksi, and the corresponding compressive axial force is –1.3 kips.

Since strain gauge DK_4_5_SG2 is on the bottom of the concrete deck at a location between B4 and B5, and is subject to localized deck bending, the data from this strain gauge is not consistent with the plane-section assumption at all times in the time-history. The strain time-history for strain gauge DK_4_5_SG2 includes local response shown as relatively large (positive) maxima that occur between the 1.0 and 2.0 seconds of the time-history. This local response, which was also observed during controlled-load testing, suggests that the wheels on one side of the vehicle passed near the transverse mid-distance between steel tee sections B4 and B5, with each local strain maxima corresponding to the passage of one axle of the vehicle over the strain gauge location. The localized strain maxima are seen in the data from the strain gauge on the concrete deck (DK_4_5_SG2), but not on the other gauges, because the deck is subjected to localized bending at the location of DK_4_5_SG2, while the other strain gauges on the steel tee section are at locations subjected to primary bending only.

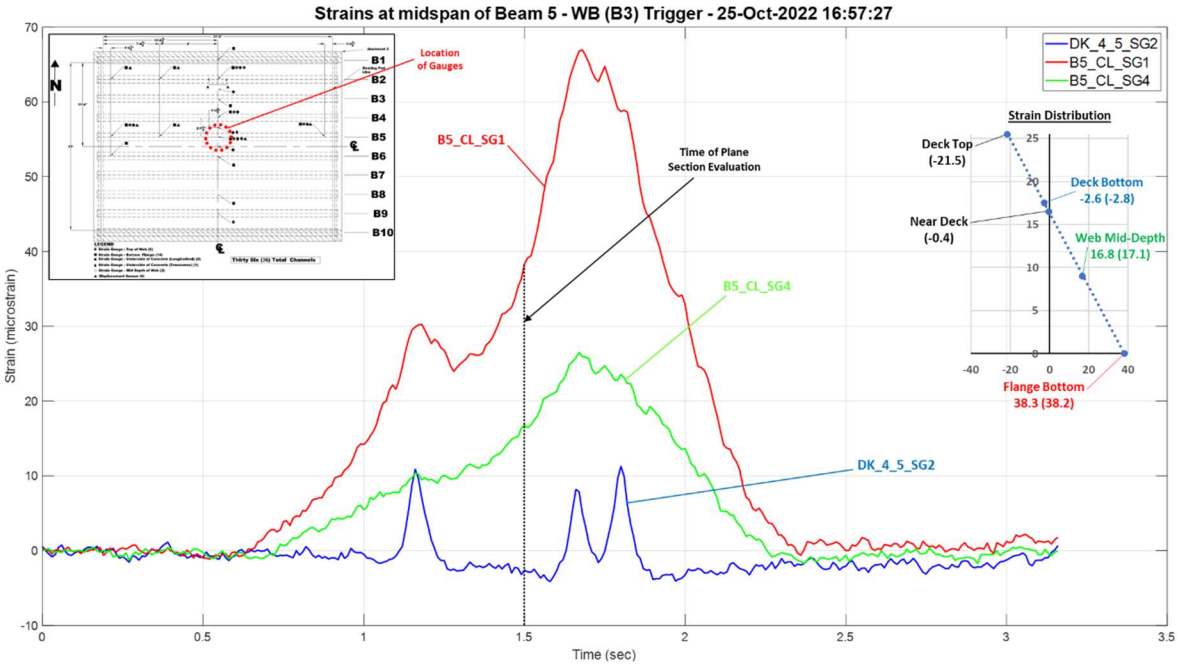

Figure 59. Mid-span strains over depth of composite steel tee section B5 (B3 trigger event at 22 seconds of complete time-histories).

Figure 60 shows the measured longitudinal strain (from DK_4_5_SG2) and transverse strain (from DK_4_5_SG5) on the bottom of the concrete deck between steel tee sections B4 and B5. The transverse strain (from DK_4_5_SG5) appears to be dominated by overall transverse bending of the bridge as the vehicle passes over the bridge, without as much sensitivity to the individual axles as the longitudinal strain (from DK_4_5_SG2).

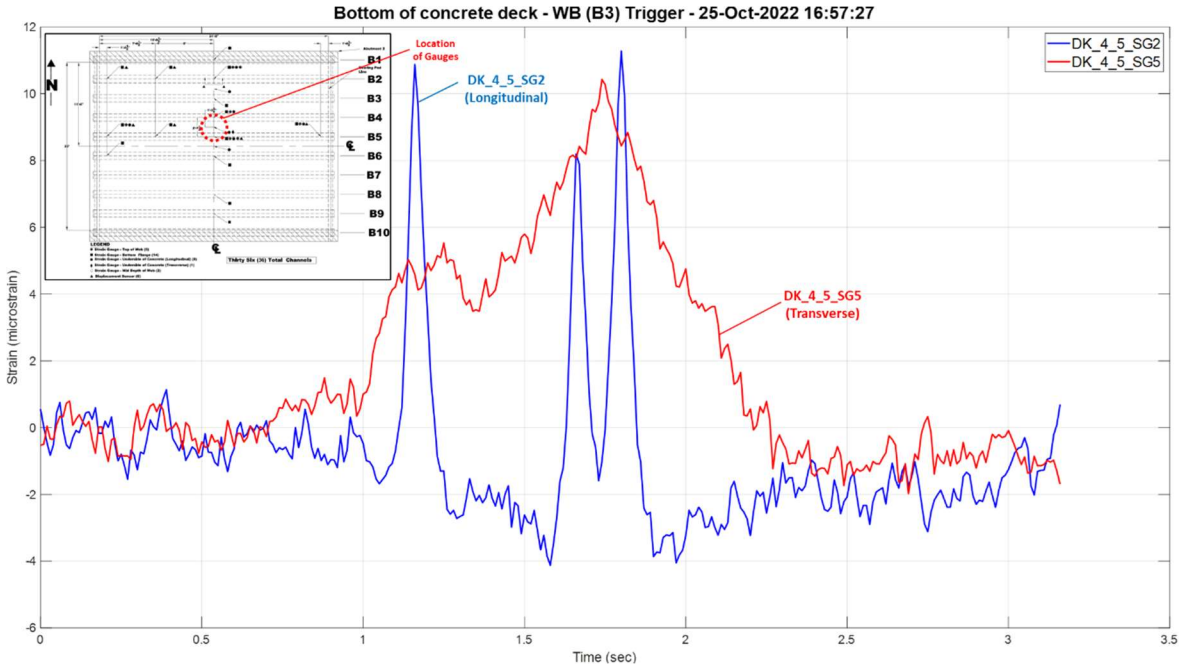

Figure 60. Mid-span strains at bottom of concrete deck between B4 and B5 (B3 trigger event at 22 seconds of complete time-histories).

Figure 61 shows the flange bottom strain time-history near the west bearing of steel tee section B5 for the same trigger event (October 25, 4:57 p.m.). As mentioned earlier, the mid-span flange bottom strain distribution among the composite steel tee sections, shown in Figure 58, suggests that the vehicle for this trigger event was closer to the south parapet than to the north parapet, and thus was likely traveling in the eastbound direction. The data in Figure 61, however, suggest that the vehicle was traveling in the westbound direction. The time-history in Figure 61 shows a general trend toward negative strain (from negative bending) in response to the vehicle approaching and reaching the mid-span, with a local cycle of strain variation (first positive, then negative) from the front axle reaching the strain gauge location (near the west bearing) followed by a larger local cycle of strain variation as rear axle(s) reaching the strain gauge location, similar to the strain history shown in Figure 49 from crawl Test 1 (with the test truck in the westbound direction). Thus, it appears that the vehicle was both traveling in the westbound direction and closer to the south parapet than to the north parapet, which is not unexpected, since the road is narrow and without lane markings, and a vehicle may become positioned transversely toward the wrong side of the road. Importantly, the data in Figure 61 shows the tendency for negative bending near the bearing as the vehicle reaches mid-span, similar to the data from the controlled load testing.

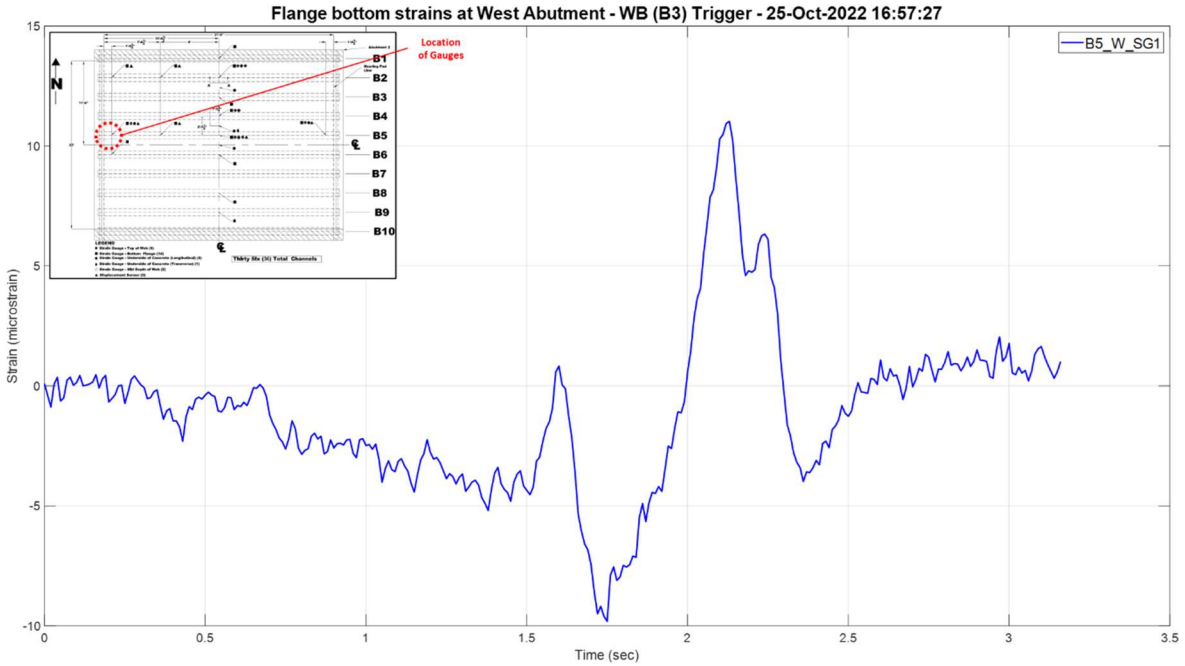

Figure 61. Flange bottom strain for B5 near west bearing (B3 trigger event at 22 seconds of complete time-histories).

Figure 62 shows another B3 strain gauge trigger event with relatively high mid-span flange bottom strains from Saturday November 5th at 6:30 p.m. (at 2752 seconds of the complete time-histories of the B3 trigger events in Figure 56). Corresponding maximum stress values of 1.71 ksi occurred on the flange bottom of steel tee section B6, and 1.63 ksi occurred on the flange bottom of steel tee section B5. The flange bottom strains have a nearly symmetrical distribution with respect to a longitudinal axis at mid-width of the bridge (i.e., steel tee sections B2 and B9, as well as B3 and B8, have similar strain histories), which suggests the vehicle was centered transversely at the mid-width of the bridge.

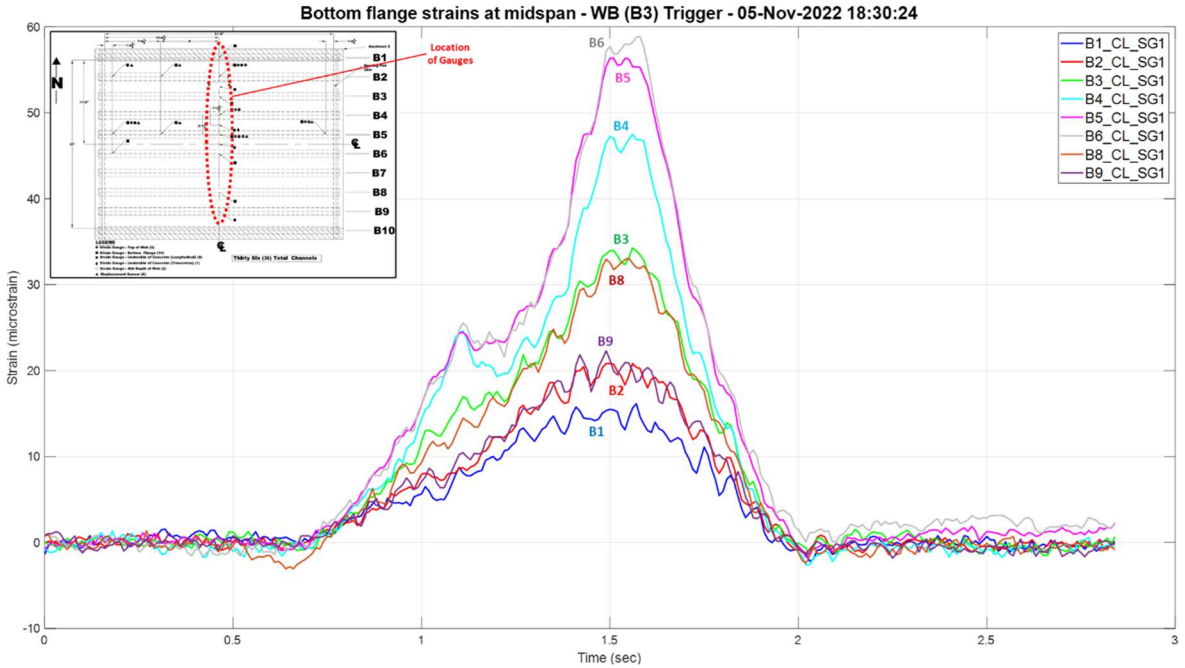

Figure 62. Mid-span flange bottom strains (B3 trigger event at 2752 seconds of complete time-histories).

For this same trigger event (November 5, 6:30 p.m.), time-histories of the measured strains over the depth of the composite steel tee section at mid-span of B5 are shown in Figure 63. A plot of the strain distribution over the cross-section at an arbitrary time (1.65 seconds) is provided on the right side of Figure 63. The dashed line is the best-fit straight line for the measured strain values from the three strain gauges over the depth of the composite section, which are B5_CL_SG1 on the flange bottom, B5_CL_SG4 at mid-depth of the (exposed) web, and DK_4_5_SG2 on the bottom of the concrete deck. The strain distribution plot compares the measured values from the strain gauges with the values from the best-fit line (in parentheses) and relatively small differences between the measured values and best-fit line (i.e., 0.4 microstrain corresponding to 0.01 ksi) are seen, which validate the plane-section assumption. At the arbitrary time (1.65 seconds) of this trigger event, the neutral axis at mid-span of B5 is 16.47 in. above the bottom of the flange, and compressive strain is observed at the centroid of the transformed-section model. The corresponding (compressive) stress at the centroid is –0.02 ksi, and the corresponding compressive axial force is –0.9 kips.

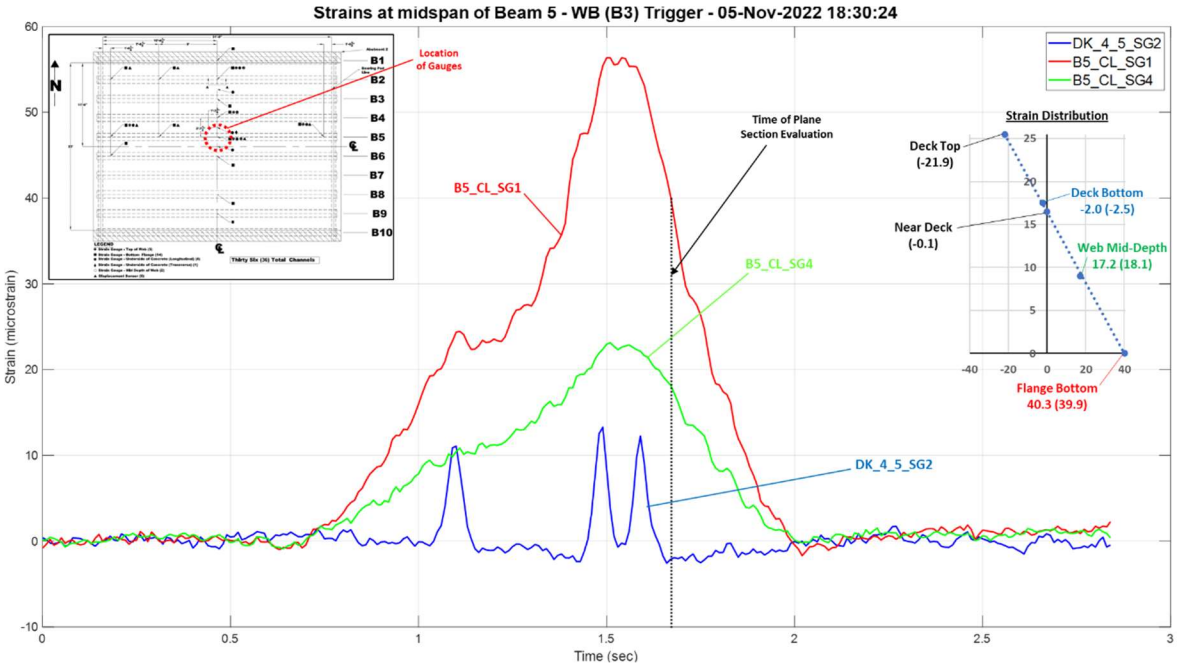

Figure 63. Mid-span strains over depth of composite steel tee section B5 (B3 trigger event at 2752 seconds of complete time-histories).

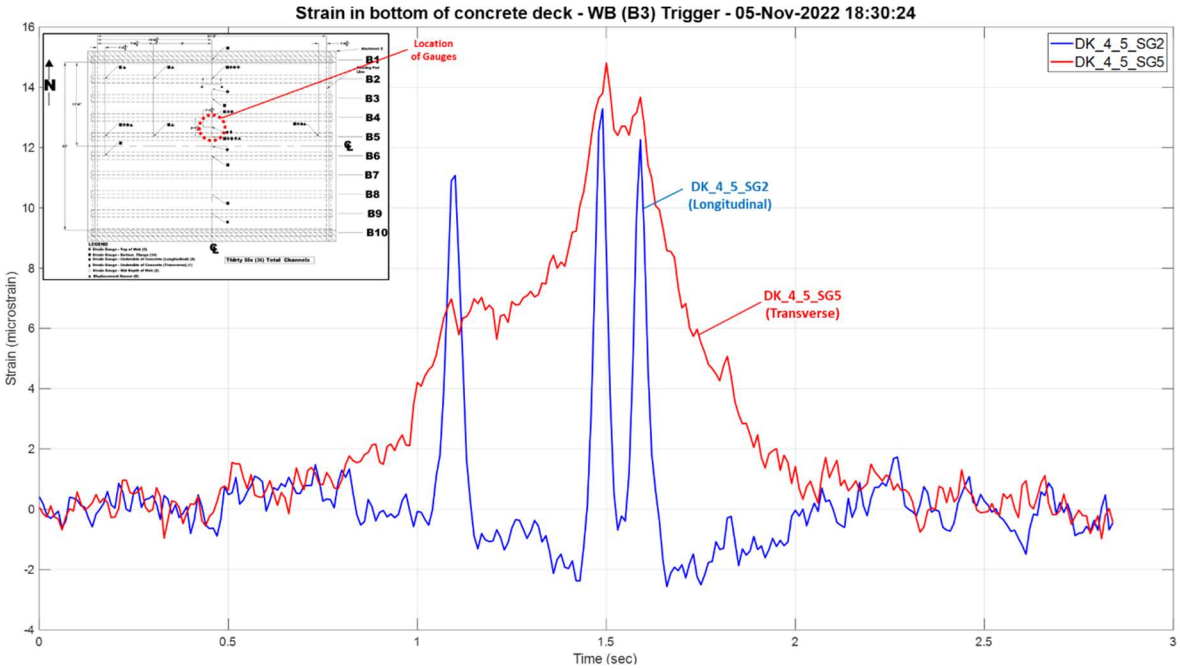

Figure 64. Mid-span strains at bottom of concrete deck between B4 and B5 (B3 trigger event at 2752 seconds of time-history).

Figure 64 shows the measured longitudinal strain (from DK_4_5_SG2) and transverse strain (from DK_4_5_SG5) on the bottom of the concrete deck between steel tee sections B4 and B5 for this same trigger event (November 5, 6:30 p.m.). This data is similar to the data shown in Figure 60 for the previous event (October 25, 4:57 p.m.) with slightly larger strains during the November 5, 6:30 p.m. event.

Figure 65 shows the flange bottom strain time-history near the west bearing of steel tee section B5 for the same trigger event (November 5, 6:30 p.m.). This data is similar to that shown in Figure 61 for the previous event (October 25, 4:57 p.m.) and suggests that the vehicle that was traveling in the westbound direction. Also, similar to the data in Figure 61, the data in Figure 65 shows the tendency for negative bending near the bearing as the vehicle reaches mid-span, similar to the data from the controlled load testing.

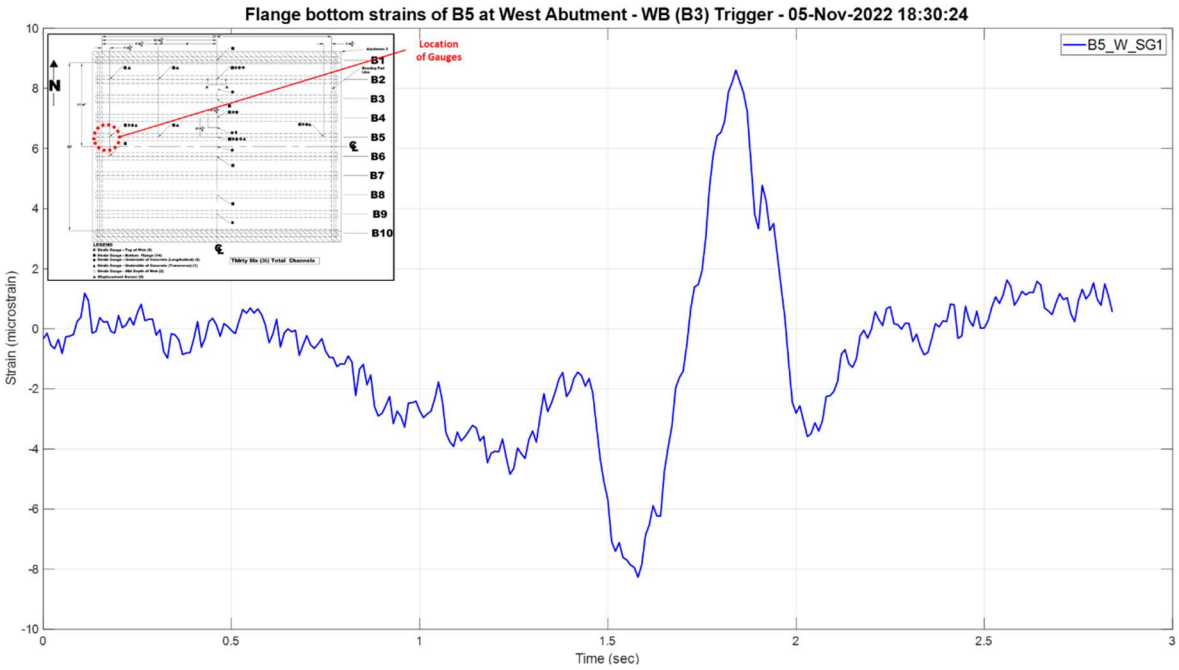

Figure 65. Flange bottom strain for B5 near west bearing (B3 trigger event at 2752 seconds of complete time-histories).

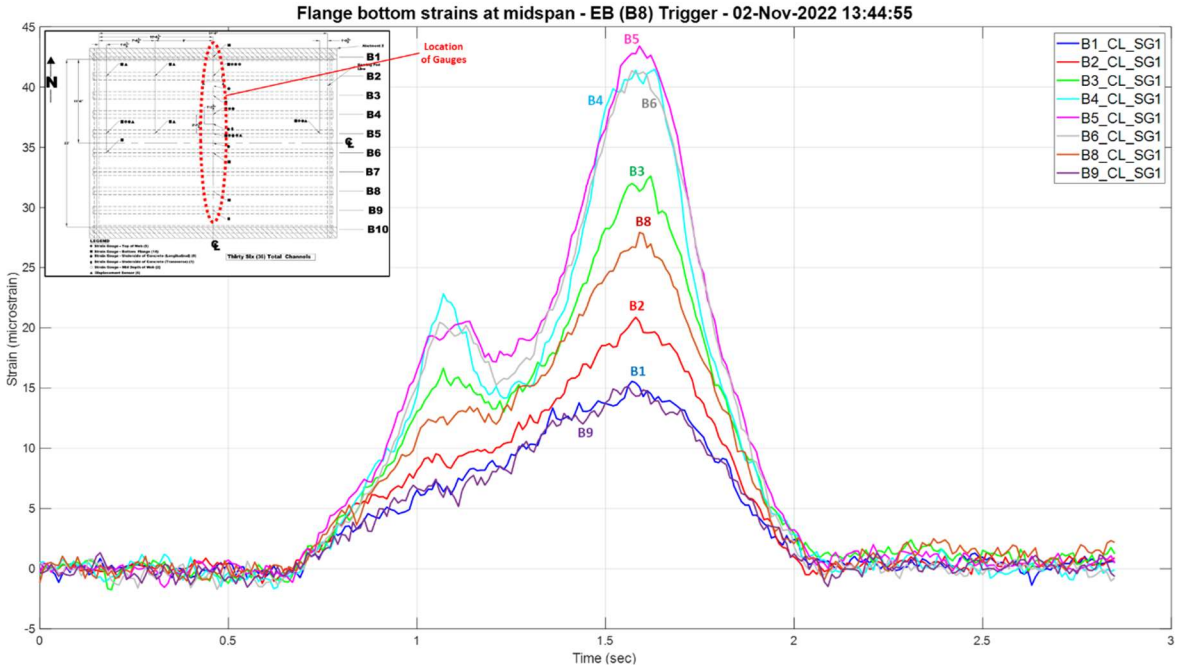

Figure 66. Mid-span flange bottom strains (B8 trigger event at 4235 seconds of complete time-histories).

Figure 66 shows the flange bottom strains at mid-span of steel tee sections B1, B2, B3, B4, B5, B6, B8, and B9 after a trigger from the strain gauge on B8. This event occurred on Wednesday, November 2nd at approximately 1:45 p.m. (at 4235 seconds of the complete time-histories of the B8 trigger events shown in Figure 57). The maximum stress of 1.26 ksi occurred on steel tee section B5 and stresses of 1.20 ksi occurred on both steel tee sections B4 and B6. Figure 66 shows that (comparing steel tee sections B2 with B9 and B3 with B8) the steel tee sections in the north half of the bridge have slightly higher strains than their counterparts in the south half of the bridge.

For this same trigger event (November 2nd, 1:45 p.m.), time-histories of the measured strains over the depth of the composite steel tee section at mid-span of B5 is shown in Figure 67. A plot of the strain distribution at an arbitrary time (approximately 1.7 seconds) is provided on the right side of the figure, where the dashed line is the best-fit straight line for the measured strain values. The relatively small differences between the measured values and best-fit line (i.e., 1.1 microstrain corresponding to 0.03 ksi) show the measured strain distribution is consistent with a linear strain distribution that corresponds to the plane-section assumption. At the arbitrary time (1.7 seconds) of this trigger event, the neutral axis at mid-span of B5 is 16.06 in. above the bottom of the flange, and compressive strain is observed at the centroid of the transformed-section model. The corresponding (compressive) stress at the centroid is –0.04 ksi, and the corresponding compressive axial force is –1.8 kips. These results for this B8 strain gauge trigger event (November 2nd, 1:45 p.m.) are similar to the results shown previously for B3 strain gauge trigger events.

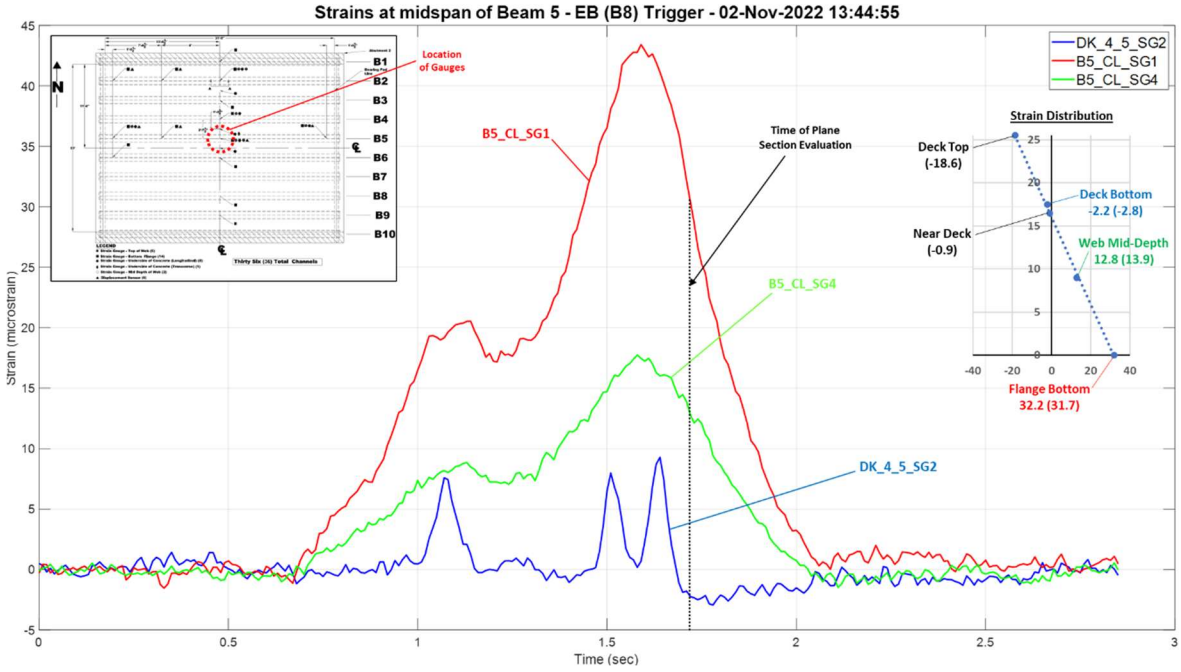

Figure 67. Mid-span strains over depth of composite steel tee section B5 (B8 trigger event at 4235 seconds of complete time-histories).

The strain time-histories from the trigger events discussed thus far suggest that the trigger events were from tri-axle vehicles passing over the bridge, based on the similarity to data from the controlled-load testing with a tri-axle test truck. In particular, the data from strain gauge DK_4_5_SG2 on the bottom of the concrete deck between steel tee sections B4 and B5, shown in Figure 59, Figure 60, Figure 63, Figure 64, and Figure 67, indicate the passage of three axles. The data generally follow a nearly pseudo-static pattern of response, consistent with the relative location of the gauge and the vehicle and its axles, as the vehicle crosses the bridge. Minor oscillations in the data are attributed to small amplitude vibrations of the bridge and unavoidable noise in the data.

The roadway on the Flex Beam demonstration bridge and on its approaches was smooth, and strain time histories from the dynamic tests during controlled-load testing did not have significant oscillations. A few trigger events from the monitoring phase, however, did provide strain time-histories with significant oscillations. Strain time-histories from two B3 strain gauge trigger events, for strains at the flange bottom at mid-span, both on Tuesday, November 8th, are presented in Figure 68 (5:47 p.m.) and Figure 69 (6:45 p.m.). The event at 5:47p.m. (Figure 68) produced the largest strain values in steel tee sections B5, B6, B4, and B3, with corresponding maximum stresses of 0.73, 0.71, 0.71, 0.65 ksi, respectively. Comparing the strains between steel tee sections B2 and B9 and between B3 and B8, it is observed that the steel tee sections in the north half of the bridge have larger strains than those in the south half of the bridge. The event at 6:45

p.m. (Figure 86) produced the largest strain values in steel tee sections B6, B5, and B8, with corresponding maximum stresses of 0.81, 0.80, and 0.71 ksi, respectively. Comparing the strains between steel tee sections B2 and B9 and between B3 and B8, it is observed that the steel tee sections in the south half of the bridge have larger strains than those in the north half of the bridge.

The significant oscillations in the strain time-histories from Tuesday, November 8th, shown in Figure 68 (5:47 p.m.) and Figure 69 (6:45 p.m.), could correspond to vertical vibration of the bridge or to pseudo-static response of the bridge to a vehicle with many axles. For the trigger event at 5:47 p.m., Figure 70 shows time-histories of the measured strains over the depth of the composite steel tee section at mid-span of B5. The strain time-history from strain gauge DK_4_5_SG2 on the bottom of the concrete deck between steel tee sections B4 and B5 in Figure 70 suggests the vehicle is a two-axle vehicle, with a local strain maxima from passage of the first axle (i.e., the lightest of the two axles) occurring at approximately 1.02 seconds, and a local strain maxima from passage of the second axle (i.e., the heaviest of the two axles) occurring at approximately 1.45 seconds. Similarly, for the trigger event at 6:45 p.m., Figure 71 shows measured strain time-histories for the composite steel tee section at mid-span of B5, and the strain time-history from strain gauge DK_4_5_SG2 also suggests the vehicle is a two-axle vehicle, with a local strain maxima from passage of the first axle (i.e., the lightest of the two axles) occurring at approximately 0.73 seconds, and a local strain maxima from passage of the second axle (i.e., the heaviest of the two axles) occurring at approximately 1.13 seconds. Although the time histories from strain gauge DK_4_5_SG2 shown in Figure 70 and Figure 71 are different from those from the trigger events discussed previously (shown in Figure 59, Figure 60, Figure 63, Figure 64, and Figure 67 which indicate the passage of three axles), the time histories shown in Figure 70 and Figure 71 do not suggest the passage of a vehicle with many (e.g., more than three) axles.

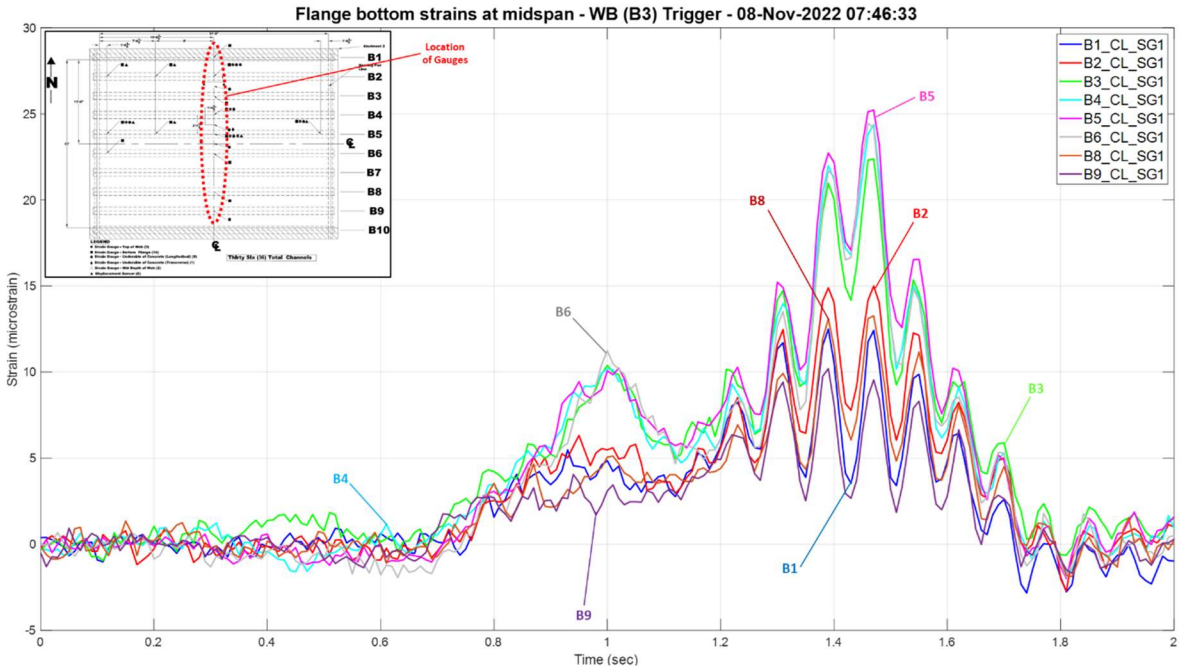

Figure 68. Mid-span flange bottom strains (B3 trigger event at 4493 seconds of complete time-histories).

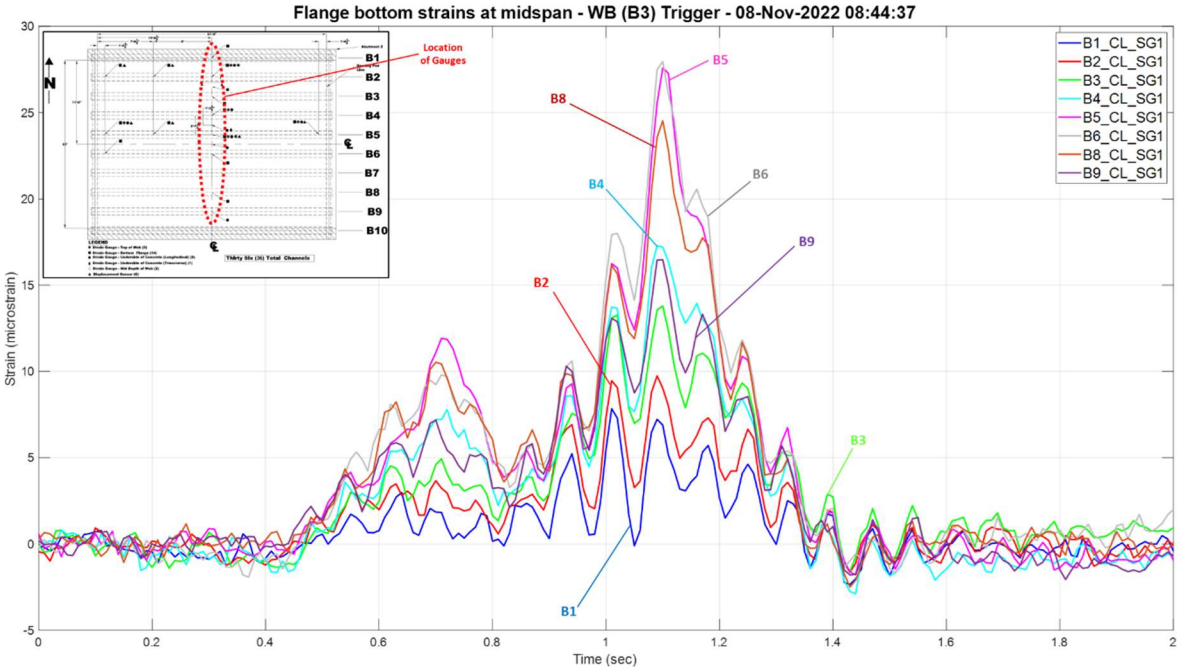

Figure 69. Mid-span flange bottom strains (B3 trigger event at 4496 seconds of complete time-histories).

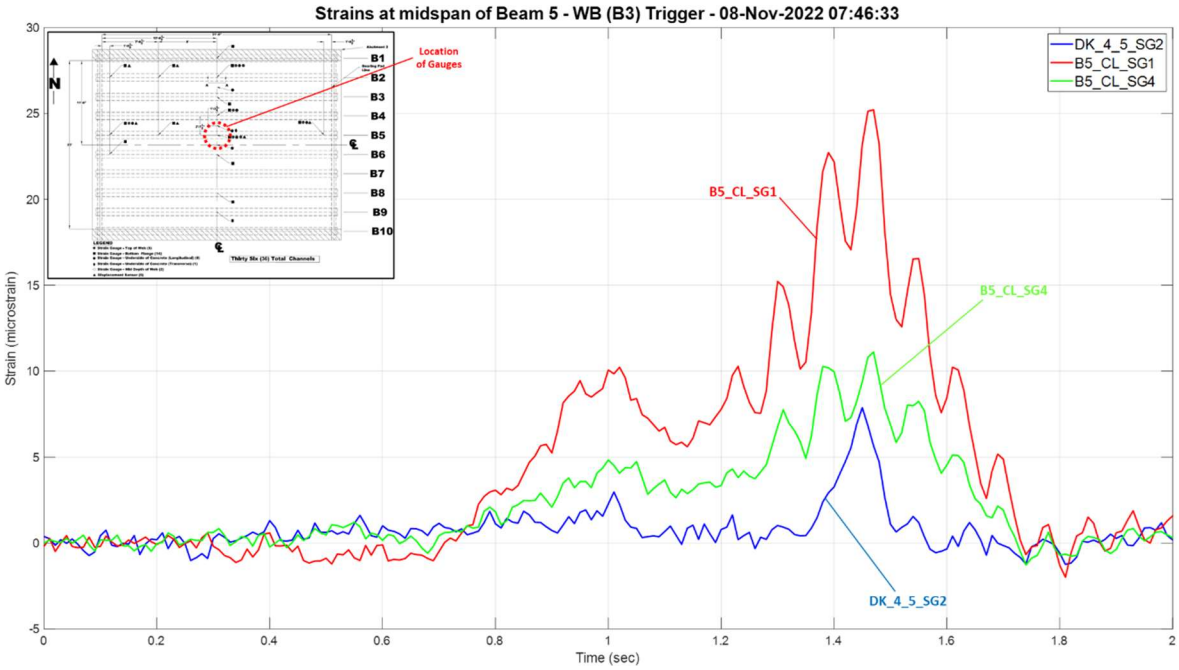

Figure 70. Mid-span strains over depth of composite steel tee section B5 (B3 trigger event at 4493 seconds of complete time-histories).

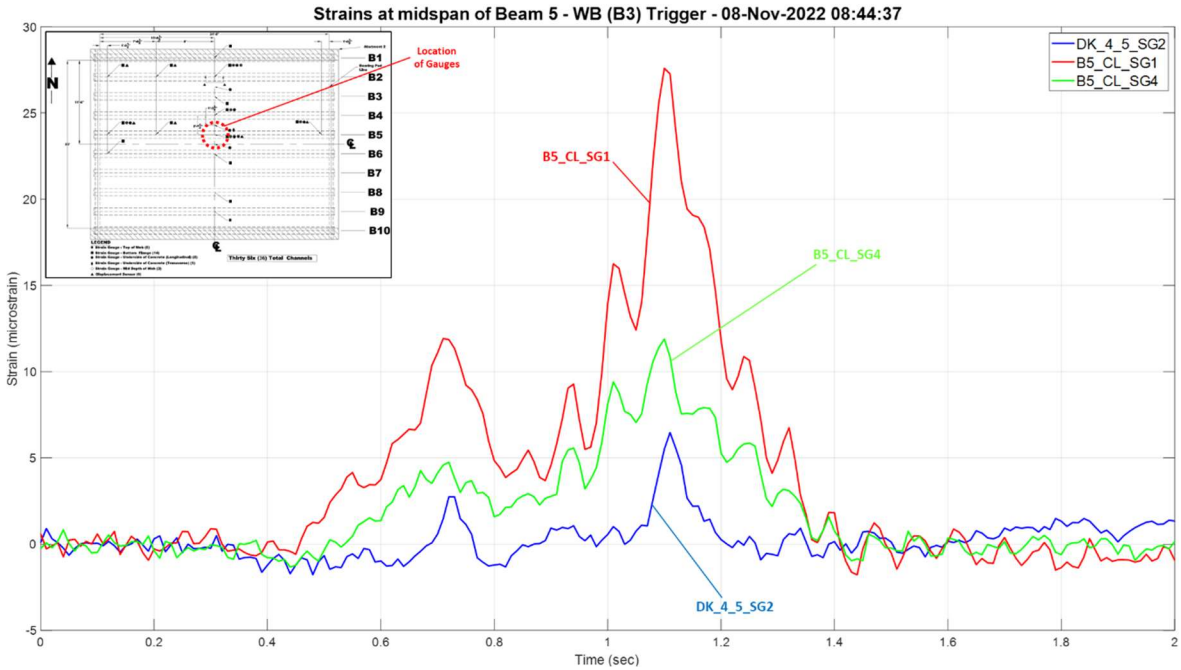

Figure 71. Mid-span strains over depth of composite steel tee section B5 (B3 trigger event at 4496 seconds of complete time-histories).

A notable feature of the significant oscillations in the strain time-histories from these November 8th trigger events in Figure 68 (5:47 p.m.) and Figure 69 (6:45 p.m.) is the amplitudes of the oscillations relative to the peak values for strain gauges on composite steel tee sections that are not heavily loaded when the vehicle is near mid-width of the bridge. As shown in Figure 68 (5:47 p.m.) and Figure 69 (6:45 p.m.), the amplitudes of the largest local oscillations (from local peak to local valley) for the strain gauges at mid-span of steel tee sections B1, B2, and B9 are approximately 40% to 100% of the peak values, while for strain time-histories at mid-span of B1, B2, and B9 from dynamic Test 7 (Figure 53) and from the trigger events discussed previously (Figure 58, Figure 62, and Figure 66) the amplitudes of the largest local oscillations are about 10% of the peak values. These results indicate that the strain responses of steel tee sections B1, B2, and B9 (away from the mid-width of the bridge and near the parapets) from the November 8th trigger events are dominated by vertical vibration of the bridge, which suggests that the significant oscillations in all of the strain time-histories are from vertical vibration of the bridge. The vehicle characteristics that produce this vertical vibration are unknown, however, since the largest mid-span flange bottom stresses are relatively small (less than 1 ksi), the vehicles that produced these trigger events do not appear to be heavy.

3.3.2. Monitoring Summary

Data from monitoring of the Flex beam bridge under typical vehicular loading was collected for a period of approximately six weeks, from Tuesday, October 25 without interruption until Thursday, December 08. During the evening of Friday, November 11, or morning of Saturday, November 12, possibly due to bad weather in the area during that week, the mid-span flange bottom strain gauge on steel tee section B6 (B6_CL_SG1) stopped functioning properly. All other sensors functioned properly for the duration of the monitoring phase. The data from monitoring under typical vehicular loading were consistent with the data from the controlled-load testing. The strains and stresses were as expected. Some oscillations in the strain data, greater than those observed from the controlled-load testing, were observed. However, the largest strains and stresses were significantly smaller than those from the controlled-load testing. Trigger events with relatively similar strain values occurred during both weekdays and weekend days.

The response of the bridge to typical vehicular loading did not deviate from that observed during controlled-load testing. The strains (and corresponding stresses) recorded for all trigger events were much smaller than

the maximum values measured during controlled-load testing. The largest flange bottom stress observed from typical vehicular loading (1.94 ksi) is approximately 65 percent of the largest stress measured during controlled-load testing (3.07 ksi). A small level of reverse (negative) bending of the steel tee sections near the bearings (as observed during controlled-load testing) was observed in strains measured by the strain gauge on the flange bottom of steel tee section B5 near the west bearing. The observed negative bending is discussed in greater detail in the next chapter.

In summary, the monitoring of the Flex Beam bridge under typical vehicular loading provided data and associated observations similar to those from controlled-load testing. The data from monitoring were consistent with the data from controlled-load testing. The strains and stresses were as expected. Strains across the depth of the most heavily-loaded composite steel tee sections were consistent with the plane-section assumption from beam theory used for analysis and design of Flex Beam units.

3.4. Summary

Through instrumentation and controlled-load testing, the response of the Flex Beam bridge to the known loading of the test truck in specified positions was measured. The data is useful for validating assumptions made in the design and analysis of Flex Beam bridges and to validate and calibrate finite element analysis (FEA) models. Controlled-load testing of the bridge was performed using a test truck of known weight and dimensions, which was parked at different locations or driven at specified speeds and transverse paths on the bridge to assess load distribution and to validate and calibrate numerical models. The bridge was then monitored for a period of time to assess the response of the bridge to typical vehicular loading. Overall, the data from controlled-load testing and subsequent monitoring show that the composite steel tee sections of the Flex Beam system are fully composite away from the concrete end diaphragms (and bearings) and the plane-section assumption and a transformed-section model are appropriate for analysis of the Flex Beam system units. Fully composite action was not observed near the bearings of the bridge, and this observation will be discussed further in the next chapter. Relative displacements between the concrete deck and the web of the steel tee sections were very small.

CHAPTER 4: FINITE ELEMENT ANALYSIS

4.1. Background

Finite element analysis (FEA) of the Flex Beam demonstration bridge was conducted in two phases, namely *pre-test analyses* and a *post-test analyses*. The pre-test analyses had two objectives: (1) to provide information needed to develop the instrumentation plan; and (2) to assess various modeling and analysis approaches. To meet the second objective, the analyses included a conventional line-girder analysis, often used in conventional design and assessment calculations, and FEA using FEA models of different levels of complexity. The simplest FEA models used shell elements and omitted the effects of bridge components such as the parapets, concrete end diaphragms, and bearing pads. These bridge components may affect the structural response of the Flex Beam bridge, but were not included in the FEA models used in previous research (Naito, Hendricks, & Sause, 2018b). In the post-test analyses, a FEA model of the Flex Beam demonstration bridge was developed and calibrated with the park test data from the controlled-load testing of the bridge, to better reflect the in-situ conditions of the bridge. This validated FEA model can be used to examine loading cases that cannot be implemented in the field. This chapter presents these pre-test and post-test analyses of the bridge.

4.2. Loading Used in Analyses

The FEA used commercial finite element software (SAP2000). As discussed in Chapter 2, properties (geometry and weight) of a standard PennDOT triaxle dump truck (with the fourth (tag) axle raised and not in contact with the bridge deck) were used as the load model in the analyses (see Figure 7). Two test truck geometries and weights were used (see Figure 8). In the pre-test analyses, the properties of a Nominal Test Truck (NTT) were used for the load model. In the post-test analyses, the load model was based on the properties of the actual test truck (ATT) from the controlled-load testing of the bridge. The geometry of the ATT was measured on-site by Lehigh University researchers and the axle weights (and wheel loads) were measured by a Pennsylvania State Police Weight Enforcement Team. Note that the wheel loads of the NTT are symmetrical about the longitudinal axis of the truck, while the ATT wheel loads are not symmetrical about the longitudinal axis, and this difference was included in the FEA.

Area pressure loads on the bridge concrete deck are used to represent the wheel loads. In the pre-test analyses a 10 in. x 10 in. square area is used for each single wheel of the front axle and a 10 in. x 20 in. rectangle is used for each of pair of wheels of the rear tandem axle. For the post-test analyses, a 10 in. x 13 in. rectangle is used for each single front wheel, and a 10 in. x 22 in. rectangle is used for each pair of wheels of the rear tandem axle. The loading was applied at three transverse positions, namely: (**1**) mid-width of the bridge, (**2**) mid-lane, and (**3**) with the centroid of the wheels at 2 ft. from the parapet (i.e., roadway edge). For each transverse position, three longitudinal positions were considered, namely: (**1**) the truck centered on mid-span; (**2A**) a truck position with the front axle of the tandem axle centered on the bearing, the rear axle of the tandem on the bridge, and the front axle of the truck off the bridge; (**2B**) a truck position with the rear axle of the tandem axle centered on the bearing, the front axle of the tandem axle and the front axle of the truck on the bridge; and (**3**) a truck position with the tandem axle centered at mid-span (and the front axle of the truck off the bridge). Figure 72, Figure 73, and Figure 74 show the NTT load model in Longitudinal Position 1 (Truck Centered in Span), directed westbound, and in the three transverse positions.

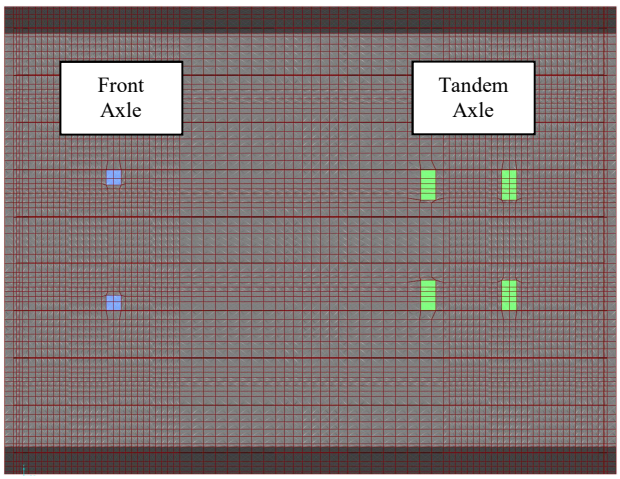

Figure 72. NTT load model (Model 4: Transverse Position 1, Longitudinal Position 1). Test truck wheel load shown in blue (front axle) and green (tandem axle).

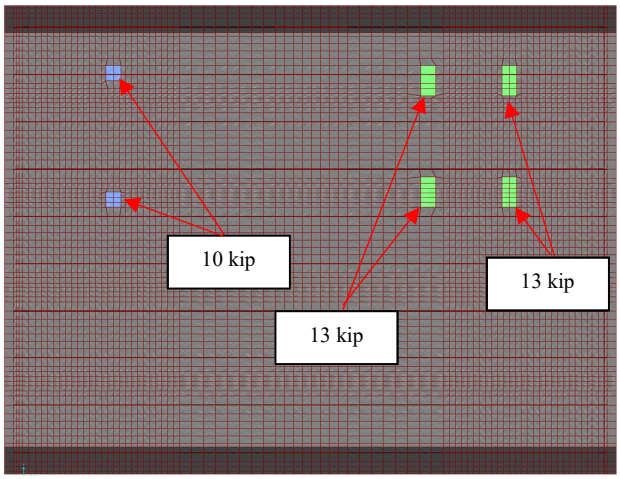

Figure 73. NTT load model (Model 4: Transverse Position 2, Longitudinal Position 1). Test truck wheel load shown in blue (front axle) and green (tandem axle).

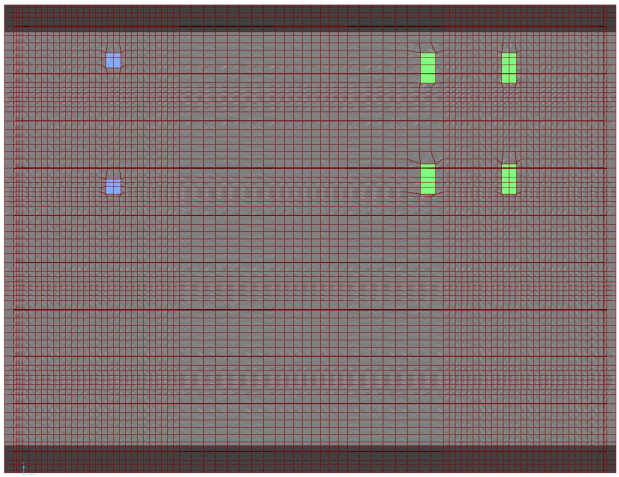

Figure 74. NTT load model (Model 4: Transverse Position 3, Longitudinal Position 1). Test truck wheel load shown in blue (front axle) and green (tandem axle).

4.3. Description of FEA Models

In the pre-test analyses, the effects of various bridge components, parapets, end diaphragms, and bearing details on the response of the bridge were studied using several FEA models. In the post-test analyses, the most complex and accurate FEA model from the pre-test analyses was calibrated using results from the controlled-load testing to consider in-situ conditions. The calibrated FEA model was used to extract further information about the structural response of the bridge that is useful to validate the basis for design of a Flex Beam bridge. The FEA models are summarized in Table 5.

Four FEA models, along with a line-girder analysis, were used in the pre-test analyses. Three of these FEA models were comprised of shell elements and one model was comprised of solid (i.e., brick) elements. A fifth (calibrated) FEA model was used in the post-test analyses. Conventional U.S. units (kip and in.) were used for each model. Linear-elastic response was assumed for each model with steel elastic modulus (E_s) and Poisson's ratio (v_s) of 29,000 ksi and 0.3, respectively, and concrete elastic modulus (E_c) and Poisson's ratio (v_s) of 3,625 psi and 0.2, respectively. When the bearing pads were modeled with springs, the total stiffness was 1,066 kip/in for the vertical direction and 30 kip/in for the longitudinal direction, based on previous research results (Naito, Hendricks, & Sause, 2018b).

Three finite element models based on shell elements were created and analyzed: (1) Model 1 has simple pin and roller supports (to model the bearings), and includes the concrete deck, steel tee sections, and end diaphragms modeled as shell elements, as well as the interface shear connections modeled as springs; (2) Model 2 is an extension of Model 1, which includes the parapets that flank the roadway, modeled as shell elements; and (3) Model 3 is an extension of Model 2, which includes distributed springs to model the bearing pads, rather than simple pin and roller supports. Model 1 is shown in Figure 75 and Model 2 is shown in Figure 76.

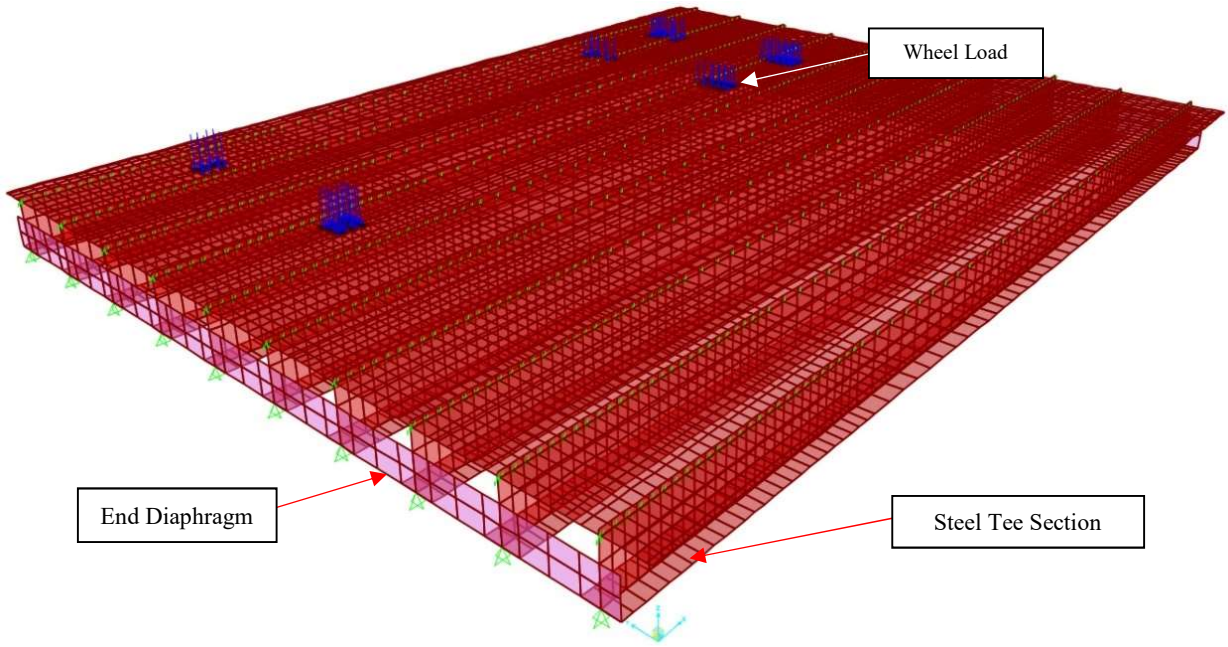

Figure 75. Model 1 (shell elements) shown with NTT in westbound direction (Transverse Position 2, Longitudinal Position 1).

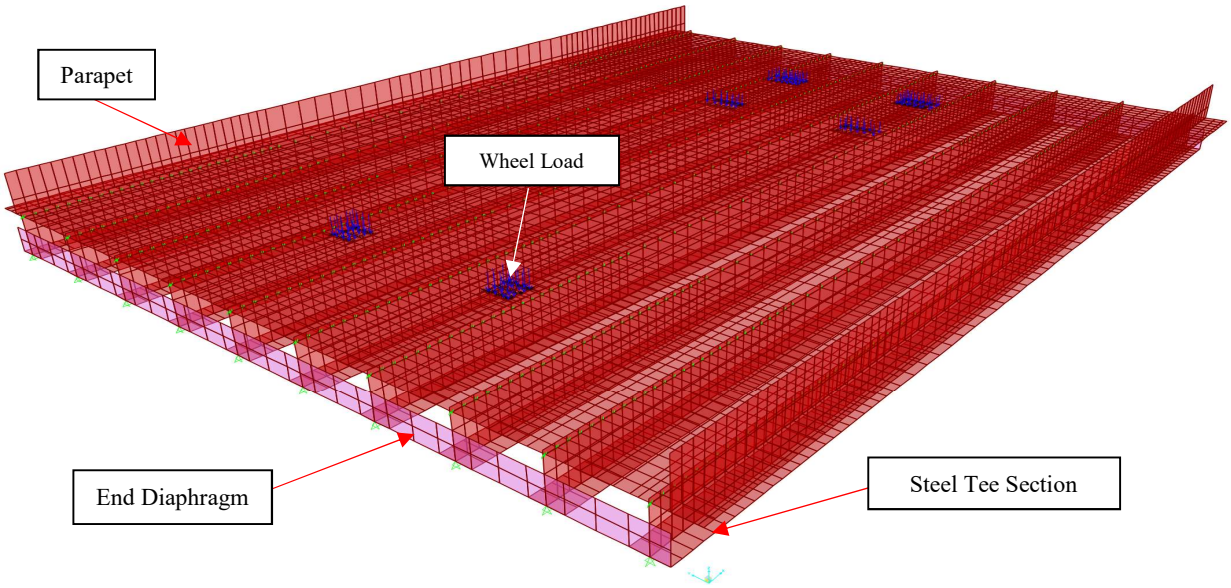

Figure 76. Model 2 (shell elements) shown with NTT in westbound direction (Transverse Position 1, Longitudinal Position 1).

Shell elements could not model certain aspects of the bridge, such as the torsional stiffness of the concrete end diaphragms. Therefore, Model 4, comprised of solid elements, was created to provide more accurate representation of the concrete end diaphragms and other geometric features of the bridge, such as the actual physical relationship of the parapets to the bridge deck. Model 4 includes the concrete end diaphragms and the steel bearing stiffener plates at the bearings. The bearing pad length is included (in the longitudinal direction of the bridge) to represent the effective span length of the bridge (relative to the bearing-to-bearing centerline dimension). Distributed area springs were used to model the bearing pads. Model 4, shown in Figure 77, was considered to be the most accurate FEA model of the bridge (for the pre-test analyses), and was used to provide information for developing the instrumentation plan. Model 5 is an extension of Model 4 that was calibrated to consider in-situ conditions. Model 5 is described later in this chapter.

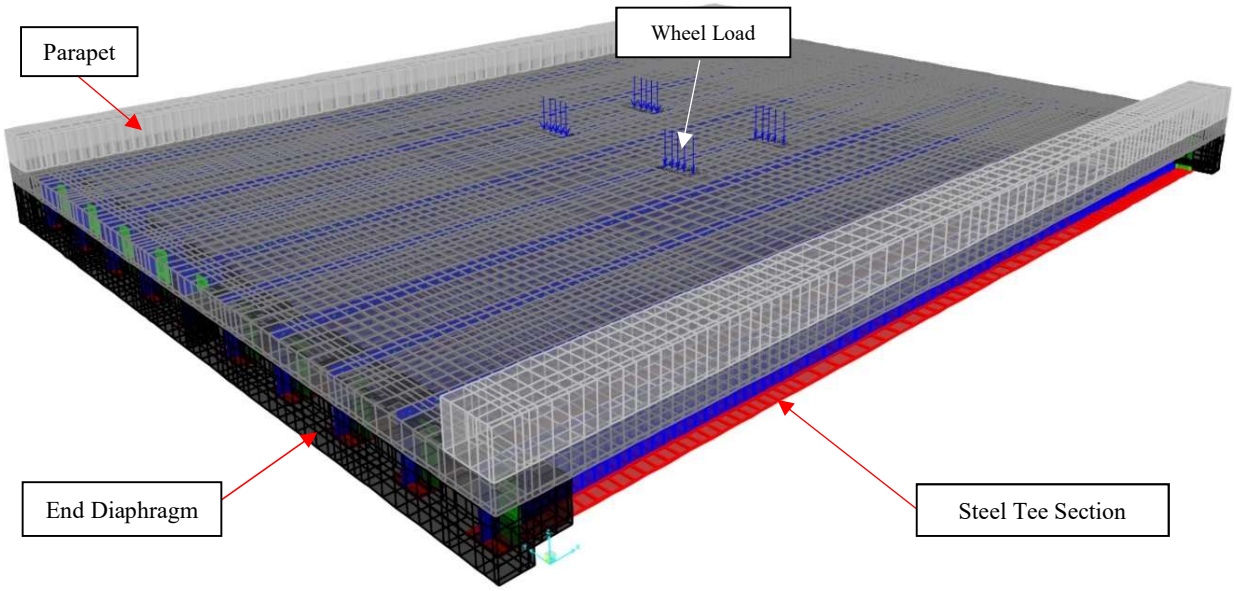

Figure 77. Model 4 (solid elements) shown with load from NTT rear tandem (Transverse Position 1, Longitudinal Position 3).

Shell elements are planar with a representative thickness that simulates a 3-D body. In the shell element models, the steel tee sections, parapets, and end diaphragms were modeled using a shell with uniform thickness perpendicular to and centered on the element plane (the thickness of the element is centered on the defined element plane). The shell elements modeling the concrete deck are "layered" shell elements which enables modeling of the eccentricity of the concrete deck mid-surface (i.e., mid-thickness of the concrete deck) relative to the interface shear connectors (located at the holes in the steel tee section web, below the mid-thickness of the deck). The deck shell element plane passes through the vertical locations of the interface shear connections (i.e., where the steel reinforcement dowels pass through the corresponding holes in the web), and the deck elements have unequal thickness above and below the element plane to represent the actual deck geometry with respect to the locations of the interface shear connections.

To simulate the interface shear connection response in both the shell and solid element models, a linear-elastic link element with a stiffness of 3,372 kip/in. was used at the location of each interface shear connection in the bridge, based on previous research (Naito, Hendricks, & Sause, 2018b). This interface shear connection model provides elastic resistance to relative longitudinal displacement between the deck and the steel tee sections. At the locations of these interface shear connection elements, a rigid constraint was specified for the other relative displacements to prevent relative displacement in the vertical and transverse directions of the bridge. For Model 1, Model 2, and Model 3 (shell element models), at each interface shear connection element location, the corresponding deck node and steel tee section web node are offset from each other by 0.750 in. in the longitudinal direction to provide a finite distance between the corresponding nodes. A schematic of a linear-elastic link element is shown in the left image of Figure 78, while the right image shows a close-up view of a link element in the finite element model.

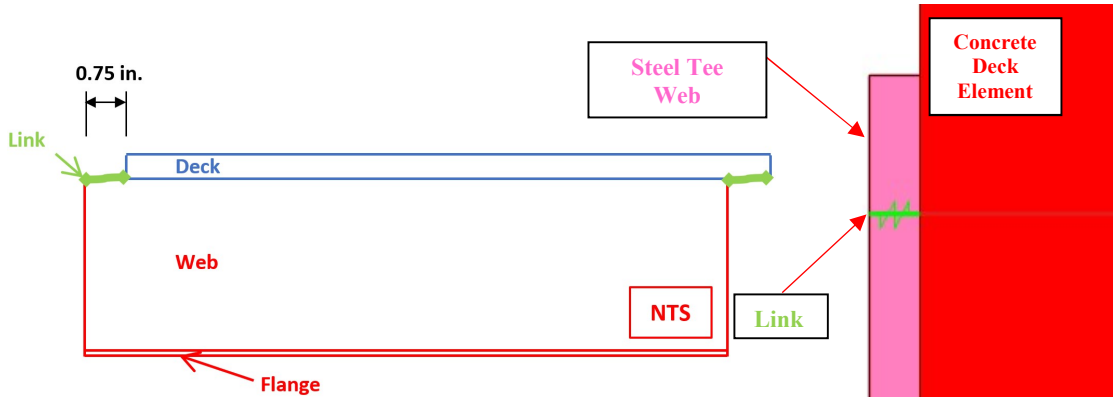

Figure 78. Interface shear connection element with corresponding deck and tee section web nodes (for shell element models).

For Model 4 and Model 5 (solid element models), at each interface shear connection element location, the linear-elastic link element connects to coinciding nodes in the finite element mesh for the deck and the finite element mesh for the tee section web (i.e., the nodes have the same coordinates and the link element has zero length) and there is no longitudinal offset.

All FEA models have similar element sizes, and the element sizes are similar to those used in previous research (Naito, Hendricks, & Sause, 2018b). In the longitudinal direction of the bridge, the element length was governed by the interface shear connection spacing. Starting at the bearings, the connections are spaced 4 in. (on-center) for the first 8 ft-8 in. (resulting in 4 in. long elements), followed by 8 in. for the next 5 ft-4 in. (resulting in 8 in. long elements), and then 12 in. for the next 2 ft up to the mid-span. To maintain reasonable element aspect ratios, the 12 in. spacing was divided in half to create 6 in. long elements. The element meshes are symmetric about the bridge mid-span. Element lengths in the transverse direction of the bridge were less constrained and are based on locations requiring coinciding nodes for connecting the bridge components (e.g., the location of the interface between the steel tee section webs and deck). Element aspect ratios are less than 6:1.

An important difference between the shell element models (Model 1, Model 2, and Model 3) and the solid element models (Model 4 and Model 5) is the model for the end diaphragms. The shell element models have end diaphragms that are modeled as single plates directly attached to the steel tee webs, and aligned with the centerline of the bearings. This model of the end diaphragms with shell elements does not adequately represent the torsional stiffness of the concrete end diaphragms of the bridge, which can restrain the (in-plane) end rotations of the composite steel tee sections (into the span). Model 4, with solid elements, was developed to enable a more accurate model of the end diaphragms to be included in the FEA. Figure 79 compares the shell element and solid element models of the end diaphragms. Figure 80 shows that the solid element models also include stiffeners (shown in green) attached to the steel tee sections at the bearings.

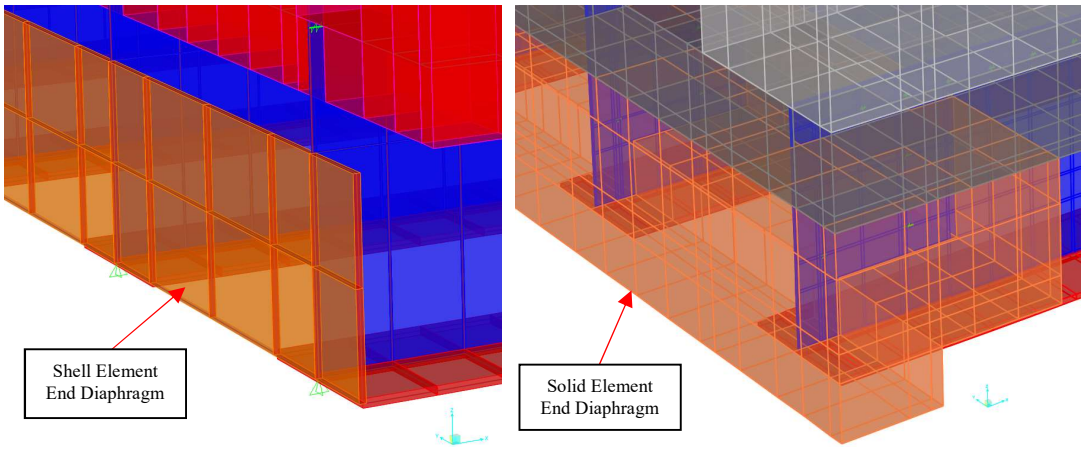

Figure 79. End diaphragm models: (left) shell element model; (right) solid element model.

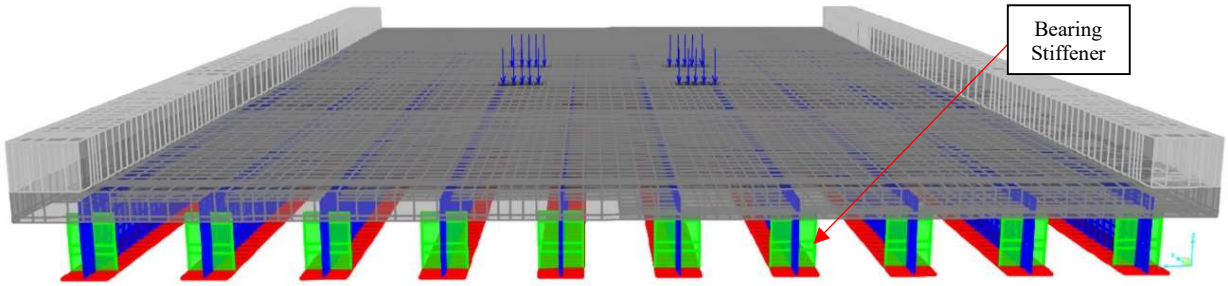

Figure 80. Model 4 (with solid elements) shown with end diaphragm elements removed to show bearing stiffeners.

Table 5. Summary of FEA Models.

Model Name	Pre-test or Post-test	Element Type	Description
Model 1	Pre-test	Shell	Simplified model with pin and roller supports
Model 2	Pre-test		Extension of Model 1 with parapets
Model 3	Pre-test		Extension of Model 2 with spring supports
Model 4	Pre-test	Solid	Includes parapets, end diaphragms, and bearing stiffeners and pads
Model 5	Post-test		Extension of Model 4 with subbase/backfill against end diaphragms

4.4. Pre-Test Analyses

The pre-test FEA used models of increasing complexity, as described earlier. As previously noted, the instrumentation of the bridge was planned using results from the most complex of these model (Model 4). The presentation of the FEA results starts with results from the simplest FEA model. Before the FEA results

are given, results from a conventional line-girder analysis (often used in bridge design and assessment) are presented. The line-girder analysis uses a transformed-section to model the composite steel tee section of the Flex Beam units, along with vehicular load distribution factors. The NTT is used to model vehicular load on the bridge.

4.4.1. Line-Girder Analysis

The line-girder analysis is based on a transformed-section model of a Flex Beam half-unit, and provides initial results for comparison with FEA results. A Flex Beam half-unit is half of a standard Flex Beam modular unit that has two inverted steel tee sections with the associated concrete deck, shown in Figure 81.

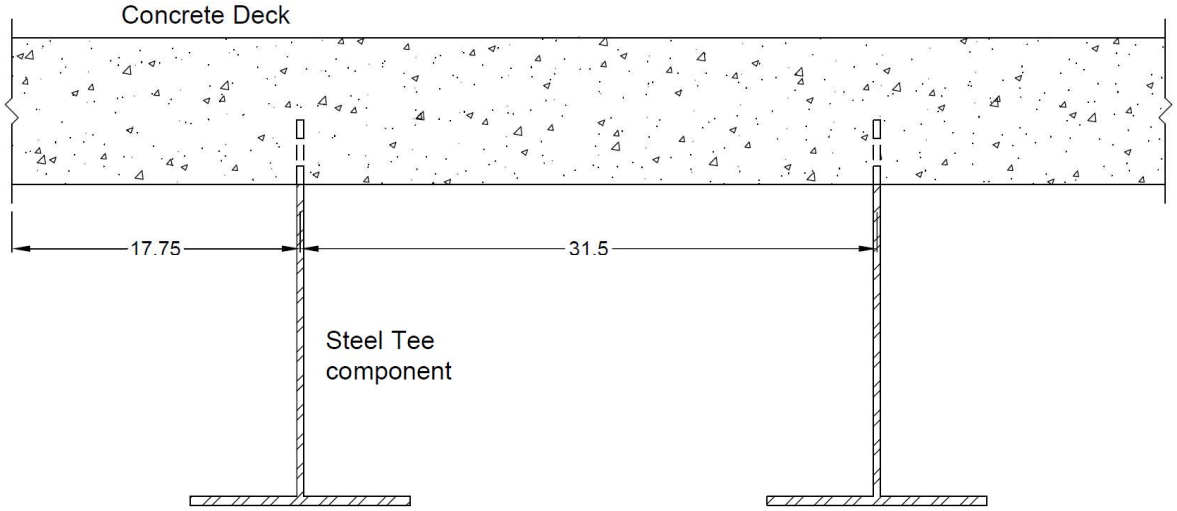

Figure 81. Flex Beam modular unit composed of two inverted steel tee components.

Using the plane-section assumption of beam theory and elastic material properties, the Flex Beam half-unit cross-section was represented as a transformed section (see Figure 82) and analyzed as a simple beam. The transformed section is based on elastic modulus values for concrete (E_c) and steel (E_s), which are 3,625 ksi and 29,000 ksi, respectively, resulting in transformation factor, n, of 8. Correspondingly, the concrete deck width is reduced from 31.5 in. to transformed steel section width of 3.9375 in. (see Figure 82).

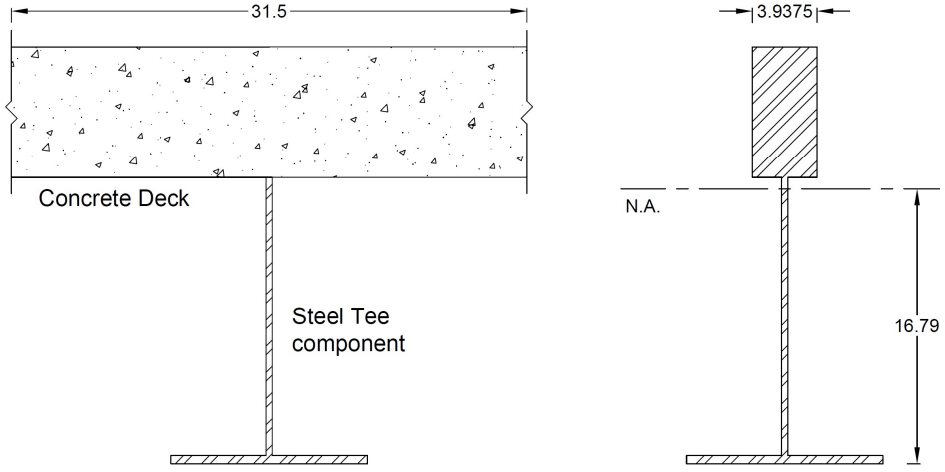

Figure 82. Transformed-section model of Flex Beam half-unit: (Left) half-unit; (Right) transformed section.

Conventional live (vehicular) load distributions factors are used to distribute a portion of the total NTT load to a single Flex Beam half-unit. The load distribution factors are for the single-lane-loaded condition, with the standard multiple presence factor of 1.2 for the single-lane-loaded case removed, since the distribution

factors are being applied to a known test truck. These load distribution factors are based on previous research (Naito, Hendricks, & Sause, 2018a) and are 0.25 for flexure (i.e., the assumed factor of 0.3 divided by 1.2) and 0.39 for shear (i.e., the factor for shear in interior beams from DM-4 is 0.36 + S/25 divided by 1.2) (Design Manual, Part 4 (DM-4), 2019). For the line-girder analysis, the NTT is applied to the bridge in two separate longitudinal positions. For a large moment case, the tandem axle is centered on the span, and the front axle is off the bridge (see Figure 83a). For a large shear case, the NTT is centered on the span (see Figure 83b). The large shear case is analogous to Longitudinal Position 1 and the large moment case is analogous to Longitudinal Position 3.

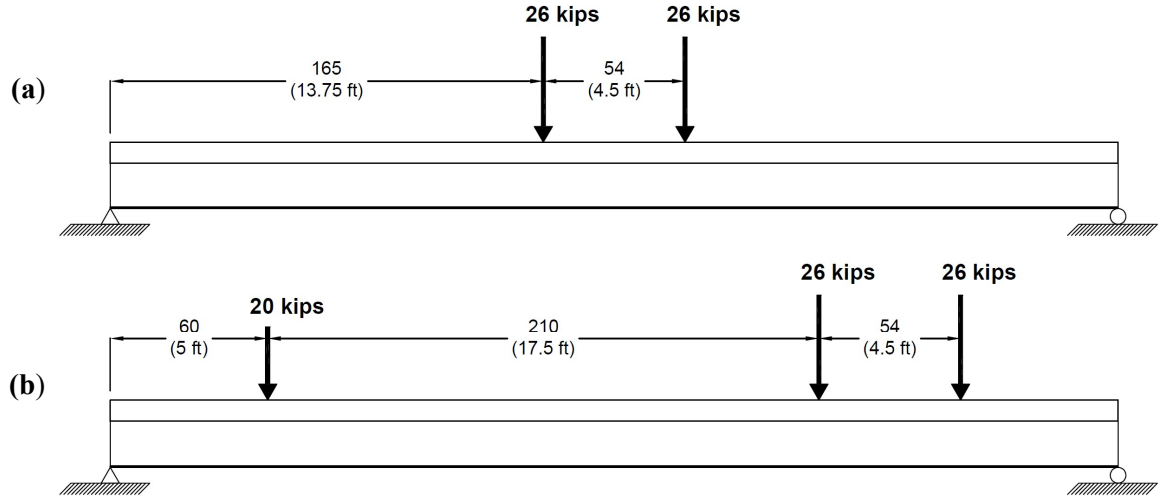

Figure 83. Longitudinal positions of NTT used in line-girder analysis. (a) large moment case and (b) large shear case.

Structural analysis with the load distribution factors applied to the results for maximum moment and shear, provided the stress at locations of interest. For the large moment case, the maximum flexural stress was 5.90 ksi (at mid-span at the bottom of the flange), and for the large shear case, the maximum shear stress was 2.71 ksi (at the support nearest to the tandem axle). These values will be compared to results from FEA (SAP2000) of a Flex Beam half-unit modeled similar to Model 1 (using shell elements for modeling of the composite steel tee section, link elements for interface shear connections, and simple supports for the bearings) to assess the line-girder analysis approach. FEA of the Flex Beam half-unit under the NTT positioned as shown in Figure 83, with the distribution factors (0.25 for flexure and 0.36 for shear) applied, provides results consistent with the line-girder analysis (see Figure 84). For the large moment case, FEA provided a maximum stress at the mid-span flange bottom of 5.91 ksi, and for the large shear case, FEA provided a maximum shear stress (in the web) near the support closest to the tandem axle of 2.94 ksi.

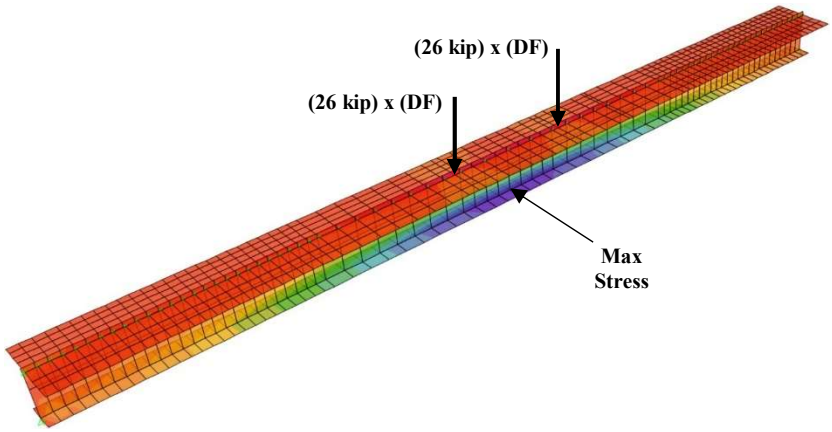

Figure 84. FEA of Flex Beam half unit with load distribution factor applied for large moment case.

Table 6 summarizes the results of the line-girder analysis.

Table 6. Maximum flange bottom flexural stress for large moment load case and maximum web shear stress for large shear load case from line-girder transformed-section analysis and FEA results.

Load Case	Line-Girder Transformed-Section Analysis (ksi)	FEA (ksi)
Large Moment	5.90	5.91
Large Shear	2.71	2.94

The large moment and large shear load cases are not the longitudinal positions of the NTT that would produce the theoretical maximum moment and theoretical maximum shear on the Flex Beam half-unit. The bending stress from the large moment case, Longitudinal Position 3, with the tandem axle centered at mid-span produces a bending moment stress (5.899 ksi) that is essentially equal to the theoretical maximum bending moment stress (5.900 ksi) for one axle of the tandem axle centered at mid-span. The shear stress from the large shear case, Longitudinal Position 1, with the truck centered at mid-span (2.71 ksi) is 21% less than the theoretical maximum shear stress (3.41 ksi), which occurs with the 2nd axle of the tandem axle centered on the bearing (and the rest of the truck axles on the bridge, Longitudinal Position 2B). The advantage of using the large shear case (Longitudinal Position 1), instead of the theoretical maximum shear case for these comparisons, is that the axle nearest to the bearing with the largest reaction, is located away from the bearing in the large shear case (Longitudinal Position 1), so that rational FEA shear stresses can be determined. When an axle is too close to the bearing, or located over the bearing, there is no shear span, and FEA shear stresses cannot be determined.

4.4.2. Effects of Modeling Approaches on FEA Results

Four FEA models, along with the line-girder analysis, were used in the pre-test analyses. The FEA models were described earlier. Figure 85, Figure 86, Figure 87, and Figure 88, respectively, present flange bottom stresses with the test truck tandem centered in the westbound lane (Transverse Position 2) and at mid-span (Longitudinal Position 3) for Model 1, Model 2, Model 3, and Model 4, respectively.

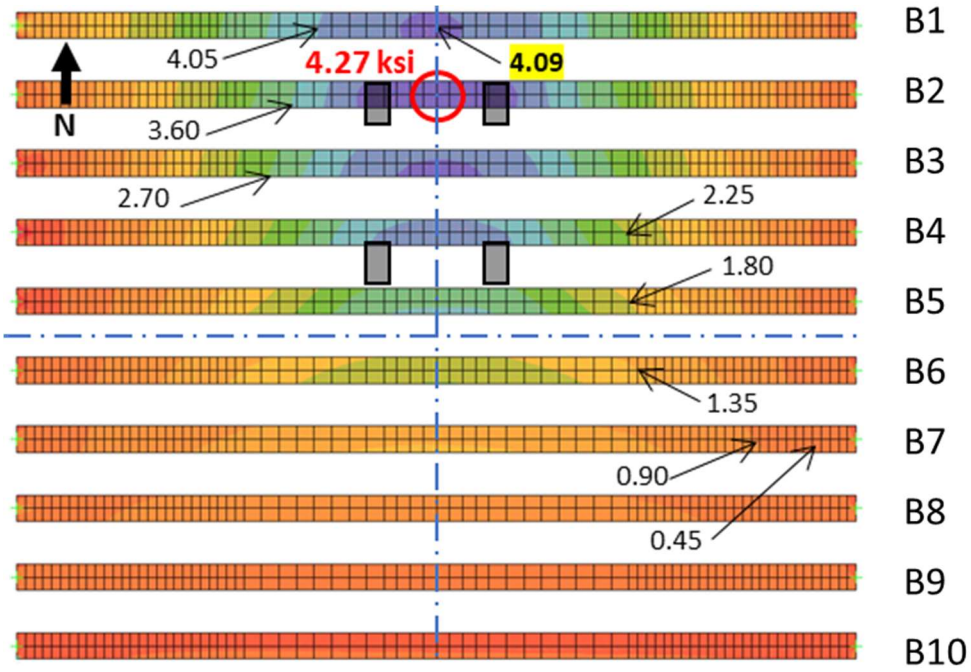

Figure 85. Flange bottom longitudinal stresses from Model 1 (Transverse Position 2, Longitudinal Position 3).

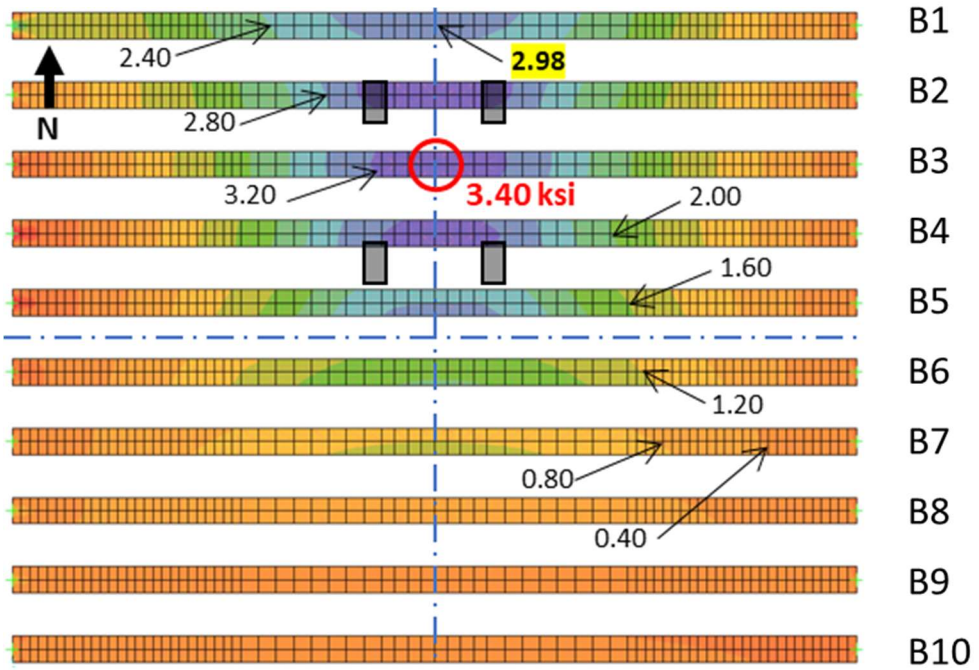

Figure 86. Flange bottom longitudinal stresses from Model 2 (Transverse Position 2, Longitudinal Position 3).

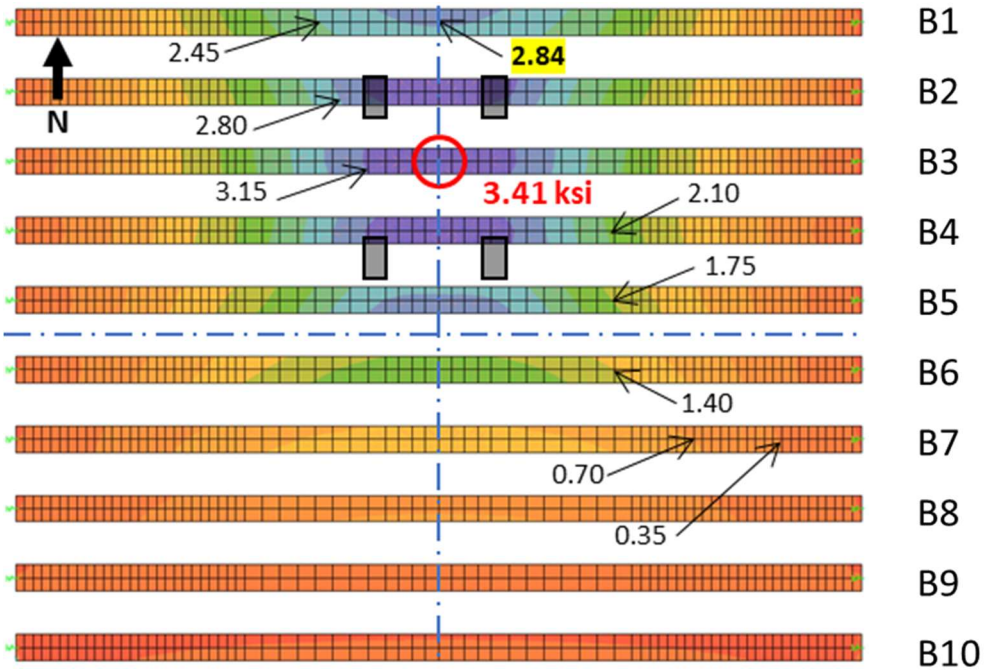

Figure 87. Flange bottom longitudinal stresses from Model 3 (Transverse Position 2, Longitudinal Position 3).

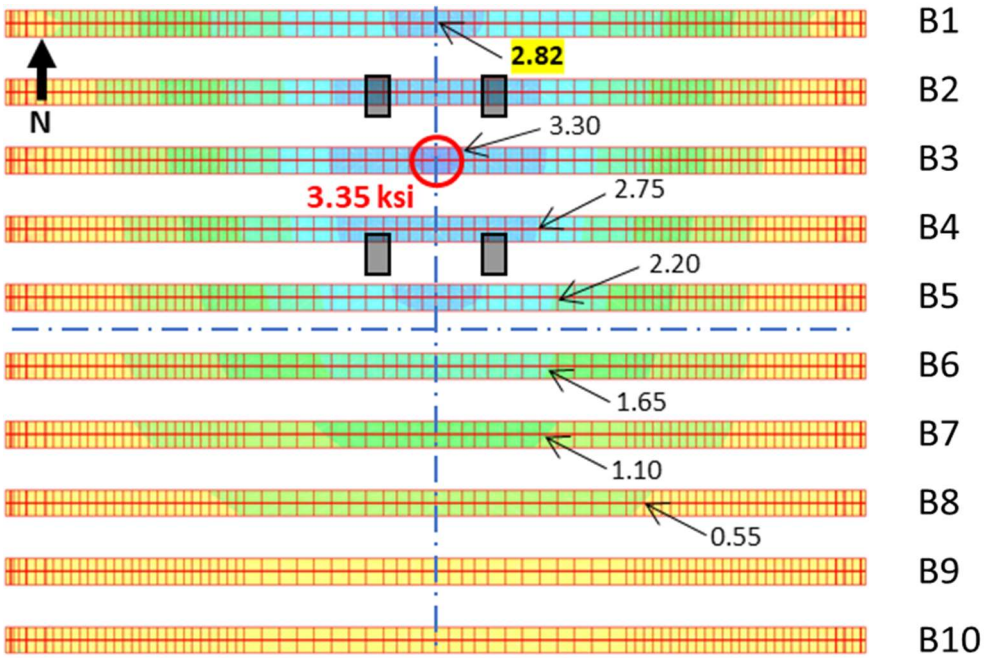

Figure 88. Flange bottom longitudinal stresses from Model 4 (Transverse Position 2, Longitudinal Position 3).

Figure 85 shows the flange bottom longitudinal stress results from Model 1 with a relatively large maximum stress on the flange of the exterior steel tee section, B1 equal to 4.09 ksi, and a maximum flange stress in B2 of 4.27 ksi. Figure 86 shows the flange bottom stress results from Model 2, where the stress on B1 decreased 37% to 2.98 ksi by adding the parapets (modeled with shell elements) to the FEA model. Also, the maximum flange stress decreased to 3.40 ksi, and the maximum stress is on the flange bottom of B3 instead of B2. Figure 87 shows the results from Model 3, which has a more realistic model of the bearings, using springs to model the bearing pads (instead of pin and roller supports), and only small changes in the flange bottom stresses, relative to the results from Model 2, are observed. Figure 88 shows the results from Model 4, based on solid elements with a more realistic model for the concrete end diaphragms. The maximum flange bottom stress on B3 from Model 4 is decreased by about 2% from the flange bottom stress from Model 2 and Model 3.

One unusual aspect of the results from Model 1 is the negative (reverse) bending that occurs in the exterior composite steel tee section on the opposite side of the bridge when the truck is positioned with the centroid of (rear tandem axle) wheels at 2 ft. from the parapet (i.e., roadway edge) in Transverse Position 3. Without the parapets in the model, Model 1 has a two-way plate bending behavior, which is restrained by the bearings. For example, when the truck is in the westbound lane, the expected positive bending behavior occurs in composite steel tee sections B1, B2, B3, B4, B5 and B6; however, reverse bending occurs in B10. In this example, the two-way bending of the bridge (in Model 1) causes the concrete deck to pull up on B10 within the span, and the bearings of B10 restrain the uplift causing end shears that pull it down, resulting in negative bending of B10. Figure 89 shows the longitudinal stress on the flange bottom of B10 from this reverse bending, where the dark regions in the image are areas of compressive stress over the entire span of B10. Adding the parapets to Model 2 and Model 3 decreases this reverse bending, and Figure 90 shows that reverse bending over the length of B10 is completely eliminated in Model 4 (compressive stresses are shown in grey). The compressive stress shown at the ends of the tee section of Model 4 are artificial localized effects from the area springs used to model the bearing pads.

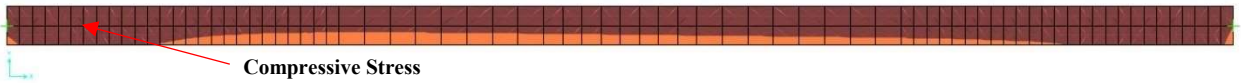

Figure 89. Flange bottom longitudinal stresses in B10 from Model 1 (Transverse Position 2, Longitudinal Position 3).

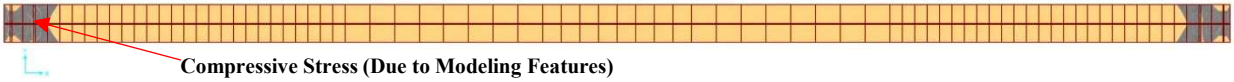

Figure 90. Flange bottom longitudinal stresses in B10 from Model 4 (Transverse Position 2, Longitudinal Position 3).

As discussed previously, the torsional stiffness of the concrete end diaphragms (included in Model 4) causes some negative (reverse) bending moment in the composite steel tee sections near the bearings. Figure 91 shows reverse bending near the bearings of the steel tee sections near the longitudinal centerline of the bridge when the truck is at Transverse Position 1 and Longitudinal Position 3 (compressive stress is shown in grey).

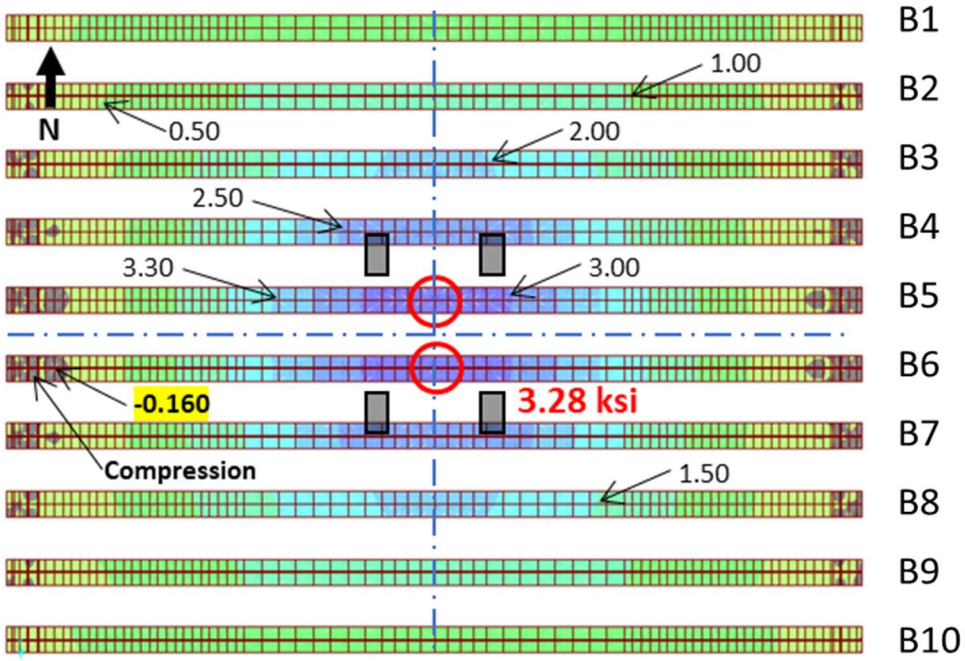

Figure 91. Flange bottom longitudinal stresses from Model 4 (Transverse Position 1, Longitudinal Position 3).

As shown in Figure 91, FEA of Model 4 provides a compressive flange bottom stress of -0.160 ksi near the west bearing at mid-width of the bridge (and this location was instrumented to measure reverse bending). This reverse bending near the bearings is an effect of the torsional stiffness of the end diaphragms, which is not properly modeled in Model 1, Model 2, or Model 3 (the shell element models). Therefore, the reverse bending is not observed in the results from Model 3 shown in Figure 92, which shows that FEA of Model 3 provides a tensile flange bottom stress of 0.280 ksi near the west bearing at mid-width of the bridge.

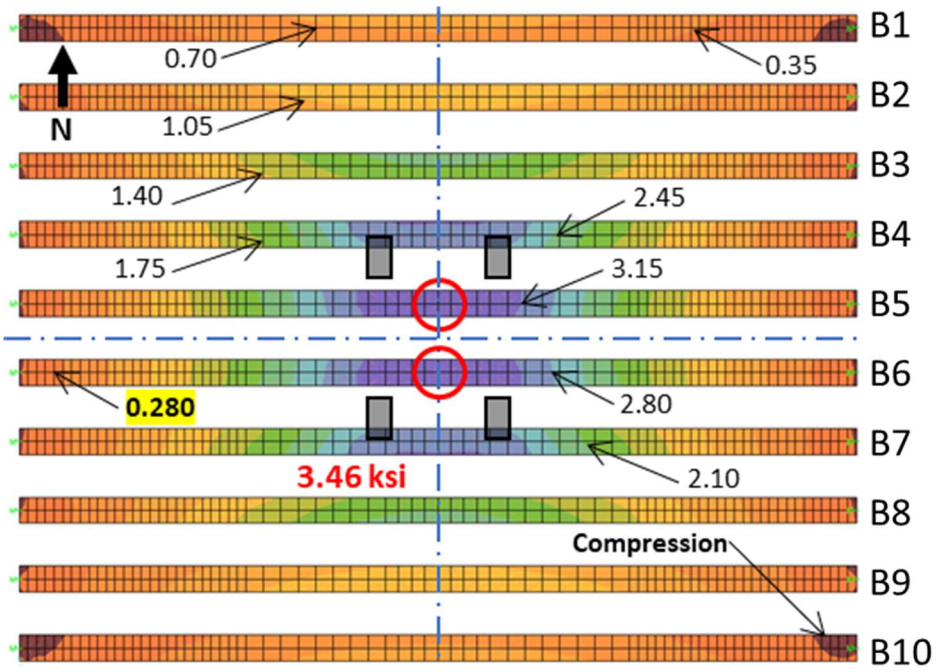

Figure 92. Flange bottom longitudinal stresses from Model 3 (Transverse Position 1, Longitudinal Position 3).

4.5. Post-Test Analyses

In the post-test analyses the ATT weights and dimensions (measured immediately before controlled-load testing) were used as input for the analyses (see Figure 8). For the purpose of validating the analysis models, the test truck positions used in the pre-test analyses and during controlled-load testing park tests were also used in the post-test analyses. To assess the accuracy of the post-test FEA models, strains measured during the controlled-load testing were compared with results from the FEA, and the post-test FEA models were ultimately calibrated using results from the controlled-load testing.

4.5.1. Comparison of Results from FEA Model 4 and Controlled-Load Testing

The static responses of the bridge from the controlled-load testing park tests, were compared to results from FEA of Model 4 using the ATT for loading. The results for three park tests are compared, namely Test 16, Test 17, and Test 18, which have the ATT positioned at three transverse positions, mid-width, mid-lane, and 2 ft from the parapet, respectively (see Table 7). For these park tests, the ATT is centered on the bridge longitudinally (Longitudinal Position 1).

Table 7. Park tests from controlled-load testing of bridge used in comparison with FEA results.

Test No.	Test Truck Direction of Travel	Test Type	Transverse Position	Longitudinal Position
16	Westbound	Park	(**1**) Mid-Width	(**1**) Truck Centered in Span
17	Westbound	Park	(**2**) Mid-Lane	(**1**) Truck Centered in Span
18	Westbound	Park	(**3**) 2 ft from Parapet	(**1**) Truck Centered in Span

The stress results from controlled-load testing and FEA (Model 4) are compared in Table 8. The comparison shows that Model 4 provides results that tend to be larger (i.e., conservative) compared to the measured static response of the bridge from the park tests.

Table 8. Comparison of results measured in controlled-load testing and results from FEA of Model 4.[1]

Channel Name	Test 16		Test 17		Test 18	
	Measured	FEA Model 4	Measured	FEA Model 4	Measured	FEA Model 4
B2_W_SG1	0.17	0.24	0.15	0.20	0.16	0.23
B2_QRT_SG1	0.58	0.80	0.99	1.39	0.91	1.47
B1_CL_SG1	0.58	0.84	1.41	2.10	1.65	2.27
B2_CL_SG1	0.82	1.13	1.41	1.92	1.51	2.06
B2_CL_SG2	0.04	0.00	0.14	0.04	0.14	0.04
B2_CL_SG3	0.18	0.05	0.31	0.28	0.29	0.31
B2_CL_SG4	0.43	0.55	0.79	1.04	0.85	1.11
DK_2_3_SG2	0.01	0.01	0.03	0.03	0.03	0.04
B3_CL_SG1	1.04	1.40	1.44	1.90	1.55	1.96
B4_CL_SG1	1.23	1.53	1.42	1.73	1.37	1.67
B4_CL_SG2	0.02	0.02	0.03	0.03	0.03	0.02
B4_CL_SG3	0.08	0.10	0.06	0.16	0.08	0.16
B5_QRT_SG1	0.91	1.19	0.74	1.06	0.69	1.03
B5_W_SG1	0.02	0.07	0.02	0.10	0.00	0.13
B5_W_SG2	-0.02	-0.02	-0.02	-0.02	-0.02	-0.02
B5_W_SG3	0.06	0.18	0.07	0.18	0.06	0.15
DK_4_5_SG2	-0.01	0.02	0.00	0.02	0.00	0.02
DK_4_5_SG5	0.04	0.14	0.03	0.10	0.02	0.08
B5_CL_SG1	1.40	1.74	1.23	1.47	1.16	1.43
B5_CL_SG3	0.14	0.12	0.20	0.09	0.14	0.08
B5_CL_SG4	0.63	0.87	0.49	0.73	0.53	0.70
B6_W_SG1	0.01	0.08	0.13	0.16	0.17	0.18
DK_5_6_SG2	-0.01	0.03	0.00	0.01	0.01	0.00
B5_E_SG1	0.10	0.24	0.06	0.24	0.12	0.28
B5_E_SG2	-0.02	-0.04	-0.02	-0.03	-0.01	-0.03
B5_E_SG3	0.27	0.31	0.22	0.23	0.21	0.20
B6_CL_SG1	1.35	1.74	0.96	1.26	0.92	1.17
B8_CL_SG1	0.99	1.32	0.47	0.60	0.35	0.51
B9_CL_SG1	0.73	1.03	0.27	0.33	0.18	0.27
B2_W_DISP	0.00	-0.05	0.32	-0.18	0.33	-0.17
B2_QRT_DISP	0.01	-0.06	0.01	-0.05	0.01	-0.06
B5_W_DISP	0.25	-0.14	0.34	-0.14	0.32	-0.12
B5_QRT_DISP	0.04	-0.06	0.05	-0.03	0.07	-0.04
B5_CL_DISP	0.40	-0.25	0.32	-0.17	0.25	-0.15
B5_E_DISP	-0.58	0.30	-0.53	0.23	-0.49	0.19

[1] *Stress in ksi and Displacement in Inches*

"E": East
"W": West
"CL": Centerline of Span
"QTR": Quarter Point of Span
"B#": Beam Designation
"SG": Strain Gauge
"DISP": Displacement Sensor
"DK": Deck

The FEA results for the mid-span flange bottom stresses are compared with the measured static response of the bridge from the three park tests on the left image of Figure 93, Figure 94, and Figure 95, where the FEA results are shown in black and the measured results are shown in red (the images on the right, the mid-span flange bottom stresses for Model 5, are discussed later). The results from FEA of Model 4 are as expected with the largest stresses occurring in the steel tee sections closest (transversely) to the truck (i.e., the most heavily loaded composite steel tee sections); the stresses are smaller for the steel tee sections away

from the truck. The same pattern of mid-span flange bottom stresses is observed in the measured park test results.

In the Model 4 FEA results in Figure 93, Figure 94, and Figure 95 (left images), the influence of the actual test truck (ATT) having unequal wheel loads between the LHS and RHS is observed in results from both the FEA and park tests. The truck is positioned mid-width (Transverse Position 1), but notably larger stresses are observed on the north half of the bridge, since the truck is westbound and the RHS wheel loads of the ATT are larger than the LHS wheel loads. The location of maximum mid-span stress is a single location in the north half of the bridge on composite steel tee section B5.

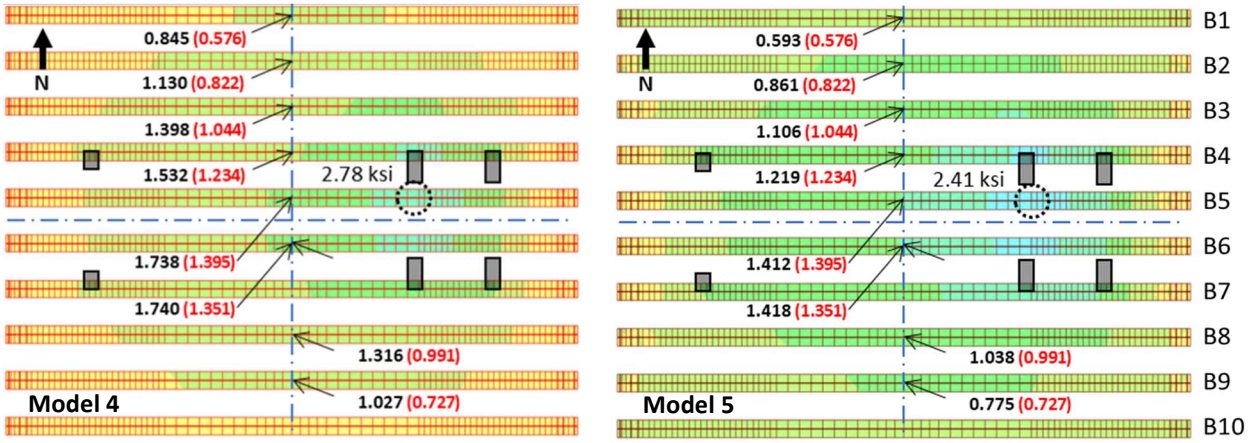

Figure 93. Flange bottom longitudinal stresses from Test 16 (Transverse Position 1, Longitudinal Position 1). Left: Model 4. Right: Model 5. FEA results in black; test results in red in parentheses.

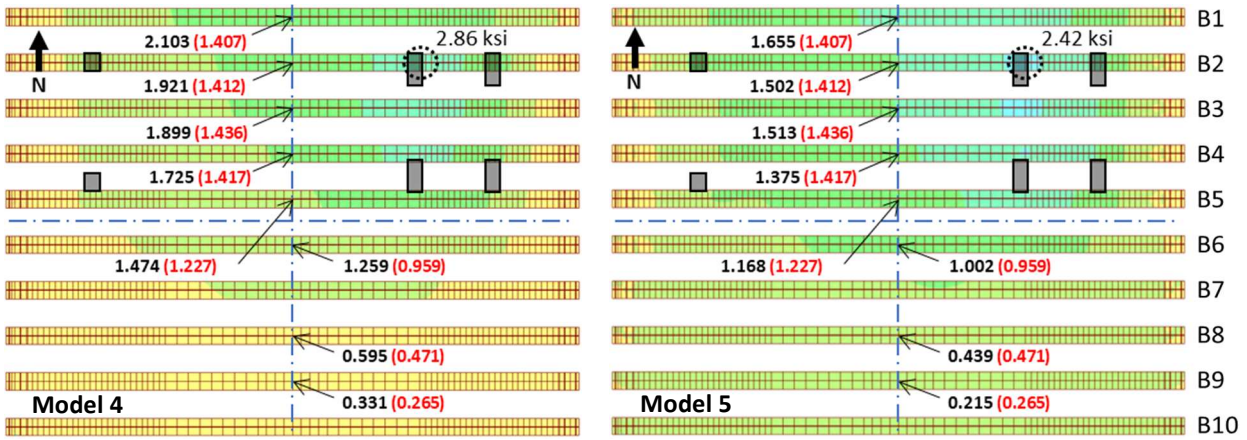

Figure 94. Flange bottom longitudinal stresses from Test 17 (Transverse Position 2, Longitudinal Position 1). Left: Model 4. Right: Model 5. FEA results in black; test results in red in parentheses.

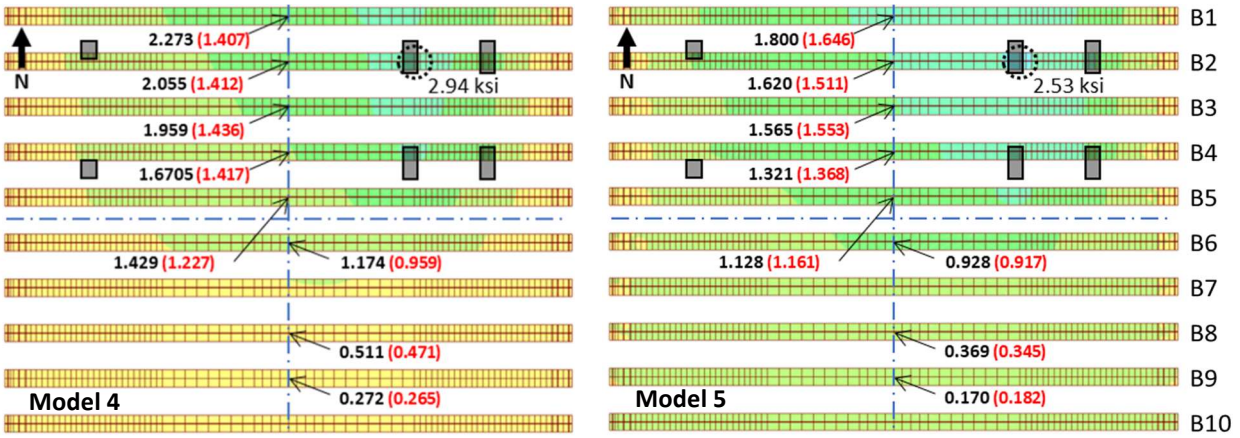

Figure 95. Flange bottom longitudinal stresses from Test 18 (Transverse Position 3, Longitudinal Position 1). Left: Model 4. Right: Model 5. FEA results in black; test results in red in parentheses.

In general, the comparison of mid-span flange bottom stress results from FEA of Model 4 and the controlled-load testing results show the Model 4 results are significantly larger than the test results. Keeping in mind that the largest flange bottom stresses tended to decrease as the FEA models were improved, it is noteworthy that the most accurate of the FEA models considered in the pre-test analyses does not accurately represent the stress response of the bridge, however, all the FEA results (for mid-span flange bottom stresses) are conservative (i.e., greater than observed in the controlled-load park tests.

Model 4 also captures the interactions of the concrete deck, end diaphragm, and steel tee sections that were observed in the park test results. Figure 96 shows the top and bottom surfaces of the deck with the truck mid-width (Transverse Position 1) and the tandem axle centered on the bridge (Longitudinal Position 3). It can be seen that the concrete deck is in positive bending (i.e., compressive stress on top and tensile stress on bottom) over most of the span and with negative bending near the bearings.

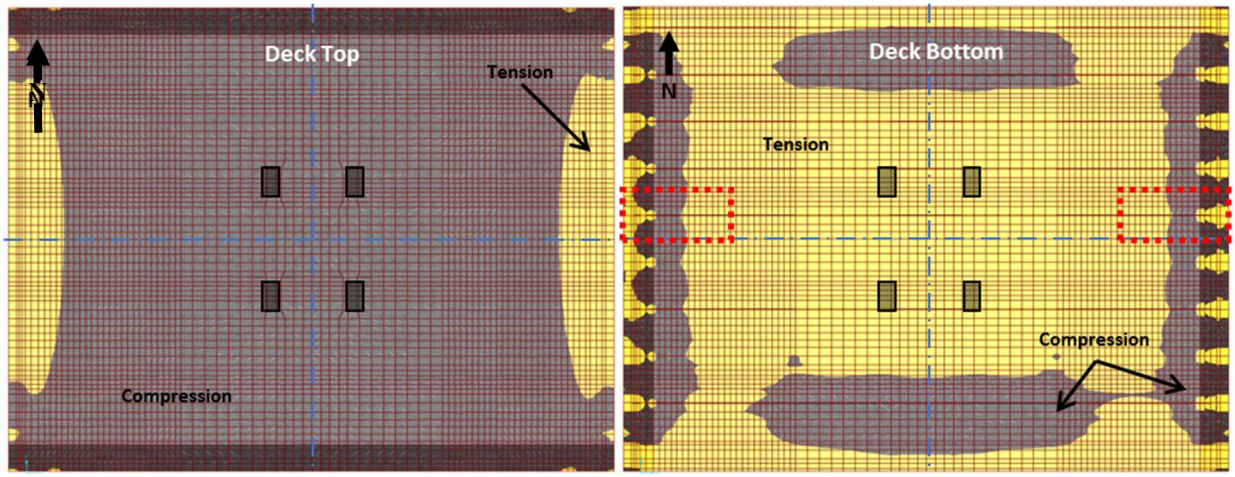

Figure 96. Concrete deck longitudinal stresses. Left: Deck top, and Right: Deck bottom. (Grey denotes regions of compressive stress).

Similar results are seen in the cross-section of views of the deck and end diaphragm at B5 in the top image of Figure 97 and Figure 98. The locations of these cross-sections are shown by the red dashed boxes on the right image of Figure 96. These cross-section images show a complex pattern of stress at the location where the deck meets the end diaphragm. At the corner where the deck meets the end diaphragm (and in the deck above this location), the deck is in negative bending. On the bottom surface of the deck, compressive strains (and corresponding stresses) were measured during the park test (as shown in the figures, where FEA stress results are in black text and measured stress results from the test are in red text in parentheses).

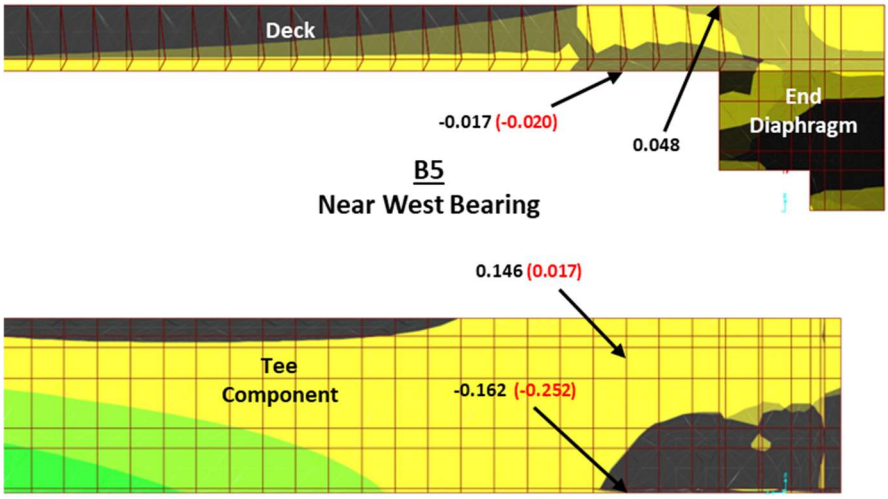

Figure 97. Cross-section view of concrete deck, end diaphragm, and steel tee section of B5 near west bearing. FEA results in black; test results in red in parentheses.

However, for the steel tee components (which are shown in the bottom images of Figure 97 and Figure 98), at the location were the deck meets the end diaphragm, tensile stress is observed on the web while compressive stress is observed on the flange bottom. A similar stress distribution was measured in the bridge during the controlled-load testing. As mentioned in Chapter 3 in the discussion of the controlled-load testing results, near the location where the deck meets the end diaphragm, or, more generally, at locations near the bearings, the plane-section assumption is no longer valid.

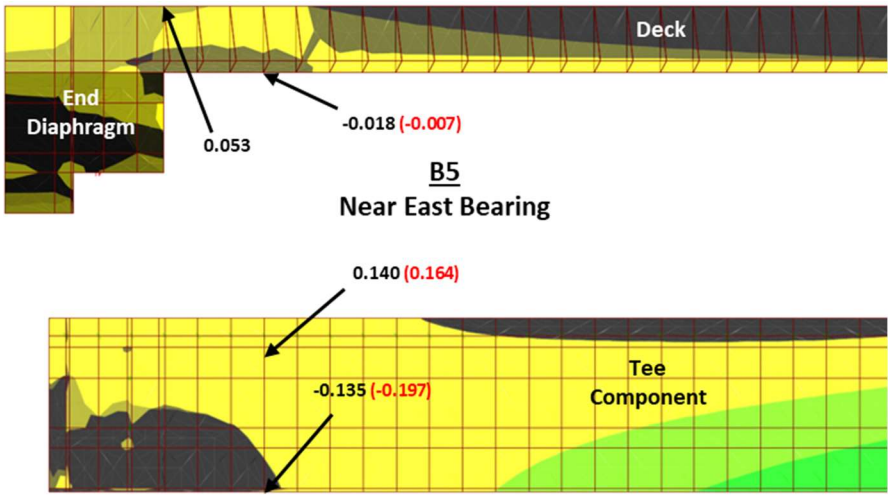

Figure 98. Cross-section view of concrete deck, end diaphragm, and steel tee section of B5 near east bearing. FEA results in black; test results in red in parentheses.

Figure 97 and Figure 98 show that the top of the concrete deck near the bearings (and above the location where the deck meets the end diaphragm) is in tension (when the test truck is mid-width, Transverse Position 1, with the tandem axle centered on the bridge, Longitudinal Position 3, i.e., as in park Test 19). The maximum tensile stress on the top of the concrete deck from FEA of Model 4 is approximately 50 psi as shown in Figure 97 and Figure 98. Tension is also observed on the bottom of the deck near mid-span, where the maximum tensile stress from FEA of Model 4 is approximately 25 psi. Note that the maximum tensile stress on the top of the concrete deck near the bearings from FEA of Model 5 (discussed later) is approximately 70 psi. Comparing these values to the theoretical concrete cracking stress of approximately 500 psi shows that cracking is not expected from these tensile stresses.

The FEA results compared to controlled-load testing results, provide verification that the Model 4 model (solid elements, with bearing pad modeled as support springs, and with parapets, end diaphragms, and bearing stiffener plates included in the model) is a more accurate model than Model 1, Model 2, or Model 3. Model 4 is the model that most accurately captures the measured response of the bridge, among the models considered in the pre-test analyses. An improved model, however, denoted Model 5 and described in the next subsection, is a final, calibrated FEA model that includes a model of the pressure from the roadway subbase and backfill on the concrete end diaphragms at the abutments of the bridge.

4.5.2. Final FEA Model and FEA Results

Features of the Flex Beam demonstration bridge that were not included in FEA Model 4 are the details at the "semi-integral" abutments of the bridge. Figure 99 shows that the west bearing is "fixed" and the east bearing is an "expansion" bearing. The design drawings show that at the "fixed" bearing, 1 in. diameter anchor bolts pass through 1 13/16 in. diameter holes in the sole plates, and at the "expansion" bearings 1 in. diameter anchor bolts pass through (longitudinally) slotted holes in the sole plates. As a result of these oversized holes, the effects of the anchor bolts were not considered in Model 5 (i.e., the final FEA model), and the bearings were modeled using springs for the bearing pads, as in Model 4. Figure 99 and Figure 100 show the absence of an abutment "back wall" and show that the roadway subbase and backfill materials are in contact with the concrete end diaphragms creating semi-integral abutment conditions which restrain the movements of the end diaphragms. As discussed previously, the large concrete end diaphragms of the Flex Beam demonstration bridge restrain the end rotations of the more heavily loaded composite steel tee sections (near to the transverse position of the truck), and this end rotation restraint helps distribute the primary bending response of the bridge to the composite steel tee sections which are less heavily loaded (i.e., those at greater transverse distance from the truck position). This restraint from the end diaphragms alone is captured in Model 4. However, the roadway subbase and backfill material at the semi-integral abutments further restrain the end rotations of the more heavily loaded composite steel tee sections, and Model 5 includes this aspect of the bridge.

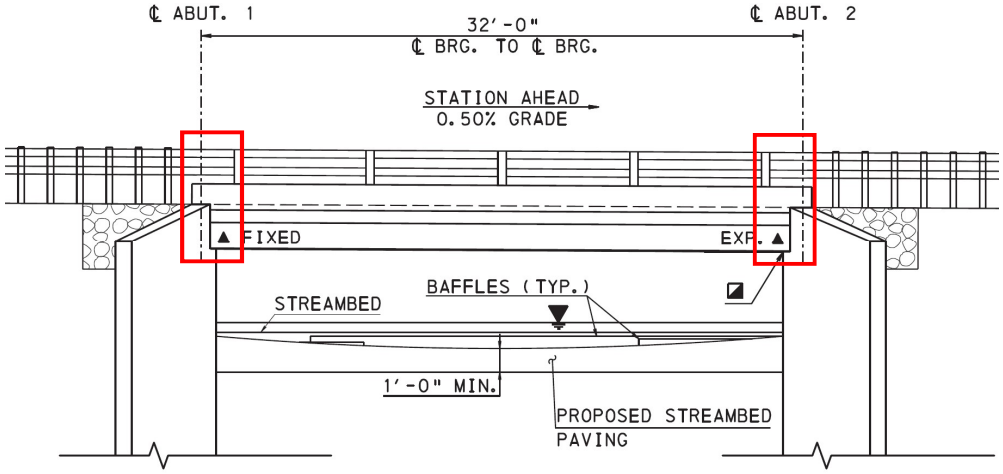

Figure 99. Side view of the Flex Beam (design drawing) and location of end diaphragm (PennDOT, 2020).

In Model 4, the rotations of the end diaphragms (about a transverse axis of the bridge) are restrained by their inherent torsional rigidity and the restraint from the composite steel tee sections to which they are connected. However, as shown in Figure 100, the roadway subbase and backfill can restrain the rotations of the end diaphragms. As the end diaphragms try to rotate and distribute load from the more heavily loaded composite steel tee sections to those that are less heavily loaded, pressure is mobilized in the roadway subbase and backfill that restricts the rotations of the end diaphragms.

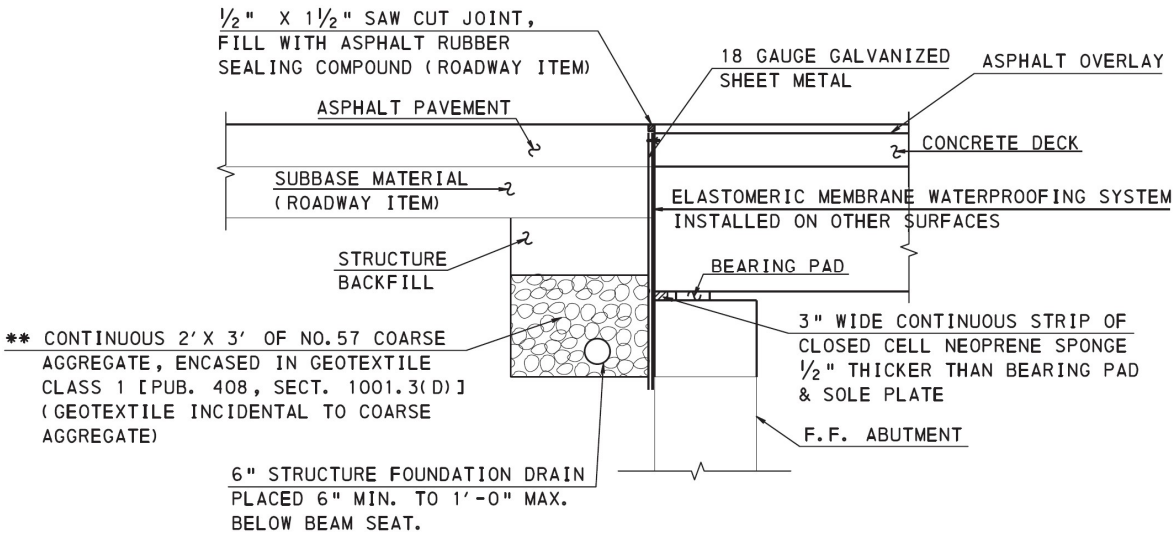

Figure 100. Roadway subbase and backfill in contact with bridge and end diaphragm (PennDOT, 2020).

FEA Model 5 includes "soil" springs to simulate the effects of pressure from the roadway subbase and backfill on the Flex Beam bridge end diaphragms. An initial value of the soil spring stiffness (k) was calculated using a formulation from the California Department of Transportation (Caltrans Seismic Design Criteria, 2013). This initial soil spring stiffness was $k = 0.0631$ kip/in.^{3} (stiffness per unit area). It is worth noting that the Caltrans formulation for soil stiffness at abutments is empirical and based on tests conducted on abutments with a specific depth (5 ft – 6 in.). In comparison, the depth of the end diaphragms in contact with the roadway subbase and backfill is relatively shallow (2 ft – 1½ in.). This calculated initial stiffness of 0.0631 kip/in.^{3} was a starting point for a sensitivity study in which the stiffness was incrementally increased. When the spring stiffness reached a value of 3 kip/in.^{3}, FEA results from Model 5 were similar to those measured during the controlled-load testing. More description of the stiffness sensitivity study is given later.

The image on the right of Figure 93 shows the flange bottom stress results for Model 5 with the ATT in Transverse Position 1, Longitudinal Position 1, where FEA stress values are in black text and measured stress results from the test are in red text in parentheses. Unlike the FEA results from Model 4 (left image in Figure 93), it is shown that Model 5 with soil springs to model pressure on the backside of the end diaphragms (with a soil spring stiffness $k = 3$ kip/in.^{3}), provides mid-span flange bottom stresses that are similar to those measured during controlled-load testing. Other test truck positions were used to provide further validation of Model 5. The images on the right side of Figure 94 and Figure 95 with results from Model 5 for Test 17 (Transverse Position 2, Longitudinal Position 1) and Test 18 (Transverse Position 3, and Longitudinal Position 1), respectively, show results similar to those in Figure 93 from Model 5, with mid-span flange bottom flexural stresses similar to the test results.

As mentioned before, a soil spring stiffness (k) sensitivity study was conducted to develop FEA Model 5 that represents the measured Flex Beam bridge response during controlled-load testing. Table 9 shows how the flange bottom longitudinal stresses at mid-span vary with the stiffness of the soil springs simulating the pressure of the roadway subbase and backfill for Test 19 (Transverse Position 1, Longitudinal Position 3), Test 20 (Transverse Position 2, Longitudinal Position 3), and Test 21 (Transverse Position 3, Longitudinal Position 3). For comparison, the measured mid-span flange bottom stresses are 1.11 and 3.07 ksi from Test 19 for steel tee sections B2 and B5, respectively; 2.62 and 2.29 ksi from Test 20 for B2 and B5, respectively; and 2.81 and 2.04 ksi from Test 21 for B2 and B5, respectively. The stiffness used for Model 5, $k = 3$ kip/in.^{3}, provides FEA stress results close to the measured controlled-load testing results.

Table 9. Flange bottom stresses at mid-span of B2 and B5 from FEA Model 5 as soil spring stiffness varies.

	Test 19		Test 20		Test 21	
Stiffness *k* (kip/in.^{3})	**B2 Stress (ksi)**	**B5 Stress (ksi)**	**B2 Stress (ksi)**	**B5 Stress (ksi)**	**B2 Stress (ksi)**	**B5 Stress (ksi)**
0	1.53	3.65	3.64	2.90	3.82	2.66
0.0631	1.52	3.64	3.63	2.89	3.81	2.65
0.5	1.46	3.57	3.53	2.82	3.71	2.58
1.0	1.40	3.49	3.44	2.75	3.61	2.51
1.5	1.35	3.43	3.35	2.69	3.52	2.45
2.0	1.30	3.37	3.28	2.64	3.44	2.39
2.5	1.26	3.32	3.21	2.59	3.37	2.35
3.0	1.22	3.27	3.15	2.54	3.31	2.31

Figure 101 shows flange bottom stresses for Test 16 (Transverse Position 1, Longitudinal Position 1) as the soil spring stiffness varies where FEA stress results are in black and measured stress results from Test 16 are in red. The results for soil spring stiffness values (a) $k = 0$ (i.e., the same as FEA Model 4), (b) $k = 0.0631$, (c) $k = 0.5$, (d) $k = 1$, (e) $k = 2$, and (f) $k = 3$ kip/in.^{3} are shown in Figure 101 (a), (b), (c), (d), (e), and (f), respectively. The results show that the flange bottom stress values from FEA across the bridge become closer to those from the test as the soil spring stiffness value approaches 3 kip/in.^{3}

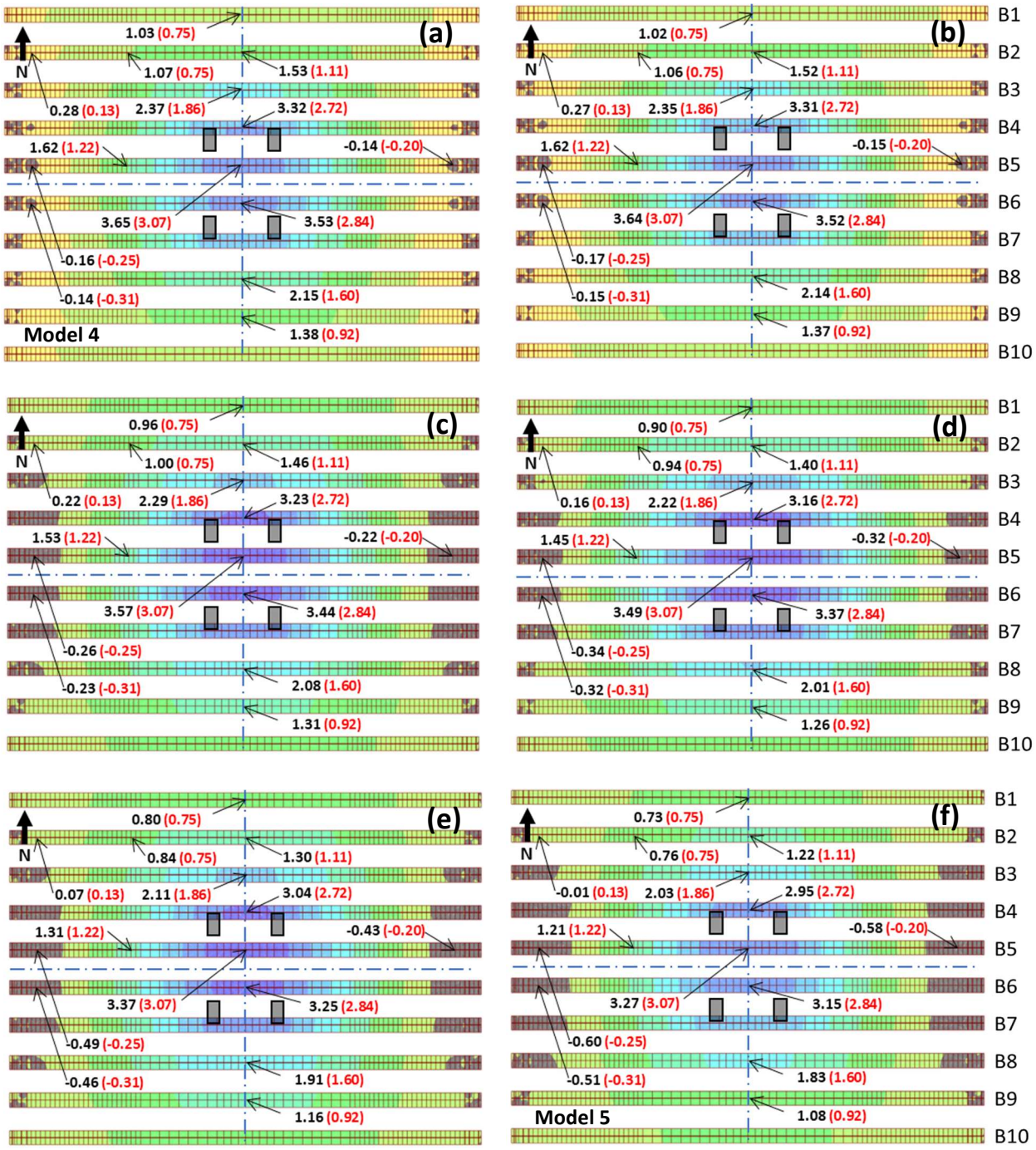

Figure 101. Flange bottom longitudinal stresses from Test 19 (Transverse Position 1, Longitudinal Position 3): (a) k = 0, (b) k = 0.0631, (c) k = 0.5, (d) k = 1, (e) k = 2, and (f) k = 3 kip/in.3. FEA results in black; test results in red in parentheses.

A full comparison of measured controlled-load testing results and FEA results for Model 5 for Test 16, Test 17, and Test 18 is presented in Table 10.

Table 10. Comparison of results measured in controlled-load testing and results from FEA of Model 5.[1]

Channel Name	Test 16		Test 17		Test 18	
	Measured	FEA Model 5	Measured	FEA Model 5	Measured	FEA Model 5
B2_W_SG1	0.17	0.01	0.15	-0.21	0.16	-0.20
B2_QRT_SG1	0.58	0.55	0.99	0.98	0.92	1.04
B1_CL_SG1	0.58	0.59	1.41	1.66	1.65	1.80
B2_CL_SG1	0.82	0.86	1.41	1.50	1.51	1.62
B2_CL_SG2	0.04	-0.01	0.14	0.02	0.14	0.02
B2_CL_SG3	0.19	-0.02	0.32	0.13	0.29	0.15
B2_CL_SG4	0.43	0.39	0.79	0.77	0.85	0.83
DK_2_3_SG2	0.01	0.00	0.03	0.02	0.03	0.02
B3_CL_SG1	1.04	1.11	1.44	1.51	1.55	1.57
B4_CL_SG1	1.23	1.22	1.42	1.38	1.37	1.32
B4_CL_SG2	0.02	0.01	0.03	0.01	0.03	0.01
B4_CL_SG3	0.08	0.02	0.06	0.56	0.08	0.05
B5_QRT_SG1	0.91	0.86	0.74	0.75	0.69	0.73
B5_W_SG1	0.02	-0.27	0.02	-0.21	0.00	-0.16
B5_W_SG2	-0.02	-0.03	-0.02	-0.03	-0.02	-0.03
B5_W_SG3	0.06	0.09	0.07	0.10	0.06	0.08
DK_4_5_SG2	-0.01	0.01	0.00	0.01	0.00	0.01
DK_4_5_SG5	0.04	0.13	0.03	0.09	0.02	0.07
B5_CL_SG1	1.40	1.41	1.23	1.17	1.16	1.13
B5_CL_SG3	0.14	0.03	0.20	0.00	0.14	0.00
B5_CL_SG4	0.63	0.68	0.49	0.55	0.53	0.53
B6_W_SG1	0.01	-0.26	0.13	-0.08	0.17	-0.05
DK_5_6_SG2	-0.01	0.02	0.00	0.00	0.01	0.00
B5_E_SG1	0.10	-0.19	0.06	-0.12	0.12	-0.06
B5_E_SG2	-0.02	-0.06	-0.02	-0.04	-0.01	-0.04
B5_E_SG3	0.27	0.23	0.22	0.15	0.21	0.11
B6_CL_SG1	1.35	1.42	0.96	1.00	0.92	0.93
B8_CL_SG1	0.99	1.04	0.47	0.44	0.35	0.37
B9_CL_SG1	0.73	0.78	0.27	0.22	0.18	0.17
B2_W_DISP	0.00	-0.05	0.33	-0.18	0.33	-0.18
B2_QRT_DISP	0.01	-0.06	0.01	-0.05	0.01	-0.06
B5_W_DISP	0.25	-0.14	0.34	-0.14	0.33	-0.12
B5_QRT_DISP	0.04	-0.06	0.05	-0.03	0.07	-0.04
B5_CL_DISP	0.40	-0.24	0.32	-0.16	0.25	-0.14
B5_E_DISP	-0.17	0.01	-0.15	-0.21	-0.16	-0.20

[1] *Stress in ksi and Displacement in Inches*

Figure 102, Figure 103, and Figure 104 compare mid-span flange bottom longitudinal stress results from FEA of Model 4 and Model 5 (with $k = 3$ kip/in.^{3}) to the measured test results for Test 19, Test 20, and Test 21, respectively, where FEA stress values are in black text and measured stress results from the test are in red text in parentheses. In each figure, the results in the left image are from Model 4 and the results in the right image are from Model 5. As shown previously in Figure 93, Figure 94, and Figure 95 for Test 16, Test 17, and Test 18, respectively, Figure 102, Figure 103, and Figure 104, for Test 19, Test 20, and Test 21, respectively, show that Model 4, the most accurate of the FEA models considered in the pre-test analyses, does not accurately represent the measured stress response of the bridge, while Model 5 with soil springs to model the pressure on the backside of the end diaphragms (with $k = 3$ kip/in.^{3}) provides mid-span flange bottom stresses similar to the measured results.

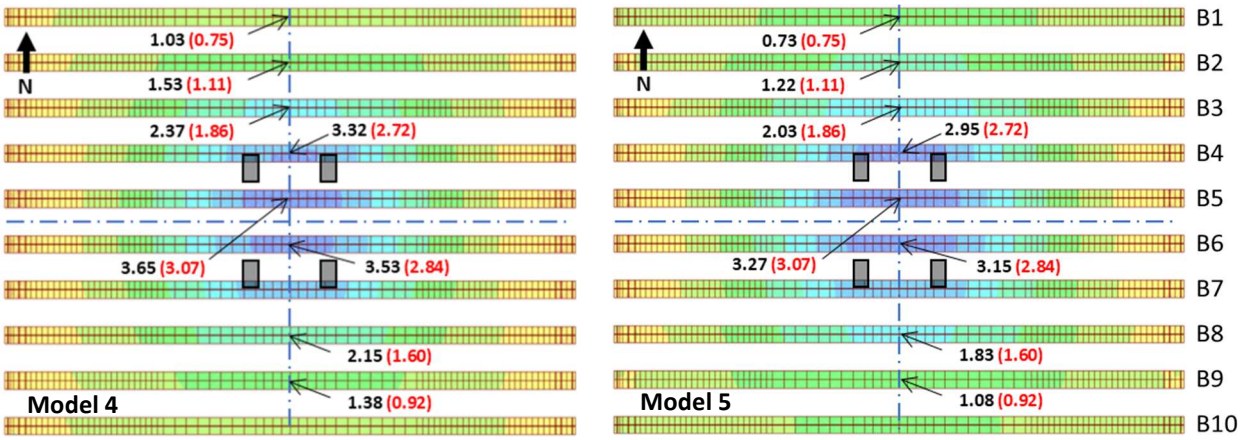

Figure 102. Test 19 longitudinal stress at flange bottom (Transverse Position 1, Longitudinal Position 3). Left: Model 4. Right: Model 5. FEA results in black; measured results in red in parentheses.

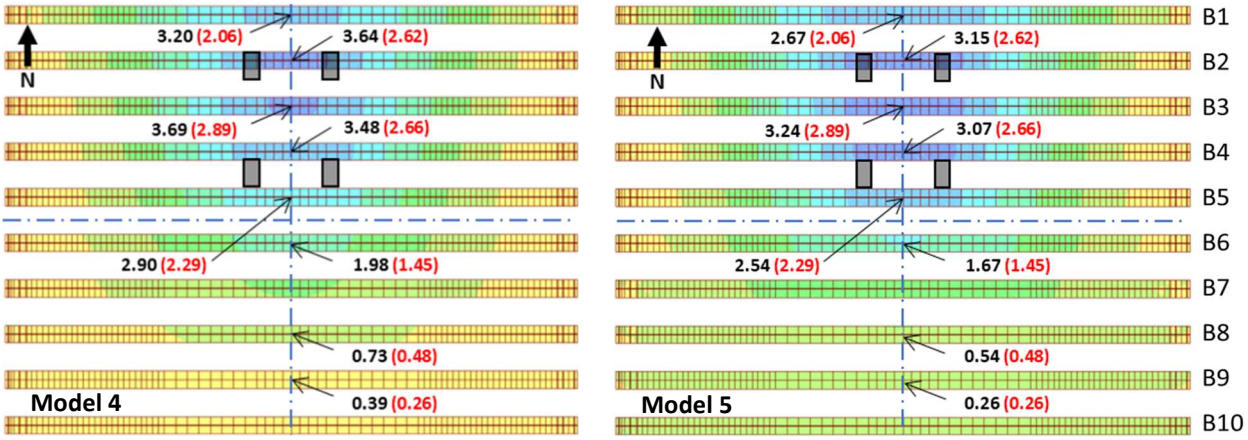

Figure 103. Test 20 longitudinal stress at flange bottom (Transverse Position 2, Longitudinal Position 3). Left: Model 4. Right: Model 5. FEA results in black; measured results in red in parentheses.

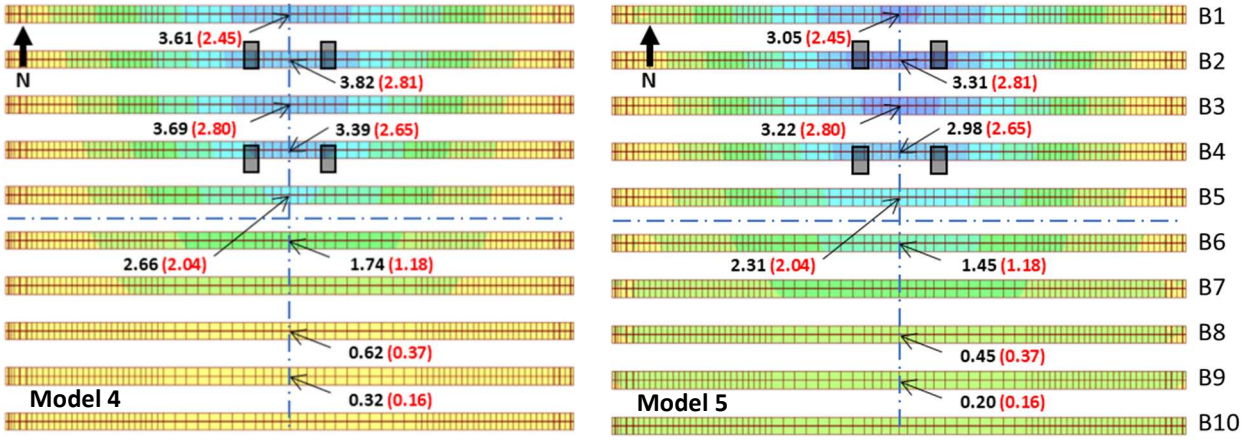

Figure 104. Test 21 longitudinal stress at flange bottom (Transverse Position 3, Longitudinal Position 3). Left: Model 4. Right: Model 5. FEA results in black; measured results in red in parentheses.

FEA results for both Model 4 and Model 5 (using the ATT) for the Test 19, Test 20, and Test 21, are presented in Table 11, along with the controlled-load testing results for comparison.

Table 11. Comparison of results measured in controlled-load testing, and results from FEA of Model 4 and FEA of Model 5.[1]

Channel Name	Test 19			Test 20			Test 21		
	Measured	FEA Model 4	FEA Model 5	Measured	FEA Model 4	FEA Model 5	Measured	FEA Model 4	FEA Model 5
B2_W_SG1	0.13	0.28	-0.01	-0.01	0.16	-0.35	0.04	0.17	-0.37
B2_QRT_SG1	0.75	1.07	0.76	1.19	1.82	1.32	1.31	1.94	1.42
B1_CL_SG1	0.75	1.03	0.73	2.06	3.20	2.67	2.45	3.61	3.05
B2_CL_SG1	1.11	1.53	1.22	2.62	3.64	3.15	2.81	3.82	3.31
B2_CL_SG2	0.03	-0.01	-0.01	0.20	0.06	0.04	0.17	0.06	0.04
B2_CL_SG3	0.24	0.01	-0.08	0.33	0.20	0.02	0.33	0.25	0.05
B2_CL_SG4	0.54	0.71	0.52	1.33	1.75	1.43	1.45	1.86	1.52
DK_2_3_SG2	0.02	0.00	-0.01	0.03	0.06	0.04	0.05	0.07	0.05
B3_CL_SG1	1.86	2.37	2.02	2.89	3.69	3.24	2.80	3.69	3.22
B4_CL_SG1	2.72	3.32	2.95	2.66	3.48	3.07	2.65	3.39	2.98
B4_CL_SG2	0.04	0.04	0.03	0.03	0.05	0.03	0.04	0.04	0.03
B4_CL_SG3	0.02	-0.09	-0.21	0.03	-0.05	-0.19	0.05	-0.02	-0.17
B5_QRT_SG1	1.22	1.62	1.21	1.04	1.38	1.00	0.95	1.34	0.98
B5_W_SG1	-0.25	-0.16	-0.60	-0.20	0.01	-0.37	-0.12	0.06	-0.31
B5_W_SG2	-0.02	-0.02	-0.03	-0.02	-0.01	-0.02	-0.01	-0.01	-0.02
B5_W_SG3	0.02	0.15	0.08	0.02	0.14	0.06	0.04	0.14	0.05
DK_4_5_SG2	-0.02	0.04	0.02	-0.01	0.03	0.02	-0.01	0.03	0.02
DK_4_5_SG5	0.10	0.29	0.28	0.08	0.22	0.21	0.06	0.19	0.18
B5_CL_SG1	3.07	3.65	3.27	2.29	2.90	2.54	2.04	2.66	2.30
B5_CL_SG3	-0.05	0.08	-0.27	-0.10	-0.09	-0.20	-0.07	-0.09	-0.20
B5_CL_SG4	1.19	1.57	1.35	0.88	1.26	1.04	0.81	1.16	0.95
B6_W_SG1	-0.31	-0.14	-0.51	0.02	0.13	-0.18	-0.01	0.16	-0.12
DK_5_6_SG2	0.01	0.06	0.04	0.00	0.02	0.01	0.00	0.01	0.00
B5_E_SG1	-0.20	-0.14	-0.58	-0.17	0.03	-0.36	-0.04	0.07	-0.30
B5_E_SG2	-0.01	-0.02	-0.03	-0.01	-0.02	-0.03	-0.01	-0.01	-0.02
B5_E_SG3	0.16	0.14	0.06	0.10	0.13	0.05	0.10	0.13	0.05
B6_CL_SG1	2.84	3.53	3.15	1.45	1.98	1.67	1.18	1.74	1.45
B8_CL_SG1	1.60	2.15	1.83	0.48	0.73	0.54	0.37	0.62	0.45
B9_CL_SG1	0.92	1.38	1.08	0.26	0.39	0.26	0.16	0.32	0.20
B2_W_DISP	0.00	0.06	0.06	0.18	0.13	0.14	0.22	0.14	0.15
B2_QRT_DISP	0.01	0.10	0.09	0.16	0.27	0.27	0.19	0.29	0.29
B5_W_DISP	0.21	0.13	0.14	0.28	0.10	0.11	0.27	0.09	0.10
B5_QRT_DISP	0.32	0.30	0.30	0.34	0.22	0.22	0.30	0.20	0.20
B5_CL_DISP	0.26	0.02	0.01	0.04	0.01	0.01	0.08	0.01	0.01
B5_E_DISP	-0.24	-0.14	-0.15	-0.28	-0.11	-0.12	-0.27	-0.10	-0.11

[1] *Stress in ksi and Displacement in Inches*

Table 12 compares maximum values of flange bottom stress for the ATT in Transverse Position 1, Longitudinal Position 3, the large moment case used previously in the line-girder analysis, and for the ATT in Transverse Position 1, Longitudinal Position 1, the large shear case used previously in the line-girder analysis. The results include: (1) results from the line-girder analysis using a transformed section and the vehicular load distribution factors for moment and shear given previously, (2) results from the most heavily loaded composite steel tee section from FEA of Model 1, (3) results from the most heavily loaded composite

steel tee section from FEA of Model 4, and (4) results from the most heavily loaded composite steel tee section from FEA of Model 5. The comparison shows that the line-girder analysis using a transformed-section with vehicular load distribution factors for moment or shear provides stress results that are quite conservative. The main reason for the conservative results appears to be the vehicular load distribution factors, since the results in Table 6 show that FEA of a model similar to Model 1, with shell elements to model the composite steel tee sections, link elements to model the interface shear connections, and simple supports to model the bearings provides results similar to those from the line-girder transformed-section analysis, *when both analyses use the vehicular load distribution factors*.

Table 12 shows that the effects of the different FEA models are much smaller than the effects of the load distribution factors. Even the simplest FEA model of the bridge, Model 1, with the bearings modeled as simple supports, and without models for the parapets, concrete end diaphragms, and semi-integral abutment conditions, provides significantly more accurate results than the line-girder analysis with the given vehicular load distribution factors. In comparison to the results from Model 1 (without the parapets, concrete end diaphragms, and semi-integral abutment conditions), the flange bottom flexural stress from the line-girder analysis is 65% greater than the FEA result from Model 1, which suggests the vehicular load distribution factor for flexure may be as much as 65% larger than the actual value for the Flex Beam demonstration bridge. Similarly, the maximum web shear stress from the line-girder analysis is 2.8 times the FEA result from Model 1, which suggests the vehicular load distribution factor for shear may be as much as 2.8 times larger than the actual value for the Flex Beam demonstration bridge. In comparison to the results from Model 5 (with the parapets, concrete end diaphragms, and semi-integral abutment conditions), the flange bottom flexural stress and maximum web shear stress from the line-girder analysis are even more conservative, suggesting that when the effects of all features of the Flex Beam demonstration bridge are included in determining these stresses, the vehicular load distribution factors are actually more conservative than it appears from comparison with Model 1. Note that the vehicular load distribution factor for shear is intended to provide the theoretical maximum shear force, which occurs when the 2nd axle of the tandem axle is centered on the bearing, while the results in Table 12 (for shear) are from the large shear load case (not maximum shear load case), as described earlier. It is also important to note that these extrapolations from the stresses in Table 12 to suggestions about vehicular distribution factors are speculative, and a comprehensive study of the vehicular load distribution factors for the Flex Beam system, considering various bridge spans and widths, variations in steel tee section spacing, and various load positions, is needed.

Table 12. Maximum flange bottom flexural stress for large moment load case and maximum web shear stress for large shear load case from line-girder transformed-section analysis and FEA results (using ATT).

Load Case	Line-Girder Transformed-Section Analysis (ksi)	FEA Model 1 (ksi)	FEA Model 4 (ksi)	FEA Model 5 (ksi)
Large Moment	6.34	3.83	3.65	3.27
Large Shear	2.91	1.03	0.25	0.23

4.6. Summary

This chapter presented FEA results from various FEA models of the Flex Beam demonstration bridge. In pre-test analyses, various FEA models were considered and evaluated, and Model 4 (made of solid elements, with bearing pads modeled as support springs, and with parapets, end diaphragms, and bearing stiffener plates included in the model) was used to generate FEA results for various test truck positions that were then used to develop an instrumentation plan and a controlled-load testing plan. In post-test analyses, FEA models were explored to develop an FEA model that provided results similar to the measured results

from the controlled-load testing. This FEA work showed the effects of pressure from the roadway subbase and backfill on the Flex Beam bridge end diaphragms are notable. Overall, the analytical work shows a line-girder analysis using a transformed-section with the load distribution factors for moment or shear provides stress results that are quite conservative compared to the FEA and measured response of the Flex Beam demonstration bridge. The analytical work suggests the vehicular load distribution factor for flexure used to design the Flex Beam demonstration bridge may be as much as 65% larger than the actual value for the Flex Beam demonstration bridge. Similarly, the vehicular load distribution factor for shear used to design the Flex Beam demonstration bridge may be as much as 2.8 times larger than the actual value for the Flex Beam demonstration bridge. A comprehensive study of vehicular load distribution factors for the Flex Beam system is needed.

CHAPTER 5: SUMMARY AND CONCLUSIONS

5.1. Summary

This report presents a study of an innovative highway bridge superstructure system termed the Flex Beam system, which was developed previously by Lehigh University in collaboration with the Pennsylvania Department of Transportation (PennDOT) and Modjeski and Masters (M&M), Inc. for short-span highway bridge applications. The system is comprised of inverted steel tee sections embedded in a concrete deck. An innovative mechanism for interface shear transfer between steel and concrete is provided by transverse deck reinforcement bars which pass through drilled holes near the tops of the steel tee webs. Previous research on the Flex Beam system was performed at Lehigh University which included analytical and laboratory studies (Naito, Hendricks, & Sause, 2018a) (Naito, Hendricks, & Sause, 2018b).

The first Flex Beam bridge was designed by PennDOT and constructed in Erie County, within PennDOT District 1, in 2021. This Flex Beam demonstration bridge carries Pageville Road over the West Branch of the Cussewago Creek. The bridge, consisting of ten (inverted steel tee section) units, has a span of 32 feet, and a width (from out-to-out) of 26 feet.

This study assessed experimentally and numerically the in-situ performance of the Flex Beam demonstration bridge. After instrumenting the bridge (with strain gauges and displacement sensors), the response of the Flex Beam bridge to controlled-load testing and typical traffic loading was measured. The controlled-load testing used a heavy truck of known dimensions and weight. Extensive finite element analyses (FEA) of the Flex Beam demonstration bridge were performed, and the ability of FEA to capture the actual measured behavior of the bridge, under various levels of FEA model refinement, was also assessed. Finally, the response of the Flex Beam bridge was compared to the response based on typical analysis and design assumptions.

5.2. Conclusions

The conclusions of this study of the Flex Beam demonstration bridge are as follows.

<u>Controlled-Load Testing</u>

1. The measured tensile stresses on the bottom of the concrete deck were generally small in magnitude. The largest tensile stresses at most strain gauge locations were less than 200 psi, far below the theoretical concrete cracking stress for the concrete deck, taken as 500 psi. The largest measured tensile stress on the bottom of the concrete deck was approximately 500 psi in the longitudinal direction from the strain gauge adjacent to steel tee section B2 as the wheels of the test truck traveled near the location of the gauge.

2. Strains measured across the cross-sections of individual composite steel tee sections show that the concrete deck is fully composite with the steel tee section. These results show the use of the plane-section assumption and transformed-section model (typically used for analysis and design) is valid within the span of the bridge away from the bearings and the influence of the concrete end diaphragms.

3. The concrete end diaphragms introduce rotational restraint at the ends of the composite steel tee sections. This restraint results in a small amount of negative flexure (i.e., reverse bending) at the ends of the steel tee sections (which produces compressive stresses on the flange bottom) when the tandem axle of the test truck was at mid-span of the bridge. This restraint also has the effect of reducing the largest flange bottom longitudinal (flexural) stress near mid-span. A complex strain and stress field was observed near the bearings of the composite steel tee sections (due to interaction

with the concrete end diaphragms), that is not consistent with the plane-section assumption. The test results and subsequent analytical work show that this stress field includes compression at the flange bottom, tension near the top of the web, compression at the bottom of the concrete deck, and tensile stress at the top of the concrete deck. The tensile stress at the top of the concrete deck was far below the theoretical concrete cracking stress, taken as 500 psi.

4. The effects of pressure from the roadway subbase and backfill on the end diaphragms (from the semi-integral abutment condition) are notable. These effects were demonstrated by comparing FEA results with the controlled load testing results. The effects of this pressure were observed to decrease the largest flange bottom longitudinal stresses near mid-span. Neglecting these effects in conventional design and assessment calculations appears to be conservative.

5. The relative displacements measured between the concrete deck and steel tee section were small (less than 0.001 in.) during the controlled-load testing, further demonstrating the fully composite behavior of the Flex Beam units (inverted steel tee section composite with concrete deck).

6. The dynamic amplification of the bridge response, assessed by comparing the results from the crawl tests and dynamic tests for a given transverse position of the test truck, was found to be small. It should be noted that the roadway on the bridge and on its approaches was smooth, without noticeable discontinuities near the ends of the bridge.

7. The response of the bridge from the controlled–load testing was consistent with the response expected from typical design and analysis calculations and with the results from previous research on the Flex Beam system. In general, the measured stresses were low.

Monitoring of Typical Vehicular-Load Response

1. The data from monitoring the bridge under typical vehicular loading are consistent with those from controlled-load testing; the strains and stresses are as expected.

2. The largest flange bottom stress from typical vehicular loading (1.94 ksi) is approximately 65 percent of the largest stress measured during controlled-load testing (3.07 ksi) under a test truck with a GVW of 77.55 kips.

3. The strains across the depth of the most heavily-loaded composite steel tee sections were consistent with the plane-section assumption (typically used for analysis and design).

4. Some of the data from events during the monitoring phase showed oscillations in mid-span flange bottom strain time-histories from vibration of the bridge, which was not observed during controlled-load testing, however, the stresses from these events were relatively small.

Analytical Work

1. The results of simple line-girder analysis using the plane-section assumption and fully composite behavior, and using a transformed-section model, compared well with results from an FEA model of a Flex Beam half unit (i.e., a single inverted steel section with composite deck).

2. Including the parapets in the FEA model had a significant effect on the response. Reduced longitudinal stresses on the flange bottom of the steel tee sections were observed in FEA results for a model with parapets included.

3. Reverse bending near the ends of the composite steel tee sections was observed in the solid element FEA models of the bridge in which the concrete end diaphragms were included. This reverse bending was consistent with the response observed during the controlled load testing. Tensile stress in the concrete deck from this reverse bending response was well below the theoretical concrete cracking stress, taken as 500 psi.

4. FEA results from a solid element model, with bearing pads, parapets, and end diaphragms included in the model (Model 4), were relatively consistent with controlled-load testing results.

5. Using the FEA model (Model 5) with soil springs to model the pressure from the roadway subbase and backfill on the Flex Beam bridge end diaphragms (from the semi-integral abutment condition) improved the agreement between the FEA and controlled-load testing results.

6. Stresses from a line-girder analysis with vehicular load distribution factors applied to the test truck load effects were significantly higher than those from a simple FEA model of the bridge and significantly higher than the measured test data, demonstrating the conservatism in this typical analysis and design approach. The analytical work suggests the vehicular load distribution factor for flexure used to design the Flex Beam demonstration bridge may be as much as 65% larger than the actual value for the Flex Beam demonstration bridge. Similarly, the vehicular load distribution factor for shear used to design the Flex Beam demonstration bridge may be as much as 2.8 times larger than the actual value for the Flex Beam demonstration bridge. A comprehensive study of vehicular load distribution factors for the Flex Beam system is needed.

REFERENCES

[1] Google, Edinboro, Pennsylvania. http://maps.google.com (Accessed: September, 2022).

[2] Commonwealth of Pennsylvania, Department of Transportation (PennDOT). *Erie county, S.R. 3010, Sec. B00, Segment0050, Offset 0000, STA. 108+02.00, Over West Branch Cussewago Creek, Superstructure Replacement & Streambed Paving*. District 1-0 Bridge Unit, Pennsylvania Department of Transportation (PennDOT). 2020

[3] Naito C., Hendricks R., Sause R. *Example Configurations of the PA Flex Beam Bridge System*. ATLSS Report 18-05. 2018a.

[4] Naito C., Hendricks R., Sause R. *Full-Scale Evaluation of the PA Flex Beam Bridge System*. ATLSS Report 18-04. 2018b.

[5] Cercone C., Naito C., Hendricks R., Sause, R. *Composite Steel Tee Concrete Bridge System: Performance of Interface Shear Connection*. Journal of Bridge Engineering, Vol. 26, Issue 3. March 2021.

[6] Design Manual, Part 4 (DM-4). *Structures: Procedures – Design – Plans Presentation – PDT – PUB No. 15M*. Pennsylvania Department of Transportation (PennDOT). December 2019 Edition.

[7] *Caltrans Seismic Design Criteria*. Version 1.7. California Department of Transportation. 2018.

[8] SAP2000 Version 17.3.0. Computers & Structures, INC. (CSI).

Appendix A: Controlled-Load Testing Results

i. Crawl Test Results

Table 13. Crawl test measured maximum and minimum stresses (ksi) and displacements (in.).

Channel Name	Test 1		Test 2		Test 3		Test 4		Test 5		Test 6		Test 22		Test 23	
	Max Neg	Max Pos	Max Neg	Max Pos	Max Neg	Max Pos	Max Neg	Max Pos	Max Neg	Max Pos	Max Neg	Max Pos	Max Neg	Max Pos	Max Neg	Max Pos
B2_W_SG1	-0.085	0.220	-0.058	0.254	-0.157	0.422	-0.194	0.362	-0.156	0.453	-0.193	0.401	-0.058	0.114	-0.081	0.122
B2_QRT_SG1	-0.114	0.795	-0.118	0.857	-0.099	2.029	-0.119	2.008	-0.087	2.220	-0.126	2.139	-0.065	0.255	-0.075	0.229
B1_CL_SG1	-0.086	0.776	-0.123	0.769	-0.127	2.052	-0.088	2.029	-0.140	2.324	-0.108	2.192	-0.086	0.184	-0.086	0.227
B2_CL_SG1	-0.098	1.086	-0.097	1.113	-0.110	2.676	-0.061	2.609	-0.070	2.849	-0.124	2.745	-0.087	0.293	-0.088	0.310
B2_CL_SG2	-0.005	0.046	-0.011	0.036	-0.012	0.359	-0.019	0.315	-0.005	0.523	-0.017	0.454	-0.025	0.009	-0.023	0.005
B2_CL_SG3	-0.081	0.270	-0.084	0.247	-0.069	0.512	-0.130	0.427	-0.051	0.519	-0.047	0.490	-0.057	0.130	-0.091	0.088
B2_CL_SG4	-0.086	0.568	-0.047	0.613	-0.104	1.398	-0.109	1.361	-0.087	1.486	-0.109	1.454	-0.061	0.200	-0.093	0.148
DK_2_3_SG2	-0.019	0.017	-0.005	0.031	-0.006	0.127	-0.010	0.135	-0.014	0.100	-0.012	0.112	-0.007	0.008	-0.018	0.002
B3_CL_SG1	-0.071	1.771	-0.074	1.828	-0.056	2.885	-0.090	2.833	-0.081	2.801	-0.070	2.832	-0.058	0.538	-0.074	0.509
B4_CL_SG1	-0.116	2.582	-0.056	2.616	-0.047	2.670	-0.090	2.624	-0.006	2.774	-0.088	2.671	-0.049	0.879	-0.085	0.931
B4_CL_SG2	-0.011	0.073	-0.012	0.064	-0.020	0.051	-0.027	0.047	-0.013	0.076	-0.022	0.055	-0.011	0.009	-0.021	0.007
B4_CL_SG3	-0.109	0.356	-0.091	0.319	-0.128	0.316	-0.153	0.362	-0.036	0.429	-0.128	0.315	-0.088	0.109	-0.109	0.093
B5_QRT_SG1	-0.090	2.275	-0.191	2.239	-0.129	1.832	-0.194	1.734	-0.162	1.596	-0.078	1.740	-0.051	1.151	-0.106	1.123
B5_W_SG1	-0.403	0.477	-0.320	0.507	-0.261	0.389	-0.327	0.357	-0.172	0.387	-0.256	0.371	-0.097	0.217	-0.087	0.274
B5_W_SG2	-0.043	0.030	-0.034	0.034	-0.033	0.048	-0.042	0.046	-0.035	0.022	-0.033	0.032	-0.021	0.006	-0.013	0.011
B5_W_SG3	-0.073	0.267	-0.077	0.314	-0.060	0.237	-0.156	0.147	-0.101	0.229	-0.102	0.185	-0.076	0.118	-0.082	0.108
DK_4_5_SG2	-0.024	0.098	-0.017	0.110	-0.032	0.075	-0.015	0.086	-0.022	0.081	-0.030	0.085	-0.014	0.006	-0.010	0.018
DK_4_5_SG5	-0.013	0.107	-0.013	0.112	-0.023	0.066	-0.014	0.082	-0.015	0.083	-0.012	0.080	-0.026	0.007	-0.026	0.006
B5_CL_SG1	-0.108	2.895	-0.035	2.940	-0.098	2.364	-0.123	2.349	-0.113	2.134	-0.067	2.245	-0.057	1.438	-0.091	1.481
B5_CL_SG3	-0.195	0.254	-0.234	0.241	-0.266	0.207	-0.304	0.131	-0.179	0.187	-0.218	0.190	-0.087	0.070	-0.072	0.079
B5_CL_SG4	-0.069	1.192	-0.087	1.189	-0.087	0.975	-0.157	0.948	-0.094	0.868	-0.140	0.866	-0.053	0.651	-0.098	0.598
B6_W_SG1	-0.439	0.440	-0.357	0.496	-0.148	0.322	-0.174	0.306	-0.117	0.295	-0.111	0.296	-0.238	0.320	-0.208	0.359
DK_5_6_SG2	-0.024	0.007	-0.018	0.013	-0.034	-0.002	-0.022	0.010	-0.013	0.023	-0.004	0.026	-0.013	0.013	-0.013	0.020
B5_E_SG1	-0.291	0.410	-0.310	0.416	-0.153	0.371	-0.231	0.298	-0.180	0.260	-0.202	0.303	-0.023	0.379	-0.092	0.337
B5_E_SG2	-0.019	0.015	-0.024	0.009	-0.023	0.014	-0.016	0.016	-0.028	0.007	-0.023	0.012	-0.010	0.008	-0.010	0.010
B5_E_SG3	-0.028	0.416	-0.139	0.263	-0.051	0.359	-0.085	0.224	-0.150	0.152	-0.099	0.232	-0.052	0.165	-0.121	0.116
B6_CL_SG1	-0.068	2.755	-0.143	2.691	-0.073	1.551	-0.037	1.588	-0.128	1.343	-0.089	1.390	-0.083	2.221	-0.047	2.322
B8_CL_SG1	-0.118	1.595	-0.066	1.593	-0.142	0.522	-0.056	0.631	-0.088	0.512	-0.051	0.542	-0.087	2.868	-0.128	2.807
B9_CL_SG1	-0.090	0.975	-0.104	0.991	-0.046	0.364	-0.044	0.352	-0.040	0.312	-0.065	0.259	-0.088	2.892	-0.046	2.793
B2_W_DISP	-0.019	0.026	-0.015	0.035	-0.014	0.400	-0.030	0.329	-0.066	0.484	-0.042	0.438	-0.046	0.021	-0.024	0.030
B2_QRT_DISP	-0.032	0.049	-0.033	0.060	-0.159	0.184	-0.177	0.141	-0.238	0.247	-0.210	0.216	-0.030	0.025	-0.040	0.025
B5_W_DISP	-0.080	0.490	-0.105	0.472	-0.046	0.501	-0.051	0.513	-0.044	0.447	-0.045	0.485	-0.043	0.025	-0.067	0.008
B5_QRT_DISP	-0.216	0.411	-0.228	0.387	-0.151	0.433	-0.175	0.421	-0.143	0.376	-0.140	0.411	-0.040	0.026	-0.101	0.022
B5_CL_DISP	-0.726	0.770	-0.749	0.753	-0.652	0.676	-0.682	0.658	-0.587	0.554	-0.607	0.651	-0.019	0.270	-0.045	0.166
B5_E_DISP	-0.022	0.595	-0.028	0.581	-0.050	0.570	-0.045	0.594	-0.027	0.513	-0.035	0.546	-0.019	0.040	-0.014	0.072

Table 14. Crawl test average maximum and minimum stresses (ksi) and displacements (in.).

Channel Name	Average Test 1 & 2 (Trans. Pos. 1 west)		Average Test 3 & 4 (Trans. Pos. 2 west)		Average Test 5 & 6 (Trans. Pos. 3 west)		Average Test 22 & 23 (Trans. Pos. 2 east)	
	Max Neg	Max Pos	Max Neg	Max Pos	Max Neg	Max Pos	Max Neg	Max Pos
B2_W_SG1	-0.071	0.237	-0.176	0.392	-0.175	0.427	-0.069	0.118
B2_QRT_SG1	-0.116	0.826	-0.109	2.018	-0.106	2.180	-0.070	0.242
B1_CL_SG1	-0.105	0.772	-0.107	2.041	-0.124	2.258	-0.086	0.206
B2_CL_SG1	-0.097	1.099	-0.086	2.643	-0.097	2.797	-0.088	0.302
B2_CL_SG2	-0.008	0.041	-0.015	0.337	-0.011	0.489	-0.024	0.007
B2_CL_SG3	-0.083	0.259	-0.100	0.470	-0.049	0.505	-0.074	0.109
B2_CL_SG4	-0.066	0.591	-0.106	1.379	-0.098	1.470	-0.077	0.174
DK_2_3_SG2	-0.012	0.024	-0.008	0.131	-0.013	0.106	-0.013	0.005
B3_CL_SG1	-0.073	1.800	-0.073	2.859	-0.075	2.816	-0.066	0.523
B4_CL_SG1	-0.086	2.599	-0.068	2.647	-0.047	2.723	-0.067	0.905
B4_CL_SG2	-0.012	0.069	-0.024	0.049	-0.018	0.066	-0.016	0.008
B4_CL_SG3	-0.100	0.337	-0.141	0.339	-0.082	0.372	-0.099	0.101
B5_QRT_SG1	-0.141	2.257	-0.162	1.783	-0.120	1.668	-0.078	1.137
B5_W_SG1	-0.362	0.492	-0.294	0.373	-0.214	0.379	-0.092	0.246
B5_W_SG2	-0.038	0.032	-0.038	0.047	-0.034	0.027	-0.017	0.009
B5_W_SG3	-0.075	0.291	-0.108	0.192	-0.102	0.207	-0.079	0.113
DK_4_5_SG2	-0.021	0.104	-0.023	0.080	-0.026	0.083	-0.012	0.012
DK_4_5_SG5	-0.013	0.110	-0.018	0.074	-0.014	0.081	-0.026	0.006
B5_CL_SG1	-0.071	2.918	-0.110	2.356	-0.090	2.189	-0.074	1.459
B5_CL_SG3	-0.214	0.248	-0.285	0.169	-0.198	0.188	-0.080	0.074
B5_CL_SG4	-0.078	1.191	-0.122	0.962	-0.117	0.867	-0.075	0.625
B6_W_SG1	-0.398	0.468	-0.161	0.314	-0.114	0.295	-0.223	0.339
DK_5_6_SG2	-0.021	0.010	-0.028	0.004	-0.009	0.025	-0.013	0.016
B5_E_SG1	-0.300	0.413	-0.192	0.334	-0.191	0.281	-0.058	0.358
B5_E_SG2	-0.021	0.012	-0.020	0.015	-0.025	0.010	-0.010	0.009
B5_E_SG3	-0.083	0.339	-0.068	0.291	-0.124	0.192	-0.086	0.141
B6_CL_SG1	-0.106	2.723	-0.055	1.570	-0.108	1.367	-0.065	2.272
B8_CL_SG1	-0.092	1.594	-0.099	0.576	-0.069	0.527	-0.107	2.837
B9_CL_SG1	-0.097	0.983	-0.045	0.358	-0.053	0.286	-0.067	2.843
B2_W_DISP	-0.017	0.030	-0.022	0.364	-0.054	0.461	-0.035	0.025
B2_QRT_DISP	-0.033	0.055	-0.168	0.163	-0.224	0.231	-0.035	0.025
B5_W_DISP	-0.092	0.481	-0.048	0.507	-0.044	0.466	-0.055	0.016
B5_QRT_DISP	-0.222	0.399	-0.163	0.427	-0.141	0.394	-0.071	0.024
B5_CL_DISP	-0.738	0.762	-0.667	0.667	-0.597	0.603	-0.032	0.218
B5_E_DISP	-0.025	0.588	-0.048	0.582	-0.031	0.529	-0.016	0.056

ii. Dynamic Test Results

Table 15. Dynamic test measured maximum and minimum stresses (ksi) and displacements (in.).

Channel Name	Test 7		Test 8		Test 9		Test 10		Test 11		Test 12		Test 24		Test 25	
	Max Neg	Max Pos	Max Neg	Max Pos	Max Neg	Max Pos	Max Neg	Max Pos	Max Neg	Max Pos	Max Neg	Max Pos	Max Neg	Max Pos	Max Neg	Max Pos
B2_W_SG1	-0.097	0.168	-0.071	0.189	-0.209	0.249	-0.154	0.314	-0.124	0.412	-0.124	0.378	-0.061	0.119	-0.073	0.114
B2_QRT_SG1	-0.106	0.628	-0.073	0.721	-0.165	1.924	-0.098	1.741	-0.153	2.181	-0.126	2.176	-0.082	0.300	-0.052	0.312
B1_CL_SG1	-0.065	0.740	-0.077	0.703	-0.124	1.690	-0.006	1.814	-0.076	2.064	-0.058	2.333	-0.080	0.263	-0.062	0.235
B2_CL_SG1	-0.067	1.062	-0.086	1.010	-0.094	2.165	-0.006	2.338	-0.085	2.512	-0.089	2.601	-0.066	0.386	-0.070	0.384
B2_CL_SG2	-0.004	0.045	-0.007	0.042	-0.008	0.226	-0.010	0.224	-0.009	0.400	-0.005	0.464	-0.017	0.008	-0.021	0.005
B2_CL_SG3	-0.093	0.174	-0.045	0.196	-0.093	0.373	-0.058	0.405	-0.018	0.493	-0.086	0.539	-0.060	0.080	-0.055	0.076
B2_CL_SG4	-0.026	0.628	-0.069	0.524	-0.089	1.124	-0.078	1.200	-0.026	1.381	-0.063	1.409	-0.099	0.166	-0.076	0.176
DK_2_3_SG2	-0.002	0.034	-0.016	0.016	-0.008	0.122	-0.012	0.122	-0.003	0.124	-0.007	0.084	-0.009	0.006	-0.004	0.009
B3_CL_SG1	-0.024	1.686	-0.064	1.558	-0.043	2.684	-0.046	2.727	-0.062	2.577	-0.065	2.568	-0.090	0.638	-0.051	0.616
B4_CL_SG1	-0.001	2.410	-0.073	2.227	-0.056	2.413	-0.064	2.469	-0.065	2.358	-0.060	2.499	-0.060	0.997	-0.080	0.924
B4_CL_SG2	-0.010	0.047	-0.016	0.046	-0.001	0.059	-0.010	0.049	-0.008	0.061	-0.005	0.068	-0.008	0.016	-0.012	0.007
B4_CL_SG3	-0.067	0.283	-0.075	0.269	-0.003	0.410	-0.095	0.365	-0.057	0.401	-0.150	0.454	-0.052	0.114	-0.113	0.079
B5_QRT_SG1	-0.133	2.014	-0.119	2.170	-0.088	1.949	-0.091	1.772	-0.079	1.733	-0.060	1.613	-0.076	1.345	-0.074	1.239
B5_W_SG1	-0.468	0.382	-0.336	0.372	-0.305	0.345	-0.293	0.366	-0.186	0.336	-0.182	0.206	-0.088	0.192	-0.071	0.225
B5_W_SG2	-0.049	0.042	-0.044	0.035	-0.040	0.037	-0.036	0.038	-0.029	0.029	-0.029	0.023	-0.018	0.008	-0.017	0.005
B5_W_SG3	-0.202	0.110	-0.115	0.116	-0.172	0.099	-0.087	0.209	-0.065	0.179	-0.013	0.190	-0.092	0.080	-0.085	0.074
DK_4_5_SG2	-0.013	0.101	-0.023	0.083	-0.007	0.065	-0.006	0.073	-0.015	0.077	-0.009	0.092	-0.019	0.002	-0.010	0.008
DK_4_5_SG5	-0.003	0.091	-0.006	0.082	-0.003	0.055	-0.005	0.054	-0.005	0.073	-0.009	0.062	-0.015	0.002	-0.010	0.011
B5_CL_SG1	-0.070	2.970	-0.043	2.585	-0.036	2.327	-0.043	2.363	-0.021	2.074	-0.072	1.928	-0.074	1.640	-0.032	1.587
B5_CL_SG3	-0.235	0.241	-0.204	0.242	-0.246	0.214	-0.227	0.257	-0.209	0.191	-0.105	0.143	-0.054	0.154	-0.042	0.079
B5_CL_SG4	-0.071	1.215	-0.050	1.037	-0.037	0.946	-0.039	0.991	-0.064	0.870	-0.077	0.809	-0.098	0.687	-0.079	0.632
B6_W_SG1	-0.431	0.390	-0.384	0.388	-0.141	0.311	-0.192	0.306	-0.080	0.285	-0.102	0.161	-0.214	0.294	-0.225	0.265
DK_5_6_SG2	-0.018	0.007	-0.007	0.015	0.002	0.030	-0.016	0.009	-0.009	0.013	-0.008	0.016	-0.016	0.006	-0.006	0.019
B5_E_SG1	-0.257	0.466	-0.271	0.329	-0.211	0.324	-0.182	0.372	-0.136	0.301	-0.230	0.279	-0.167	0.262	-0.107	0.308
B5_E_SG2	-0.010	0.016	-0.015	0.011	-0.019	0.010	-0.026	0.008	-0.019	0.008	-0.017	0.010	-0.009	0.009	-0.007	0.009
B5_E_SG3	-0.112	0.282	-0.074	0.286	-0.058	0.275	-0.056	0.349	-0.046	0.249	-0.042	0.259	-0.131	0.103	-0.047	0.139
B6_CL_SG1	-0.046	2.756	-0.038	2.455	-0.051	1.615	-0.061	1.635	-0.040	1.374	-0.061	1.256	-0.063	2.338	-0.017	2.277
B8_CL_SG1	-0.074	1.900	-0.070	1.567	-0.015	0.759	-0.022	0.718	-0.058	0.597	-0.043	0.481	-0.105	2.659	-0.033	2.781
B9_CL_SG1	-0.050	1.229	-0.104	0.987	-0.062	0.421	-0.098	0.367	-0.042	0.342	-0.076	0.212	-0.115	2.368	-0.093	2.508
B2_W_DISP	-0.033	0.021	-0.024	0.019	-0.012	0.282	-0.012	0.276	-0.016	0.416	-0.050	0.464	-0.021	0.020	-0.032	0.017
B2_QRT_DISP	-0.037	0.035	-0.028	0.037	-0.061	0.100	-0.068	0.102	-0.118	0.211	-0.058	0.277	-0.020	0.030	-0.026	0.022
B5_W_DISP	-0.101	0.500	-0.084	0.463	-0.043	0.461	-0.046	0.500	-0.036	0.418	-0.026	0.420	-0.020	0.071	-0.017	0.079
B5_QRT_DISP	-0.257	0.347	-0.237	0.356	-0.152	0.395	-0.161	0.396	-0.112	0.418	-0.090	0.391	-0.030	0.038	-0.029	0.045
B5_CL_DISP	-0.703	0.784	-0.758	0.734	-0.693	0.715	-0.677	0.680	-0.636	0.708	-0.373	0.763	-0.078	0.367	-0.027	0.333
B5_E_DISP	-0.029	0.486	-0.018	0.502	-0.029	0.518	-0.029	0.546	-0.041	0.489	-0.031	0.466	-0.015	0.083	-0.033	0.045

Table 16. Dynamic test average maximum and minimum stresses (ksi) and displacements (in.).

Channel Name	Average Test 7 & 8 (Trans. Pos. 1 west)		Average Test 9 & 10 (Trans. Pos. 2 west)		Average Test 11 & 12 (Trans. Pos. 3 west)		Average Test 24 & 25 (Trans. Pos. 2 east)	
	Max Neg	Max Pos	Max Neg	Max Pos	Max Neg	Max Pos	Max Neg	Max Pos
B2_W_SG1	-0.084	0.178	-0.181	0.281	-0.124	0.395	-0.067	0.117
B2_QRT_SG1	-0.089	0.675	-0.132	1.833	-0.140	2.178	-0.067	0.306
B1_CL_SG1	-0.071	0.722	-0.065	1.752	-0.067	2.199	-0.071	0.249
B2_CL_SG1	-0.076	1.036	-0.050	2.251	-0.087	2.557	-0.068	0.385
B2_CL_SG2	-0.006	0.043	-0.009	0.225	-0.007	0.432	-0.019	0.007
B2_CL_SG3	-0.069	0.185	-0.076	0.389	-0.052	0.516	-0.058	0.078
B2_CL_SG4	-0.048	0.576	-0.083	1.162	-0.044	1.395	-0.088	0.171
DK_2_3_SG2	-0.009	0.025	-0.010	0.122	-0.005	0.104	-0.006	0.008
B3_CL_SG1	-0.044	1.622	-0.044	2.705	-0.063	2.573	-0.070	0.627
B4_CL_SG1	-0.037	2.318	-0.060	2.441	-0.062	2.428	-0.070	0.960
B4_CL_SG2	-0.013	0.046	-0.006	0.054	-0.007	0.064	-0.010	0.011
B4_CL_SG3	-0.071	0.276	-0.049	0.387	-0.103	0.428	-0.082	0.097
B5_QRT_SG1	-0.126	2.092	-0.090	1.860	-0.070	1.673	-0.075	1.292
B5_W_SG1	-0.402	0.377	-0.299	0.355	-0.184	0.271	-0.079	0.209
B5_W_SG2	-0.047	0.038	-0.038	0.037	-0.029	0.026	-0.017	0.007
B5_W_SG3	-0.159	0.113	-0.130	0.154	-0.039	0.184	-0.089	0.077
DK_4_5_SG2	-0.018	0.092	-0.006	0.069	-0.012	0.085	-0.014	0.005
DK_4_5_SG5	-0.005	0.086	-0.004	0.055	-0.007	0.067	-0.013	0.007
B5_CL_SG1	-0.057	2.778	-0.039	2.345	-0.046	2.001	-0.053	1.613
B5_CL_SG3	-0.220	0.241	-0.237	0.236	-0.157	0.167	-0.048	0.117
B5_CL_SG4	-0.061	1.126	-0.038	0.968	-0.071	0.840	-0.088	0.660
B6_W_SG1	-0.408	0.389	-0.166	0.308	-0.091	0.223	-0.220	0.279
DK_5_6_SG2	-0.012	0.011	-0.007	0.020	-0.009	0.014	-0.011	0.012
B5_E_SG1	-0.264	0.398	-0.197	0.348	-0.183	0.290	-0.137	0.285
B5_E_SG2	-0.012	0.014	-0.023	0.009	-0.018	0.009	-0.008	0.009
B5_E_SG3	-0.093	0.284	-0.057	0.312	-0.044	0.254	-0.089	0.121
B6_CL_SG1	-0.042	2.606	-0.056	1.625	-0.051	1.315	-0.040	2.307
B8_CL_SG1	-0.072	1.734	-0.019	0.738	-0.051	0.539	-0.069	2.720
B9_CL_SG1	-0.077	1.108	-0.080	0.394	-0.059	0.277	-0.104	2.438
B2_W_DISP	-0.028	0.020	-0.012	0.279	-0.033	0.440	-0.026	0.019
B2_QRT_DISP	-0.033	0.036	-0.065	0.101	-0.088	0.244	-0.023	0.026
B5_W_DISP	-0.092	0.481	-0.044	0.480	-0.031	0.419	-0.018	0.075
B5_QRT_DISP	-0.247	0.352	-0.156	0.396	-0.101	0.404	-0.030	0.042
B5_CL_DISP	-0.730	0.759	-0.685	0.697	-0.504	0.736	-0.053	0.350
B5_E_DISP	-0.024	0.494	-0.029	0.532	-0.036	0.478	-0.024	0.064

iii. Park Test Results

Table 17. Park test stresses (ksi) and displacements (in.).

Channel Name	Test 13	Test 14	Test 15	Test 16	Test 17	Test 18	Test 19	Test 20	Test 21	Test 26	Test 27	Test 28	Test 29
B2_W_SG1	0.126	0.227	0.214	0.172	0.146	0.157	0.129	-0.011	0.039	0.126	0.090	0.103	0.179
B2_QRT_SG1	0.341	0.579	0.599	0.577	0.991	0.915	0.753	1.190	1.307	0.205	0.160	0.208	0.768
B1_CL_SG1	0.186	0.422	0.439	0.576	1.407	1.646	0.753	2.062	2.450	0.078	0.112	0.159	0.909
B2_CL_SG1	0.262	0.348	0.371	0.822	1.412	1.511	1.107	2.623	2.806	0.186	0.263	0.292	0.873
B2_CL_SG2	0.014	0.033	0.050	0.040	0.137	0.142	0.027	0.197	0.171	-0.008	-0.010	-0.017	0.082
B2_CL_SG3	0.123	0.087	0.086	0.185	0.315	0.290	0.245	0.332	0.331	0.017	0.053	0.066	0.127
B2_CL_SG4	0.126	0.216	0.165	0.434	0.785	0.847	0.537	1.326	1.450	0.087	0.144	0.186	0.479
DK_2_3_SG2	0.001	0.008	-0.001	0.012	0.027	0.029	0.020	0.028	0.052	0.000	0.000	0.013	0.002
B3_CL_SG1	0.343	0.336	0.379	1.044	1.436	1.553	1.859	2.890	2.801	0.357	0.471	0.525	0.995
B4_CL_SG1	0.379	0.362	0.353	1.234	1.417	1.368	2.719	2.660	2.646	0.533	0.754	0.867	0.858
B4_CL_SG2	0.002	-0.003	-0.003	0.024	0.033	0.025	0.041	0.033	0.042	0.001	-0.001	-0.001	0.015
B4_CL_SG3	0.074	0.056	0.176	0.078	0.056	0.080	0.015	0.034	0.052	0.063	0.009	0.060	-0.009
B5_QRT_SG1	0.822	0.526	0.565	0.908	0.738	0.690	1.222	1.041	0.949	0.680	1.050	0.915	0.664
B5_W_SG1	0.346	0.169	0.183	0.016	0.023	-0.002	-0.252	-0.197	-0.121	0.296	0.246	0.052	0.064
B5_W_SG2	-0.022	-0.023	-0.017	-0.020	-0.022	-0.019	-0.020	-0.020	-0.013	0.000	-0.008	-0.006	-0.031
B5_W_SG3	0.150	0.117	0.111	0.056	0.073	0.062	0.017	0.018	0.044	0.074	0.094	0.095	0.046
DK_4_5_SG2	-0.004	-0.011	0.004	-0.012	-0.003	-0.001	-0.024	-0.009	-0.009	-0.008	0.001	0.000	-0.012
DK_4_5_SG5	0.014	0.003	0.008	0.041	0.034	0.024	0.102	0.078	0.057	-0.004	-0.004	-0.015	0.021
B5_CL_SG1	0.335	0.283	0.279	1.395	1.227	1.161	3.068	2.294	2.037	0.766	1.051	1.498	0.786
B5_CL_SG3	-0.082	-0.021	-0.031	0.143	0.196	0.143	-0.049	-0.096	-0.075	0.045	0.028	0.014	0.084
B5_CL_SG4	0.166	0.074	0.082	0.626	0.488	0.526	1.193	0.882	0.805	0.331	0.426	0.597	0.389
B6_W_SG1	0.243	0.208	0.162	0.014	0.125	0.167	-0.313	0.019	-0.008	0.233	0.112	-0.105	0.117
DK_5_6_SG2	-0.010	-0.009	-0.002	-0.006	0.004	0.006	0.006	0.004	-0.002	0.001	0.004	0.009	-0.006
B5_E_SG1	0.016	-0.042	-0.021	0.100	0.062	0.118	-0.197	-0.175	-0.037	0.031	0.109	-0.025	-0.171
B5_E_SG2	0.005	0.001	0.000	-0.019	-0.017	-0.012	-0.006	-0.012	-0.012	-0.004	0.006	0.000	-0.011
B5_E_SG3	0.060	0.082	0.000	0.274	0.218	0.212	0.164	0.102	0.102	0.002	0.063	0.034	0.031
B6_CL_SG1	0.361	0.270	0.278	1.350	0.959	0.917	2.840	1.447	1.183	0.880	1.234	2.377	0.665
B8_CL_SG1	0.287	0.150	0.101	0.991	0.471	0.345	1.598	0.481	0.372	1.054	1.508	2.863	0.295
B9_CL_SG1	0.242	0.082	0.087	0.727	0.265	0.182	0.921	0.260	0.165	0.984	1.412	2.694	0.165
B2_W_DISP	0.005	0.255	0.256	0.003	0.325	0.326	0.004	0.176	0.225	0.003	0.000	-0.006	0.304
B2_QRT_DISP	-0.005	-0.089	-0.155	0.014	0.005	0.007	0.014	0.155	0.187	0.005	0.000	0.000	-0.017
B5_W_DISP	0.332	0.283	0.254	0.252	0.338	0.325	0.205	0.275	0.270	0.017	0.025	0.015	0.377
B5_QRT_DISP	-0.160	-0.122	-0.093	0.038	0.048	0.068	0.319	0.340	0.296	0.010	0.005	0.002	-0.023
B5_CL_DISP	-0.488	-0.455	-0.420	0.399	0.316	0.248	0.265	0.037	0.081	0.056	0.013	0.010	0.225
B5_E_DISP	-0.034	-0.049	-0.078	-0.583	-0.531	-0.489	-0.237	-0.277	-0.274	-0.027	-0.025	-0.026	-0.216

iv. Dynamic Amplification Factor

Table 18. Dynamic amplification factor (DAF): $f_{Dynamic}/f_{Crawl}$.

Channel Name	Dynamic Amplification (Trans. Pos. 1 west)		Dynamic Amplification (Trans. Pos. 2 west)		Dynamic Amplification (Trans. Pos. 3 west)		Dynamic Amplification (Trans. Pos. 2 east)	
	Max Neg	Max Pos	Max Neg	Max Pos	Max Neg	Max Pos	Max Neg	Max Pos
B2_W_SG1	1.173	0.751	1.031	0.718	0.707	0.926	0.974	0.987
B2_QRT_SG1	0.770	0.817	1.209	0.908	1.313	0.999	0.948	1.264
B1_CL_SG1	0.679	0.934	0.610	0.858	0.539	0.974	0.822	1.209
B2_CL_SG1	0.785	0.942	0.580	0.852	0.894	0.914	0.773	1.276
B2_CL_SG2	0.680	1.044	0.563	0.668	0.629	0.884	0.785	0.955
B2_CL_SG3	0.835	0.715	0.760	0.828	1.070	1.023	0.778	0.717
B2_CL_SG4	0.719	0.975	0.784	0.842	0.451	0.949	1.144	0.982
DK_2_3_SG2	0.757	1.037	1.286	0.932	0.407	0.979	0.491	1.515
B3_CL_SG1	0.600	0.901	0.609	0.946	0.842	0.913	1.062	1.197
B4_CL_SG1	0.431	0.892	0.882	0.922	1.323	0.892	1.044	1.061
B4_CL_SG2	1.117	0.675	0.241	1.104	0.384	0.983	0.596	1.447
B4_CL_SG3	0.711	0.819	0.350	1.141	1.265	1.150	0.834	0.959
B5_QRT_SG1	0.897	0.927	0.555	1.043	0.580	1.003	0.961	1.136
B5_W_SG1	1.111	0.767	1.016	0.954	0.859	0.716	0.862	0.849
B5_W_SG2	1.221	1.191	1.007	0.803	0.839	0.960	1.020	0.769
B5_W_SG3	2.122	0.390	1.204	0.802	0.382	0.891	1.123	0.683
DK_4_5_SG2	0.850	0.887	0.271	0.860	0.450	1.021	1.226	0.398
DK_4_5_SG5	0.373	0.785	0.220	0.738	0.505	0.830	0.482	1.036
B5_CL_SG1	0.794	0.952	0.356	0.995	0.513	0.914	0.722	1.106
B5_CL_SG3	1.025	0.976	0.832	1.396	0.792	0.888	0.602	1.567
B5_CL_SG4	0.782	0.946	0.310	1.007	0.604	0.969	1.174	1.056
B6_W_SG1	1.024	0.831	1.031	0.981	0.800	0.755	0.986	0.824
DK_5_6_SG2	0.604	1.104	0.250	5.138	1.004	0.580	0.835	0.766
B5_E_SG1	0.879	0.963	1.024	1.042	0.959	1.030	2.384	0.797
B5_E_SG2	0.578	1.140	1.153	0.607	0.710	0.906	0.838	1.002
B5_E_SG3	1.118	0.837	0.829	1.070	0.355	1.325	1.032	0.862
B6_CL_SG1	0.398	0.957	1.022	1.035	0.469	0.962	0.625	1.016
B8_CL_SG1	0.784	1.087	0.189	1.281	0.730	1.022	0.642	0.959
B9_CL_SG1	0.795	1.127	1.770	1.102	1.115	0.970	1.552	0.858
B2_W_DISP	1.649	0.647	0.552	0.767	0.620	0.954	0.746	0.731
B2_QRT_DISP	0.998	0.658	0.385	0.623	0.393	1.054	0.647	1.050
B5_W_DISP	1.002	1.001	0.916	0.947	0.700	0.900	0.327	4.617
B5_QRT_DISP	1.115	0.881	0.960	0.928	0.713	1.026	0.424	1.734
B5_CL_DISP	0.990	0.996	1.027	1.046	0.845	1.221	1.653	1.608
B5_E_DISP	0.944	0.841	0.609	0.915	1.155	0.902	1.476	1.134

APPENDIX B: FINITE ELEMENT ANALYSIS RESULTS

i. Model 4 Results

Table 19. FEA results for stresses (ksi) and displacements (in.) for Model 4.

Channel Name	Test 13	Test 14	Test 15	Test 16	Test 17	Test 18	Test 19	Test 20	Test 21	Test 26	Test 27	Test 28	Test 29
B2_W_SG1	0.156	0.243	0.256	0.240	0.201	0.230	0.278	0.159	0.166	0.103	0.175	0.194	0.270
B2_QRT_SG1	0.372	0.802	0.853	0.801	1.390	1.466	1.068	1.818	1.937	0.182	0.279	0.332	1.116
B1_CL_SG1	0.257	0.566	0.600	0.845	2.103	2.273	1.025	3.196	3.607	0.105	0.160	0.191	1.327
B2_CL_SG1	0.319	0.483	0.515	1.130	1.921	2.055	1.534	3.643	3.823	0.228	0.333	0.394	1.241
B2_CL_SG2	0.002	0.010	0.011	0.002	0.035	0.038	-0.006	0.060	0.064	-0.008	-0.012	-0.016	0.021
B2_CL_SG3	0.024	0.066	0.073	0.053	0.281	0.306	0.014	0.204	0.246	-0.021	-0.033	-0.044	0.169
B2_CL_SG4	0.159	0.259	0.278	0.546	1.041	1.109	0.706	1.752	1.857	0.093	0.135	0.157	0.666
DK_2_3_SG2	0.003	0.009	0.010	0.007	0.034	0.036	0.004	0.055	0.068	-0.008	-0.012	-0.018	0.021
B3_CL_SG1	0.360	0.452	0.473	1.398	1.899	1.959	2.366	3.692	3.686	0.414	0.599	0.726	1.261
B4_CL_SG1	0.363	0.411	0.406	1.532	1.725	1.671	3.317	3.482	3.394	0.645	0.940	1.235	1.154
B4_CL_SG2	0.005	0.007	0.006	0.019	0.025	0.023	0.041	0.049	0.043	-0.005	-0.008	-0.017	0.017
B4_CL_SG3	0.014	0.036	0.035	0.104	0.165	0.163	-0.093	-0.049	-0.022	-0.018	-0.032	-0.077	0.099
B5_QRT_SG1	0.894	0.678	0.639	1.190	1.056	1.030	1.616	1.382	1.345	0.725	1.376	1.177	0.978
B5_W_SG1	0.227	0.180	0.182	0.071	0.095	0.135	-0.162	0.014	0.064	0.174	0.310	0.130	0.169
B5_W_SG2	-0.023	-0.020	-0.016	-0.021	-0.021	-0.019	-0.017	-0.014	-0.013	-0.008	-0.015	-0.011	-0.026
B5_W_SG3	0.169	0.125	0.103	0.176	0.175	0.151	0.146	0.145	0.139	0.095	0.152	0.125	0.168
DK_4_5_SG2	0.006	0.005	0.004	0.023	0.019	0.016	0.036	0.028	0.028	-0.001	-0.003	-0.009	0.014
DK_4_5_SG5	0.041	0.027	0.021	0.140	0.096	0.079	0.291	0.222	0.186	0.003	0.002	-0.029	0.082
B5_CL_SG1	0.396	0.371	0.367	1.737	1.474	1.429	3.652	2.904	2.659	0.857	1.270	1.977	1.010
B5_CL_SG3	0.021	0.018	0.020	0.124	0.091	0.081	0.080	-0.087	-0.086	0.015	0.016	-0.087	0.076
B5_CL_SG4	0.196	0.180	0.181	0.871	0.729	0.702	1.572	1.263	1.162	0.402	0.590	0.850	0.511
B6_W_SG1	0.227	0.161	0.148	0.079	0.164	0.176	-0.136	0.129	0.164	0.176	0.208	0.015	0.176
DK_5_6_SG2	0.006	0.002	0.002	0.026	0.008	0.005	0.056	0.019	0.009	0.005	0.008	0.019	0.008
B5_E_SG1	-0.038	-0.004	0.005	0.238	0.240	0.284	-0.135	0.028	0.075	0.103	0.170	0.136	-0.009
B5_E_SG2	-0.002	-0.002	-0.002	-0.043	-0.035	-0.030	-0.018	-0.015	-0.014	-0.008	-0.011	-0.011	-0.013
B5_E_SG3	0.014	0.016	0.016	0.305	0.230	0.196	0.140	0.130	0.125	0.072	0.093	0.111	0.097
B6_CL_SG1	0.403	0.341	0.324	1.740	1.259	1.174	3.527	1.977	1.745	0.981	1.489	2.905	0.925
B8_CL_SG1	0.348	0.179	0.154	1.316	0.595	0.511	2.151	0.726	0.617	1.274	1.919	3.693	0.472
B9_CL_SG1	0.293	0.098	0.078	1.027	0.331	0.272	1.380	0.394	0.323	1.288	1.939	3.644	0.268
B2_W_DISP	0.022	0.151	0.153	0.046	0.176	0.170	0.060	0.132	0.141	0.004	-0.005	-0.007	-0.153
B2_QRT_DISP	0.009	-0.068	-0.065	0.061	0.046	0.064	0.095	0.270	0.287	0.009	-0.010	-0.012	-0.001
B5_W_DISP	0.147	0.115	0.093	0.138	0.140	0.120	0.131	0.101	0.094	0.060	-0.099	-0.077	-0.152
B5_QRT_DISP	-0.070	-0.050	-0.035	0.057	0.027	0.036	0.296	0.220	0.199	0.031	-0.060	-0.142	0.020
B5_CL_DISP	-0.097	-0.066	-0.062	0.245	0.167	0.147	0.015	0.009	0.008	0.025	0.095	-0.001	-0.075
B5_E_DISP	-0.014	-0.013	-0.013	-0.302	-0.230	-0.192	-0.143	-0.111	-0.103	-0.057	0.076	0.084	0.092

ii. Model 5 Results

Table 20. FEA results for stresses (ksi) and displacements (in.) for Model 5.

Channel Name	Test 13	Test 14	Test 15	Test 16	Test 17	Test 18	Test 19	Test 20	Test 21	Test 26	Test 27	Test 28	Test 29
B2_W_SG1	0.075	0.106	0.113	0.011	-0.207	-0.199	-0.01	-0.349	-0.369	0.043	0.082	0.088	0.002
B2_QRT_SG1	0.290	0.673	0.720	0.546	0.977	1.036	0.76	1.319	1.416	0.108	0.167	0.204	0.848
B1_CL_SG1	0.183	0.437	0.465	0.593	1.655	1.800	0.73	2.671	3.054	0.048	0.075	0.090	1.045
B2_CL_SG1	0.240	0.363	0.390	0.861	1.502	1.620	1.22	3.152	3.312	0.151	0.217	0.256	0.975
B2_CL_SG2	0.000	0.006	0.059	-0.005	0.020	0.021	-0.01	0.041	0.045	-0.009	-0.013	-0.017	0.011
B2_CL_SG3	0.002	0.025	0.029	-0.022	0.132	0.149	-0.08	0.022	0.046	-0.032	-0.049	-0.063	0.077
B2_CL_SG4	0.112	0.181	0.197	0.387	0.768	0.832	0.52	1.433	1.523	0.052	0.074	0.085	0.497
DK_2_3_SG2	0.001	0.005	0.005	-0.001	0.019	0.020	-0.01	0.038	0.049	-0.009	-0.014	-0.020	0.011
B3_CL_SG1	0.277	0.342	0.360	1.106	1.513	1.565	2.02	3.239	3.222	0.309	0.442	0.542	1.013
B4_CL_SG1	0.275	0.311	0.306	1.219	1.375	1.321	2.95	3.071	2.980	0.508	0.733	0.993	0.925
B4_CL_SG2	0.003	0.004	0.003	0.010	0.014	0.011	0.03	0.033	0.029	-0.008	-0.012	-0.022	0.010
B4_CL_SG3	0.012	0.006	0.005	0.018	0.558	0.053	-0.21	-0.194	-0.167	-0.049	-0.077	-0.131	0.096
B5_QRT_SG1	0.789	0.580	0.542	0.860	0.748	0.729	1.21	1.005	0.977	0.551	1.100	0.866	0.764
B5_W_SG1	0.107	0.073	0.080	-0.269	-0.210	-0.160	-0.60	-0.372	-0.306	0.003	0.033	-0.175	0.069
B5_W_SG2	-0.025	-0.022	-0.018	-0.031	-0.030	-0.028	-0.03	-0.025	-0.023	-0.014	-0.021	-0.018	-0.031
B5_W_SG3	0.148	0.104	0.082	0.090	0.100	0.078	0.08	0.056	0.054	0.055	0.034	0.059	0.050
DK_4_5_SG2	0.003	0.002	0.001	0.014	0.009	0.006	0.02	0.015	0.016	-0.005	-0.008	-0.016	0.007
DK_4_5_SG5	0.038	0.025	0.019	0.130	0.088	0.071	0.28	0.212	0.177	0.000	-0.002	-0.034	0.076
B5_CL_SG1	0.304	0.283	0.280	1.412	1.168	1.128	3.27	2.543	2.305	0.687	1.011	1.674	0.804
B5_CL_SG3	-0.004	0.048	-0.003	0.033	0.003	-0.004	-0.27	-0.196	-0.195	-0.028	-0.048	-0.176	0.019
B5_CL_SG4	0.141	0.129	0.129	0.681	0.548	0.525	1.35	1.037	0.946	0.305	0.448	0.677	0.389
B6_W_SG1	0.108	0.075	0.067	-0.256	-0.079	-0.048	-0.51	-0.176	-0.120	0.008	0.023	-0.372	0.048
DK_5_6_SG2	0.004	0.000	-0.001	0.017	0.000	-0.003	0.04	0.009	0.000	0.000	0.000	-0.011	0.003
B5_E_SG1	-0.132	-0.088	-0.075	-0.186	-0.120	-0.059	-0.58	-0.365	-0.301	-0.073	-0.078	-0.173	-0.243
B5_E_SG2	-0.005	-0.004	-0.004	-0.055	-0.044	-0.039	-0.03	-0.026	-0.025	-0.012	-0.017	-0.019	-0.020
B5_E_SG3	-0.012	-0.006	-0.006	0.227	0.152	0.114	0.06	0.047	0.046	0.035	0.094	0.046	0.118
B6_CL_SG1	0.312	0.266	0.252	1.418	1.002	0.928	3.15	1.674	1.454	0.779	1.181	2.544	0.748
B8_CL_SG1	0.268	0.133	0.112	1.038	0.439	0.369	1.83	0.542	0.449	1.021	1.531	3.239	0.358
B9_CL_SG1	0.220	0.064	0.049	0.775	0.215	0.170	1.08	0.256	0.202	1.012	1.517	3.152	0.181
B2_W_DISP	0.023	0.154	0.156	0.048	0.183	0.177	0.06	0.141	0.151	0.004	0.004	0.007	0.158
B2_QRT_DISP	0.009	-0.066	-0.064	0.058	0.046	0.064	0.09	0.272	0.290	0.007	0.009	0.010	0.001
B5_W_DISP	0.150	0.118	0.095	0.144	0.144	0.124	0.14	0.107	0.099	0.063	0.102	0.080	0.156
B5_QRT_DISP	-0.067	-0.048	-0.033	0.060	0.029	0.037	0.30	0.223	0.202	0.032	0.062	0.144	-0.018
B5_CL_DISP	-0.096	-0.065	-0.061	0.239	0.163	0.144	0.01	0.009	0.008	0.025	-0.093	0.001	0.074
B5_E_DISP	-0.016	-0.014	-0.014	-0.313	-0.237	-0.198	-0.15	-0.117	-0.109	-0.060	-0.078	-0.088	-0.096